The Physical Nature of Weak Shock Reflection

Jason Trevor Ashworth

A dissertation submitted to the Faculty of Engineering and the Built Environment, University of the Witwatersrand, in fulfillment of the requirements for the degree of Master of Science in Engineering.

Johannesburg, 2005

Declaration

I declare that this dissertation is my own, unaided work, except where otherwise acknowledged. It is being submitted for the degree of Masters of Science in Engineering at the University of the Witwatersrand, Johannesburg. It has not been submitted for any degree or examination at any other University.

Signed on ______________________

____

Jason T. Ashworth

To my family and friends, who have always supported me in everything I do.

“One day I am going to grow wings, a chemical reaction” – Thom. E. Yorke

Acknowledgements

I would like express my appreciation to Professor B. Skews, who saw the need for this project to be undertaken, for his advice and guidance during my research, and for the opportunity to co-author a journal paper.

Thanks to Mr. A. Andreis, J. Mohan and J. Goulding for their assistance with the instrumentation and optical equipment in the laboratory.

I would like to thank Dr. C. Law and Mr. N. Menon for their help with the Computational Fluid Dynamics (CFD) component of this research.

Thank you to Mr. J. Cooper and the Laboratory staff for their advice and assistance during the construction of the rig.

Abstract

Recent high-resolution numerical studies of weak shock reflections have shown that a complex flow structure exists behind the triple point which consists of multiple shocks, expansion fans and triple points. This region had not been detected earlier in experimental observations or numerical studies of weak shock reflections due to the small size of this region. New components were designed and built to modify an existing large-scale shock tube in order to obtain experimental observations to validate the numerical results. The shock tube produced a large, expanding cylindrical incident wave which was reflected off a 15° corner on the roof of the section to produce a weak shock Mach reflection with a large Mach stem in the test section. The shock tube was equipped with PCB high-speed pressure transducers and digital scope for data acquisition, and a schlieren optical system to visualise the region behind the triple point. The tests were conducted over a range of incident wave Mach numbers (M_{12} = 1.060-1.094) and produced Mach stems of between 694 mm and 850 mm in length. The schlieren photographs clearly show an expansion fan centered on the triple point in all the successful tests conducted. In some of the more resolved images, a shocklet can be seen terminating the expansion fan, and in others a second expansion fan and/or shocklet can be seen. A 'von Neumann reflection' was not visualised experimentally, and hence it has been proposed that the four-wave reflection found in these tests be named a 'Guderley reflection'. The experimental validation of Hunter & Tesdall's (2002) work resolves the 'von Neumann Paradox'.

Contents

List of Figures

List of Tables

1. Objectives

1. Determine whether Hunter & Tesdall's (2002) theoretical results can be proved experimentally by observing a second or subsequent shock or expansion region behind the triple point. This would require the following to be undertaken:

    a. Design and build or modify a large-scale shock tube using the existing large shock tube available at the Mechanical Engineering Laboratory.

    b. Test the new shock tube and determine the characteristics of the tube.

    c. Obtain photographs of the triple point region of a large-scale von Neumann Reflection.

2. Introduction

2.1. Background Theory

The following section gives a brief outline of the theory used throughout the analysis of the physical processes.

Mach number is a measure of the speed of a shock wave or gas relative to the speed of sound in ambient conditions. It is a dimensionless parameter and is defined as:

$$M = \frac{v}{a_s}$$

where: v is the velocity of the shock wave or gas [m/s]

a_s is the ambient speed of sound [m/s]

The speed of sound in a compressible gas is defined as:

$$a_s = \sqrt{\gamma R T_1}$$

where: γ is the ratio of specific heats of the gas

R is the gas constant

T_1 is the ambient temperature of the gas [K]

For the subsonic case, where $M < 1$, the particles of gas flow smoothly around any disturbances and anticipate changes in flow. For the supersonic case, where $M > 1$, the particles undergo almost discontinuous adjustments of fluid properties (pressure, temperature and density). These discontinuities are shock waves and adjust the fluid properties instantaneously.

The inverse Mach slope (*a*) is given by the following equation for uniform, plane incident waves off a reflecting surface:

$$a = \frac{\theta_w}{2\sqrt{M-1}}$$

where: θ_w is the reflection wedge angle in radians

M is the Mach number of the incident wave

2.2. Shock Wave Reflections

The first scientist to discover the phenomenon of shock wave reflections was Ernst Mach, as far back as 1878 (Ben-Dor 1992). He identified two types of reflection, namely a two-shock reflection and a three-shock reflection. These have since become known as a regular reflection and a Mach reflection respectively. Research into shock reflection was re-initiated in the 1940's by von Neumann, and since then the basic wave configurations have been divided into more specific structures.

The reflection of shock waves is generally divided into two categories: regular reflection and irregular reflections. The type of reflection depends on (M_S, γ, θ_w) parameter space, where M_S, γ and θ_w are the incident shock wave Mach number, the gas specific heat ratio and wedge angle respectively. For shallower wedge angles, and moderate Mach numbers, the reflection point detaches from the reflecting surface and forms a three-shock configuration, or irregular reflection.

A regular reflection consists of two shocks, an incident wave, and a reflected wave; which intersect on the reflecting surface at a reflection point and is generally observed for large wedge angles.

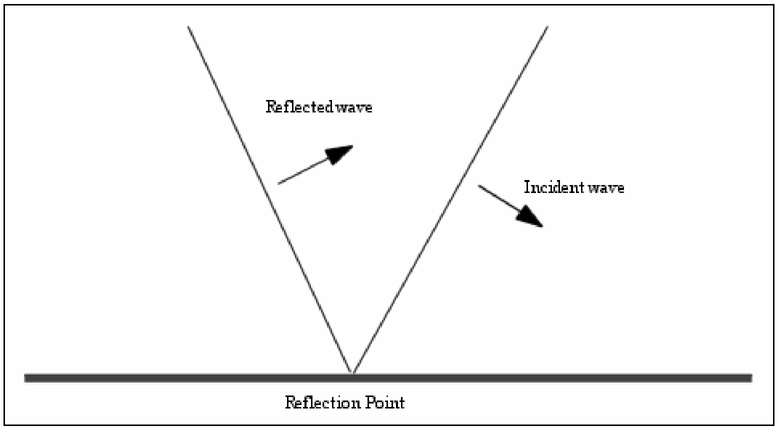

Figure 2.1 – Schematic diagram of a regular reflection

All other reflections which occur when an incident wave reflects off a surface are termed irregular reflections and are divided into two categories: Mach reflection and von Neumann reflection. A Mach reflection consists of three shocks which intersect at a single discontinuity called the triple point which follows a trajectory along the angle χ from the leading edge of the wedge. The structure is made up of an incident wave, a reflected wave, a Mach stem, and a slipstream. The reflecting point is now at the point where the Mach stem contacts the reflecting surface.

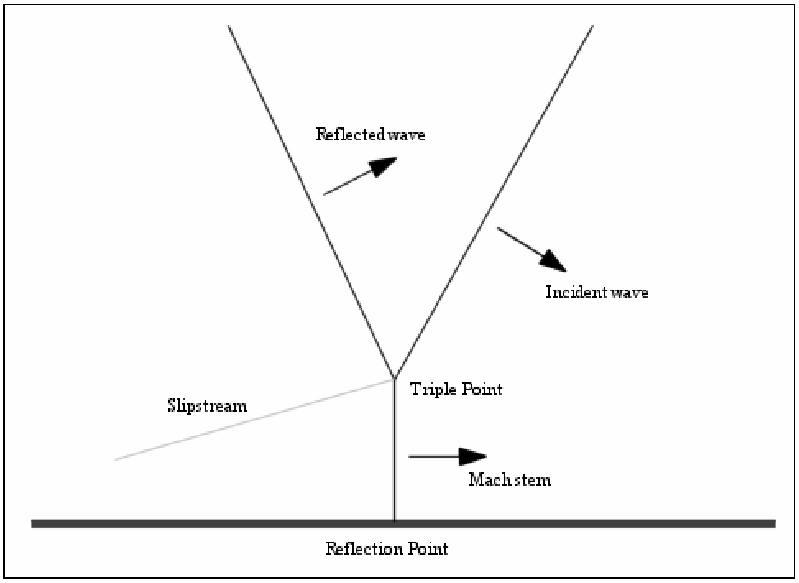

Figure 2.2 – Schematic diagram of a Mach reflection

Shock waves that are moving at a constant velocity can be analyzed by attaching a frame of reference to the shock wave. In this frame of reference, the shock wave is stationary, while the flow field is moving, and is known as pseudo-steady flow. The transformation from an inertial to a moving frame of reference is known as Galilean transformation.

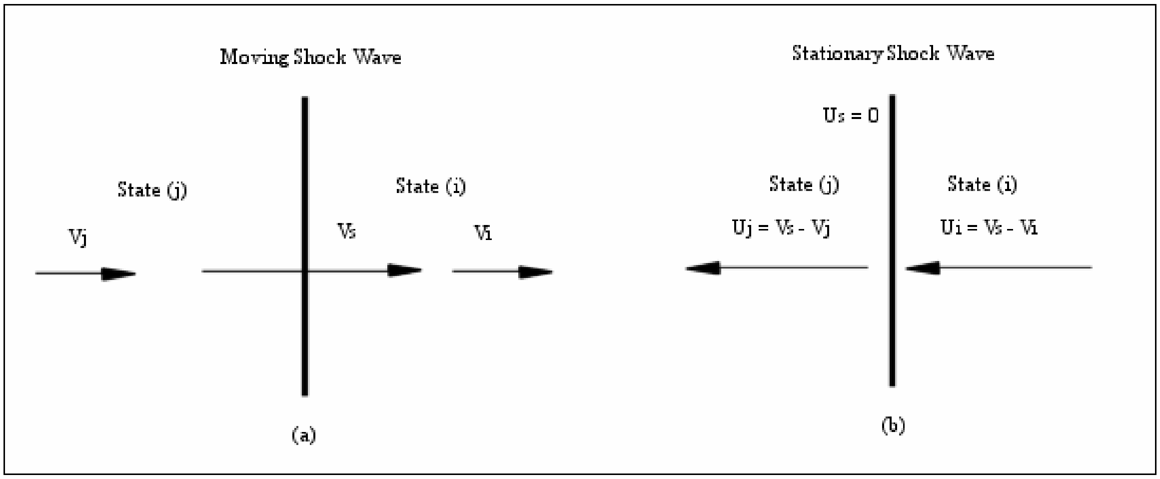

Figure 2.3 – Schematic diagram of Galilean Transformation

In Figure 2.3(a), the constant velocity shock wave is transformed into a stationary shock wave in Figure 2.3(b). In Figure 2.3(a) the moving shock wave has a constant velocity V_s, which is moving into a flow field with velocity V_i, and inducing a flow field of velocity V_j behind the wave. In Figure 2.3(b) the flow moves towards the stationary shock wave with a velocity $U_i = V_s - V_i$, and is reduced to $U_j = V_s - V_j$ after leaving the shock wave.

In pseudo-steady shock reflection, a single Mach reflection from a wedge would have the following configuration:

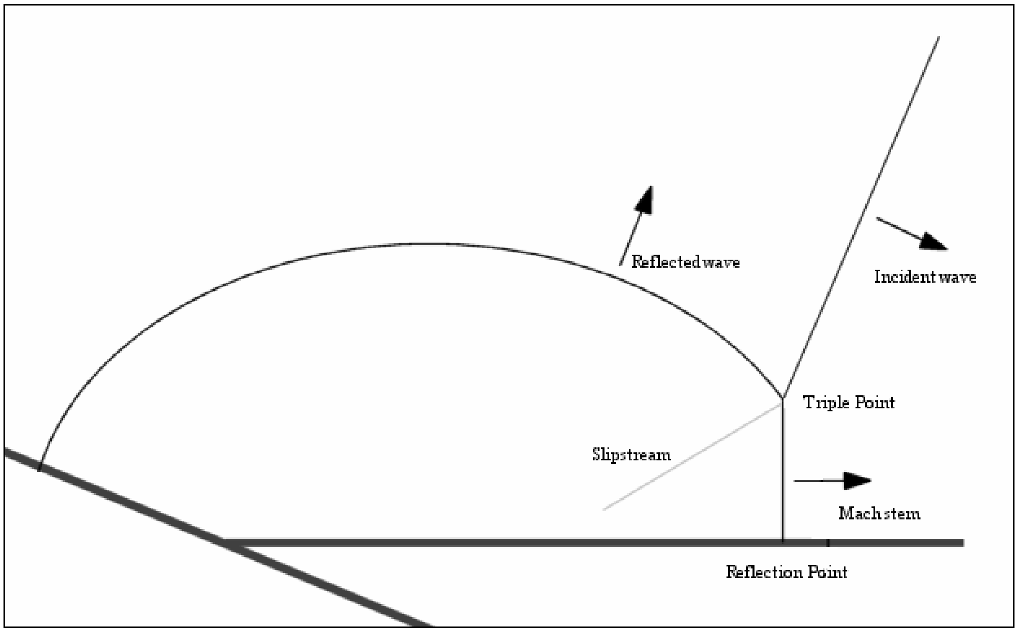

Figure 2.4 – Single Mach Reflection from a wedge

As the incident wave moves towards the wedge, a Mach stem develops and increases in length as it propagates up the wedge surface, causing the triple point to follow a straight line trajectory from the leading edge of the wedge angle, at angle χ to the wedge surface. The reflected wave expands in all directions.

A von Neumann reflection is a weak incident shock Mach reflection over a small wedge angle, where the reflected wave degenerates into a band of compression waves in the region behind the triple point, as defined by Colella & Henderson (1990) in Figure 2.5.

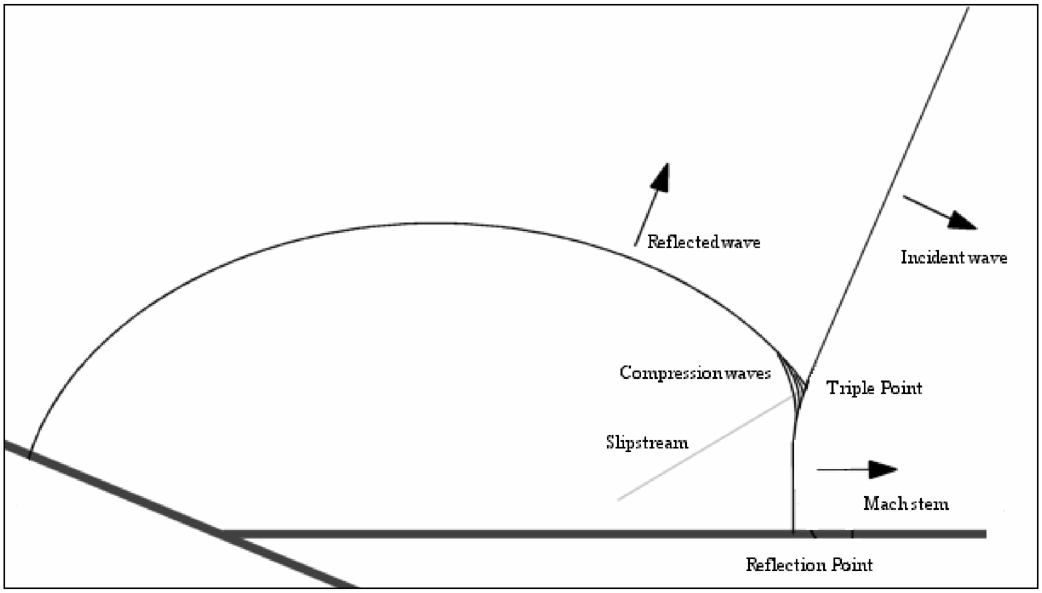

Figure 2.5 – von Neumann Reflection from a wedge

Comparing schlieren photographs of a single Mach reflection with a von Neumann reflection, it can be seen that the slope of the incident waves and Mach stem are discontinuous for a Mach reflection, whilst the slopes are almost continuous for a von Neumann reflection. The slipstream is also very distinct in a single Mach reflection, but appears as a distributed shear layer in von Neumann reflections. The triple point is also not a defined single point in a von Neumann reflection.

The equations which describe the regular and Mach reflections are known as two and three-shock theory respectively, and were formulated by von Neumann (1943). The analysis applies the oblique shock wave equations for the regions near the reflection or triple point, along with geometrical and boundary conditions. Basic assumptions are that the fluid is inviscid, that all waves are infinitely thin and plane, and that the regions between waves are uniform.

The theory produces results which are agreeable with experimental observations for regular and Mach reflection, except for the fact that regular reflection persists slightly beyond what theory suggests as its limit. This has since been attributed to thermal and viscous boundary layers on the wedge surface. The three-shock theory breaks down for weak shock reflections (von Neumann reflection).

2.3. Importance of the study

Experimental observations of an irregular reflection of a weak shock from a wedge have shown a three-shock reflection which meet at a triple point (Bleakney & Taub 1949). This type of reflection closely resembles a single Mach reflection, even though it has been shown that a standard triple point reflection for sufficiently weak shocks is theoretically impossible (Bleakney & Taub 1949; von Neumann 1963; Henderson 1987). This conflict between theoretical and experimental results for weak shock reflections has been in dispute for more than fifty years, and is referred to as the “von Neumann Paradox” (Birkhoff 1950).

Guderley (1947) proposed that a supersonic region behind the triple point existed, and hence an expansion fan is generated behind the triple point. Initial experimental observations did not show any evidence of such a supersonic region or expansion fan, nor did any numerical results show such evidence. This work had not been followed for almost half a century, the main reason why no real progress had been made can be attributed to the very small region under study, which was generally beyond the resolution of numerical studies until higher performance computers became available. Any experimental study would not have been able to resolve such a small region optically, due to the small scale of the supersonic patch in conventional shock tubes.

Various approaches have been made in studying the von Neumann paradox, some of which concentrated on the reflected wave angle and the triple point trajectory angle, but did not examine the flow field near the triple point.

Colella & Henderson (1990) used a numerical code to resolve detailed structures of the discontinuities in the vicinity of the triple point. Their solutions indicated that the reflected shock wave behind the triple point was not a single shock wave, but a smoothly distributed self-similar band of compression waves of finite thickness, which was too small to have been detected experimentally. Colella & Henderson termed this type of reflection a von Neumann reflection.

They concluded that the transition from simple Mach reflection to von Neumann Reflection occurred when the angle between the reflected wave and slipstream (β) reached $\pi/2$, as this was where the experimental and theoretical results diverged.

Olim & Dewey (1992) tried to obtain better agreement between the theory and experiment by relaxing the conditions that the flow either side of the triple point should not be parallel, and that the pressures could be different. They achieved better results, although evidence to support their assumptions is quite suspect.

Sandeman (1997) used the extensive experiments undertaken by Olim & Dewey (1992) as well as those by Sasoh *et al.* (1992), which together with his own predictions (Sandeman 2000), calculated wave angles at the triple point using three and four-shock geometry. He concluded that neither model was suitable but suggested that this could be attributed to a lack of sufficient resolution.

In 1992 Brio & Hunter began examining Mach reflection by using the Burgers equation. Čanić & Keyfitz (1995) revealed the existence of a complex square-root singularity at the wave confluence, by using a new theoretical approach. Their solution implied the existence of a complex flow structure near the triple point.

Vasil'ev & Kraiko (1999) were the first to show, from their high-resolution numerical studies using the Euler equations that a four-wave configuration, as suggested by Guderley, does exist. They show that for a wedge angle of 12.5° and a Mach number of 1.47 the angle between the slipstream and the reflected shock exceeds $\pi/2$ and a fan of rarefaction waves is centered on the triple point. The flow immediately behind the reflected wave is subsonic and convergent, and passes through sonic velocity, forming a small supersonic patch as proposed by Guderley (1947).

The supersonic patch is outlined by the dotted sonic line in Figure 2.6, where evidence of an expansion fan can also be seen emanating from the triple point.

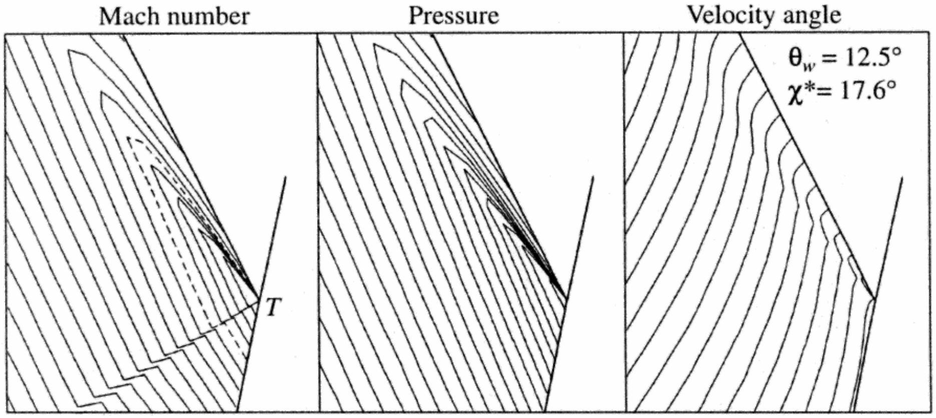

Figure 2.6 – from Vasil'ev & Kraiko (1999) an expansion fan can be seen centered on the triple point, as well as a supersonic patch outlined by the dotted sonic line.

When the wedge angle was increased to 20°, the supersonic patch shrunk to such a degree that it could no longer be detected even with additional grid refinement. For this case, the angle between the slipstream and the reflected wave again exceeded *π/2*. In another example they demonstrated that the size of the region consisting of the fourth wave is several thousandths of the dimension of the perturbed flow, supporting the reason why Guderley's work had not received due recognition was simply because of insufficient resolution being achievable.

Vasil'ev & Kraiko's (1999) work also implies that a number of distinctions of flow types exist within the domain of the von Neumann Paradox (where $\beta > \pi/2$), and finds no evidence of the structure described by Colella & Henderson (1990).

Hunter & Brio (2000) obtained a numerical solution for the unsteady transonic small-disturbance equations, which gives an asymptotic description of weak shock reflection, clearly showed a supersonic region behind the triple point of a weak shock reflection. They estimated this region to be 0.05 to 1% of the height of the Mach stem. This result has confirmed that Guderley's structure was in fact correct, as can be seen from Figure 2.7.

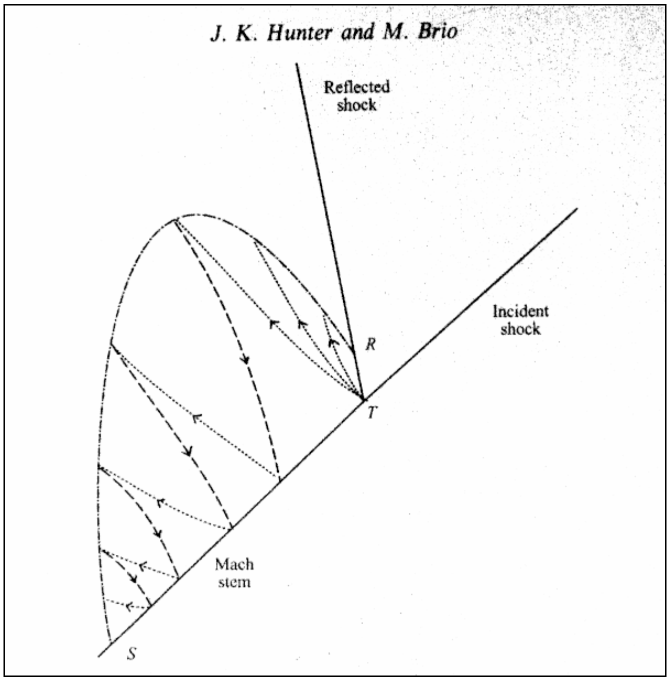

Figure 2.7 – The Guderley (1947) structure confirmed by Hunter & Brio (2000)

The authors speculated that, analogous to the supersonic region on a transonic airfoil being terminated by a shock, a small shock may exist behind this supersonic patch, and there may be series of such patches.

Zakharian *et al.*(2000) then went on to show the supersonic region existed for the full Euler equations, and supported the existence of an expansion fan at the triple point. By choosing a similar parameter space as used in Hunter & Brio (2000), they were able to validate the results previously obtained with the transonic small-disturbance equations. It was also argued that the supersonic patch was too small to be resolved in previous numerical solutions, such as those obtained by Colella & Henderson (1990).

For an incident shock Mach number of 1.04, and a wedge angle of 11.46°, Zakharian *et al.* (2000) estimated the size of the patch to be 0.5 % the height of the Mach stem. The reflected shock would also be much weaker than the incident wave, with a Mach number of only 1.003 at the triple point. In their conclusion, it was stated that boundary conditions should not affect the size of the supersonic region, the main effect viscosity would have is the thickness of the shocks. It was shown that for the parameter space described, that a Mach stem height of 1 m would produce a supersonic patch an order of magnitude larger than the reflected shock thickness.

Both of these numerical results were not, however, resolved enough to determine the detailed structure of the flow behind the triple point.

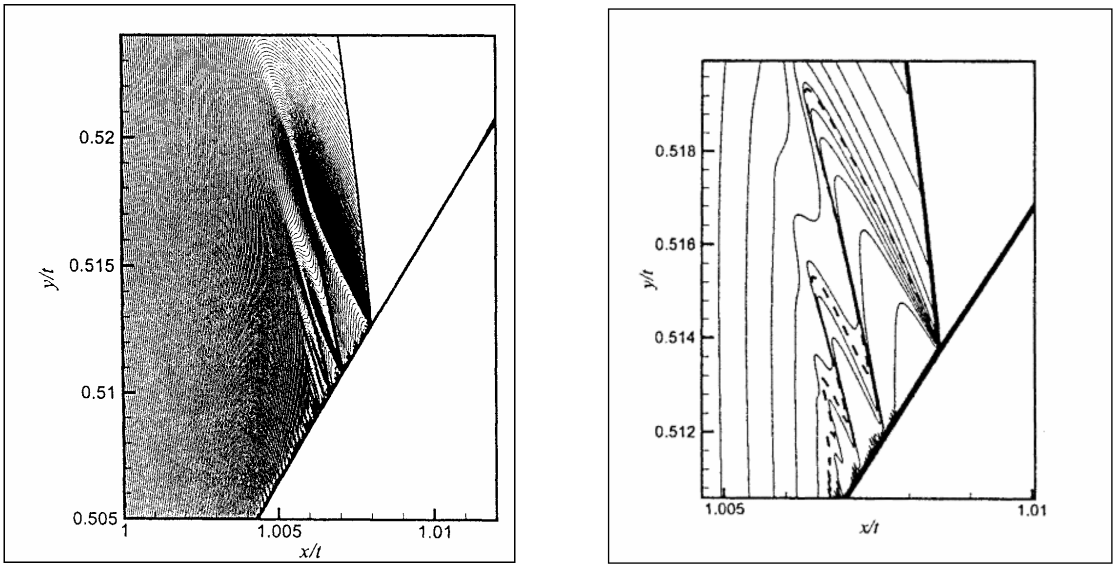

(a) (b)

Figure 2.8 – From Hunter & Tesdall (2002): (a) Plot of u near the triple point
(b) Complex flow of expansion fans,
shocks and sonic lines.

Tesdall & Hunter (2002) then went on to obtain results from a new numerical scheme for a stationary Mach reflection of weak shocks, which were similar to those obtained previously, except that the solutions were more resolved and showed a structure involving a sequence of supersonic patches formed by the reflection of shock and expansion waves between the sonic line and Mach shock. Each of the reflected shocks then intersects the Mach shock, forming a sequence of triple points behind the leading triple point. These results have supported the notion that, from theoretical considerations, an infinite number of triple points exist in an inviscid weak shock Mach reflection. The existence of an expansion fan at each triple point would resolve the "von Neumann Paradox".

Hunter & Tesdall (2002) further resolved their solutions using steady and unsteady transonic small disturbance equations. It was also shown that the size of the supersonic patch decreased rapidly with an increase in the inverse Mach slope (a), with the most refined solution being at a = 0.5.

These recent studies have been under way to increase understanding and to hopefully put to rest the paradox, especially with the use of the latest computers to obtain very high-resolution numerical solutions of the flow structure in the region behind the triple point. There, however, have been no further attempts to observe this small supersonic region experimentally, mainly due to the size of the shock tube required to observe such a small region.

Hunter & Brio (2000) estimated that, from their asymptotic equations, an incident Mach number of 1.04, a wedge angle of 11.5°, and if the shock propagated 1 m along the wedge the Mach stem would be 0.1 m high. The supersonic patch would then be 1 mm high, normal to the wedge, and 0.1 mm wide. Such lengths are not achievable in conventional shock tubes, and would generally be one-fifth the size, resulting in a Mach stem length of 20 mm and a patch roughly 0.2 x 0.02 mm in size.

This puts the University in a unique position, having a disused large section shock tube in the Laboratory. The shock tube had a test section height of 1105 mm and 100 mm wide, and was almost 4 m long. The existing shock tube could be modified to observe the supersonic region experimentally, with sizes possibly up to four times larger than that described in Hunter & Brio (2000), and hence validate the theoretical analysis and finally put the "von Neumann Paradox" to rest.

3. Design Development

3.1. Existing Shock Tube Test Section

In order to keep costs down, it was decided from the outset to utilise an existing large aspect-ratio (1:11.05) shock tube. The rig had been designed and built in the mid 1970's, and was subsequently abandoned due to the difficulty in obtaining plane waves due to the non-uniform rupture of the diaphragm inherent of a large aspect-ratio driver section. The shock tube was complete with a test section which incorporated a circular, rotating wall section with circular windows that allowed a large area of the test section height to be examined at the downstream end.

The existing driver section would have to be removed, and a new driver section designed to eliminate the diaphragm rupture problems. Since the existing shock tube had a constant cross-section area, a large wedge would have to be introduced into the test section to produce the required weak shock reflection, either from the floor or the roof of the test section.

After considering these two necessary modifications it was decided that adding a new divergent section, which would be mated at the old driver-channel interface, would produce a corner at the entrance to the test section similar to the effect of a wedge angle. The new divergent section would not be plagued by poor diaphragm rupture as the incident wave would be expanding from a low strength, small-aspect ratio, plane wave at the inlet, to a weaker, large-aspect ratio, cylindrical wave at the outlet. The incident wave for the weak shock reflection would therefore be a large-radius cylindrical wave and not a planar wave. The use of a uniform, non-planar wave was regarded as being sufficient as it is the area around the triple point that is of prime interest, and not necessarily the wave reflection pattern.

Upon exit of the divergent section, the expanding incident wave would become nearly planar at the exit of the test section as opposed to a more conventional planar wave to be reflected at a corner into a contracting section. In this latter example it would be difficult to obtain the small region we are looking for since its size is dependent on the Mach stem length, and therefore the test section height must be as large as possible. For a test section the size of that obtainable here, a conventional planar shock tube would require a section nearly 2 m high at the introduction of the wedge angle.

The new shock tube would have to be relocated to accommodate the new rig, which would be more than double its original length, and the existing rig had been placed across two rooms with no room for expansion on either side. The original rig had been designed to serve as a large-scale shock tube to produce large planar waves for testing of Mach reflections from a wedge, and was designed to withstand an overpressure up to 1 bar.

The original large aspect-ratio shock tube had the following dimensions:

Length (excluding driver):	3993 mm
Internal Width:	100 mm
Internal Height:	1105 mm
Wall Thickness:	20 mm
Roof/Floor Thickness:	5 mm
External Width (including ribs)	290 mm
External Height (including supports):	1500 mm

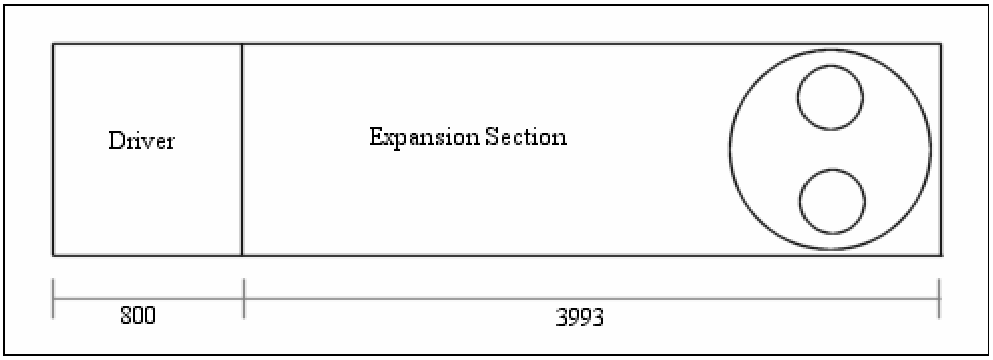

Figure 3.1 – Schematic diagram of original large-scale shock with dimensions in mm.

3.2. Identified Design Tasks

The following components would therefore have to be designed and built, in order to operate the new, large-scale shock tube:

1. A new sloping divergent section, in order to provide a corner for reflection, and to improve the diaphragm rupture characteristics of the shock tube.

2. A new driver section would have to be built for the smaller aspect-ratio inlet of the divergent section. The driver should be easily moved for re-fitting of the diaphragm.

3. A mechanism to rupture the diaphragm.

4. Various supports would have to be designed to support the large existing and new structures.

3.3. CFD Investigation

3.3.1 Importance of the CFD Investigation

Since the geometry of the problem is unknown, it was decided that an investigation into the problem using a low to mid-resolution CFD package was needed. There was no investigation into the region around the triple point using this approach, since such results would be far too low in resolution compared to the results obtained by Hunter & Tesdall (2002) and previous high-resolution studies, but rather a study on what geometries of the new divergent section would be optimal in maximising the Mach stem height for low incident Mach numbers.

Luke Feltun's C++, Euler – based 2D code was used to investigate different shock tube geometries, by altering the corner angle (the wedge angle θ_w) of the new divergent section, and the Mach number at the driver exit/divergent inlet.

3.3.2. CFD Results

A range of wedge angles were investigated, from 10° to 20°, and the entry Mach number was also varied from $M_{initial} = 1.1 - 1.5$. The resolution was determined by the *cfl* number, which is set by the user. The *cfl* is the number of initial cells per characteristic length.

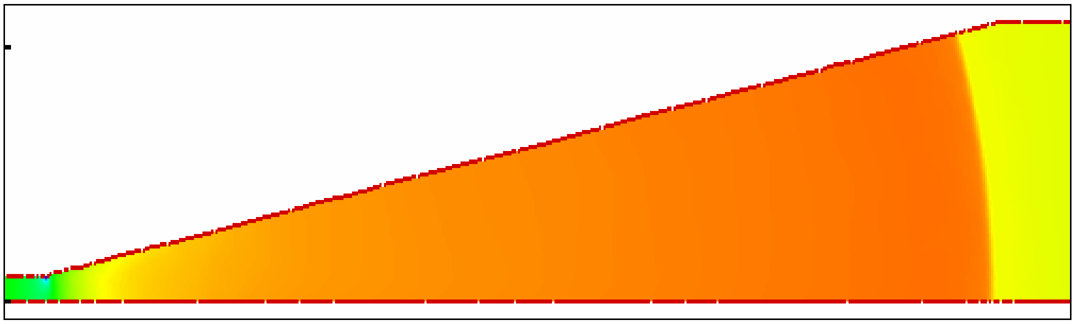

Figure 3.3.1 – CFD contour plot of ρ showing the expanding cylindrical wave

The results of these simulations were processed using Amtec Tecplot 9.0 ©, to display plots of the fluid properties at different run intervals. From these plots, the reflected wave and triple point were not clearly distinguished, and an estimate of the position of the triple point was taken for a variety of runs. The fluid properties of the flow ahead and behind the incident wave and Mach stem, were recorded in order to determine the Mach number of the incident shock wave and Mach stem.

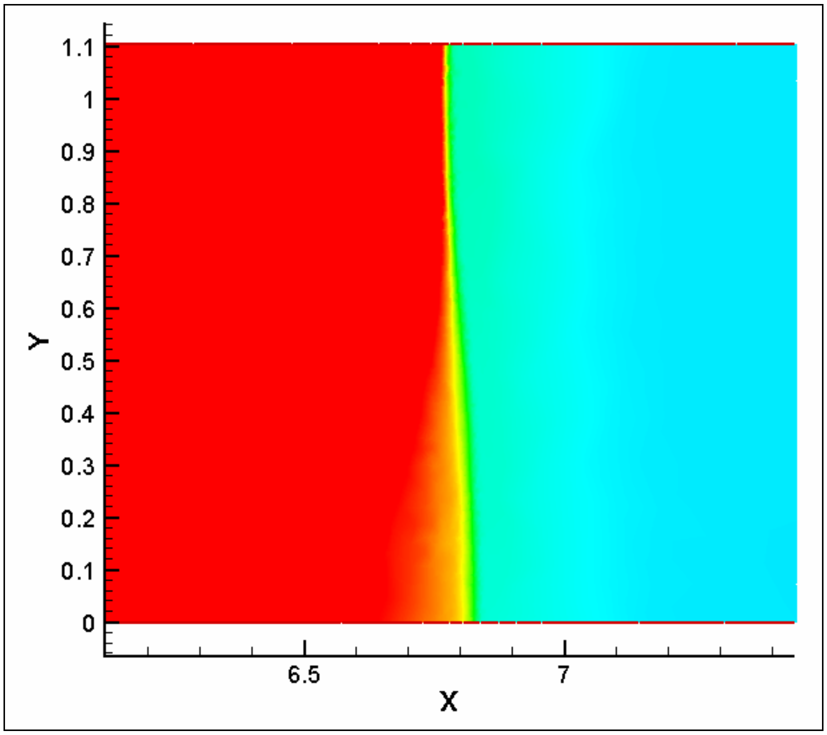

Figure 3.3.2 – CFD contour plot of ρ of the wave structure in the test section

The reflection structure and triple point is not very clear in the CFD results, but the configuration of the waves can be estimated from the geometry of the tube and of the incident wave and Mach stem geometry.

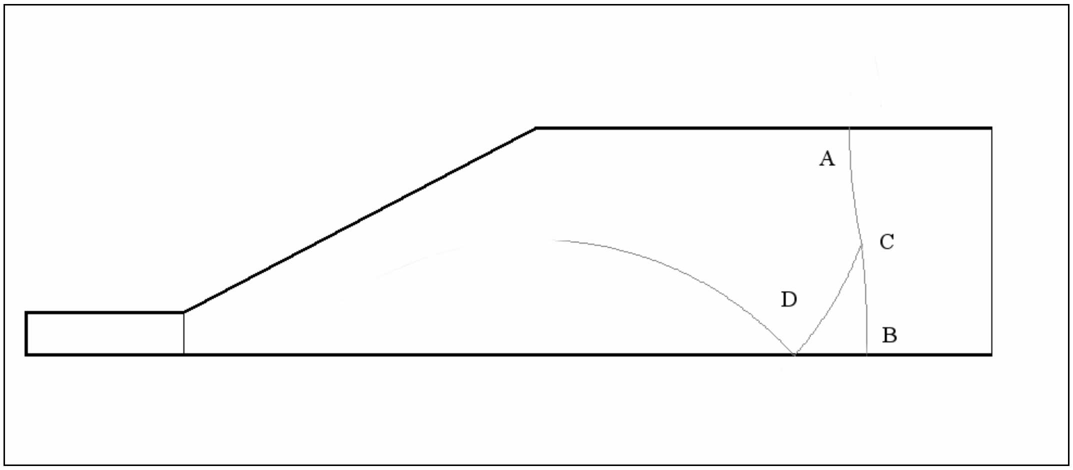

Figure 3.3.3 – Schematic representation of the reflection structure once it reaches the test section

Figure 3.3.3 shows the wave reflection configuration as it reaches the test section window, with the Mach stem (A), incident wave (B), triple point (C) and reflected wave (D). The incident wave and Mach stem at the test section have become almost planar, and the reflected wave has rebounded off the floor of the tube.

Plots of the estimated triple point trajectory, Mach number of the incident wave and Mach stem versus position were plotted for various entry Mach numbers and wedge angles. An estimate of the inverse Mach slope (*a*) was also plotted for various wedge angles and initial entry Mach numbers.

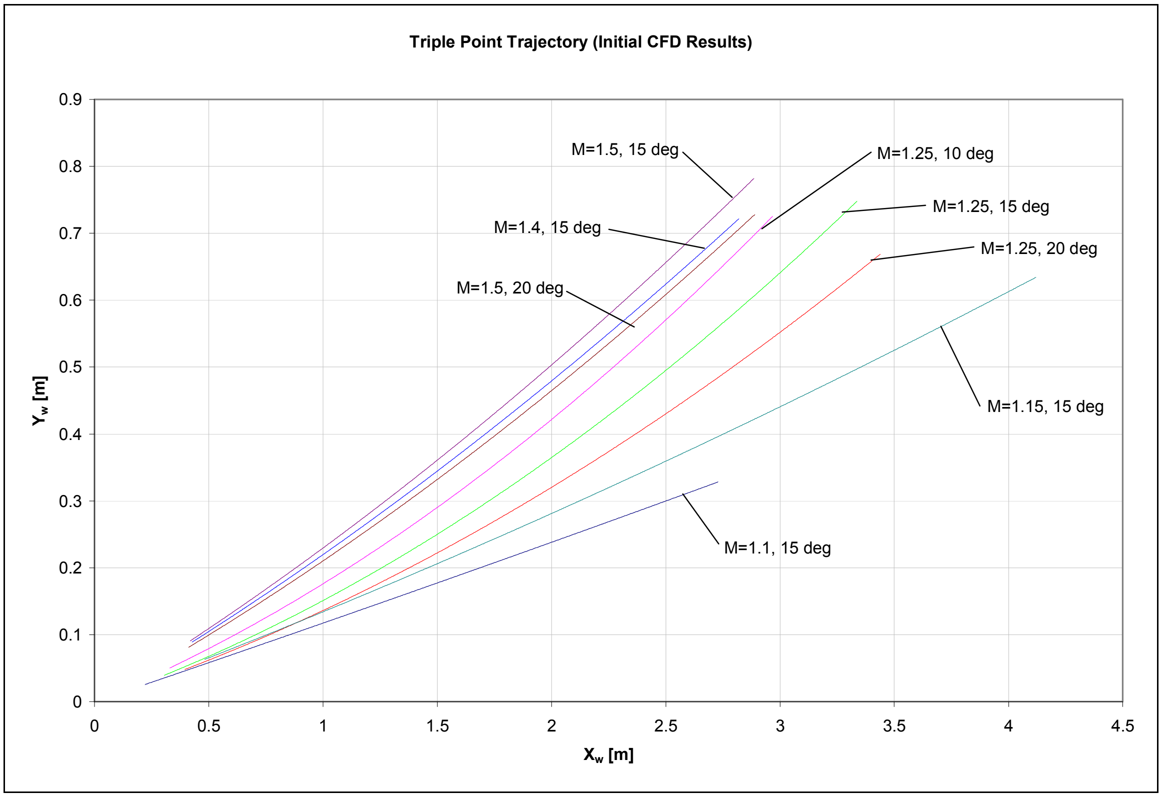

Figure 3.3.4 – Triple Point Trajectory of CFD runs with varying initial Mach number and wedge angles

As expected, the triple point trajectory follows a parabolic path shown in Figure 3.3.4, and not a linear path as for a planar incident wave. The data points (not shown) are curve-fitted with second-order polynomials, passing through the origin, for various entry Mach numbers and wedge angles. It is important to note that the origin of this figure is the reflection corner on the roof of the shock tube, hence the trajectory is inverted relative to Figure 3.3.3.

The decay of the incident wave was also plotted from the CFD results and estimated by using a $1/R^2$ relationship, since the expanding cylindrical wave can be regarded as a 2D blast wave. In the actual shock tube there would be losses due to the inefficiencies of the rupture of the diaphragm and other effects.

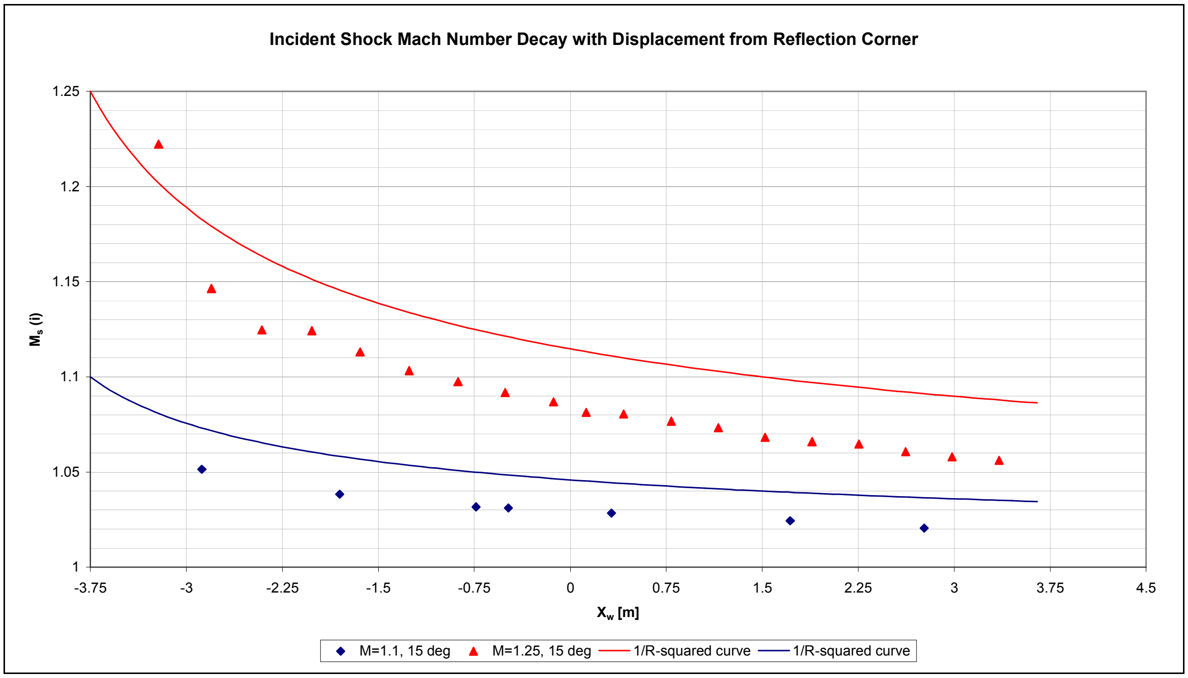

Figure 3.3.5 – Incident wave Mach number decay versus the displacement from the reflection corner

As can be seen in Figures 3.3.5 & 3.3.6, the incident wave Mach number decays rapidly from the inlet as it expands to the outlet ($X_w = 0$) of the divergent section. The expanding wave decayed roughly 7-20%, depending on the initial Mach number entering the divergent inlet to the corner of the reflection. The decay is then much less in the test section, decreasing by approximately 0.01-0.04 over the range of Mach numbers or 0.1-4% from the corner of the reflection.

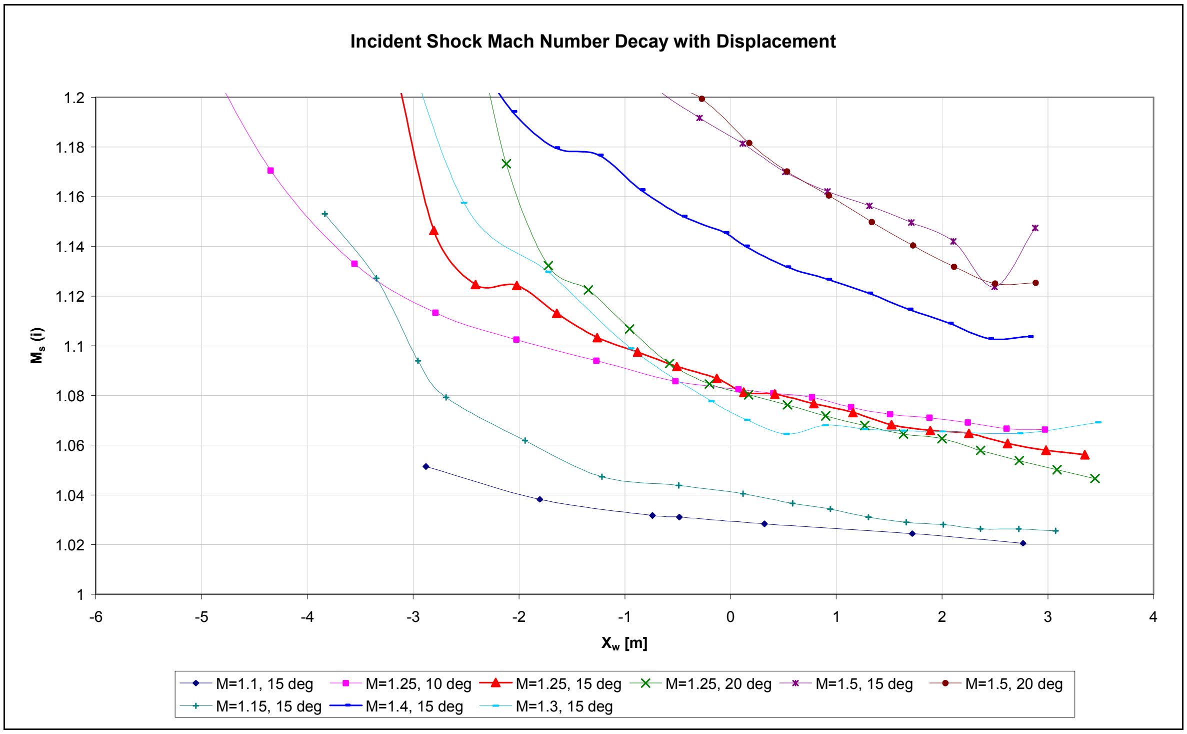

Figure 3.3.6 – Incident wave decay with displacement. The reflection corner is at $X_w = 0$.

From Hunter & Tesdall (2002), for the problems considered, the supersonic region was largest for values of $a = 0.5$ to 0.67. It is noted that the inverse Mach slope would not necessarily be the same as that achieved for a similar, planar incident wave Mach reflection, but was used in order to predict the best chance of maximising the supersonic region behind the triple point by calculating the value of a at various intervals during the reflection.

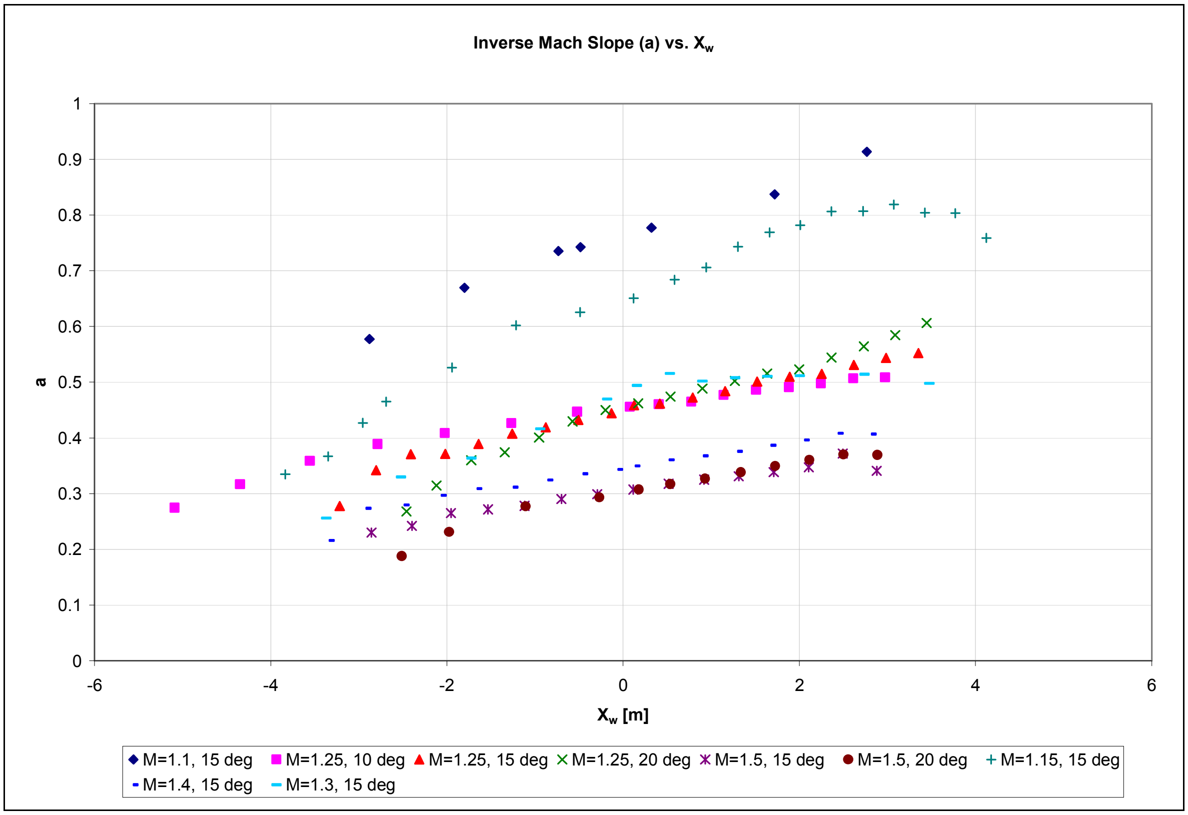

Figure 3.3.7 – Plot of the inverse Mach slope (a) with displacement from the reflection corner (X_w = 0) for various initial Mach numbers and wedge angles

From Figure 3.3.7 it can be seen that an initial Mach number of 1.25 and a wedge angle of 15° could produce promising results, similar to those achieved numerically by Hunter & Tesdall (2002).

Further CFD Simulations were performed to compare with the experimental results obtained. The new CFD simulations were setup with the final geometry of the completed shock tube, and were once again over a range of Mach numbers and resolutions. The results of these simulations were once again processed to determine the various graphs for the triple point trajectory, inverse Mach slope (a), etc. These results were used to predict the position of the triple point when taking photos, and to validate the experimental results.

It can be seen from Figure 3.3.8 that Mach stem lengths of between 500 and 800 mm could be achievable using initial driver Mach numbers of 1.1-1.5, corresponding to incident Mach numbers in the test section of around 1.02-1.15, for the final shock tube geometry. The data points are curve fitted with second order polynomials in the figure below.

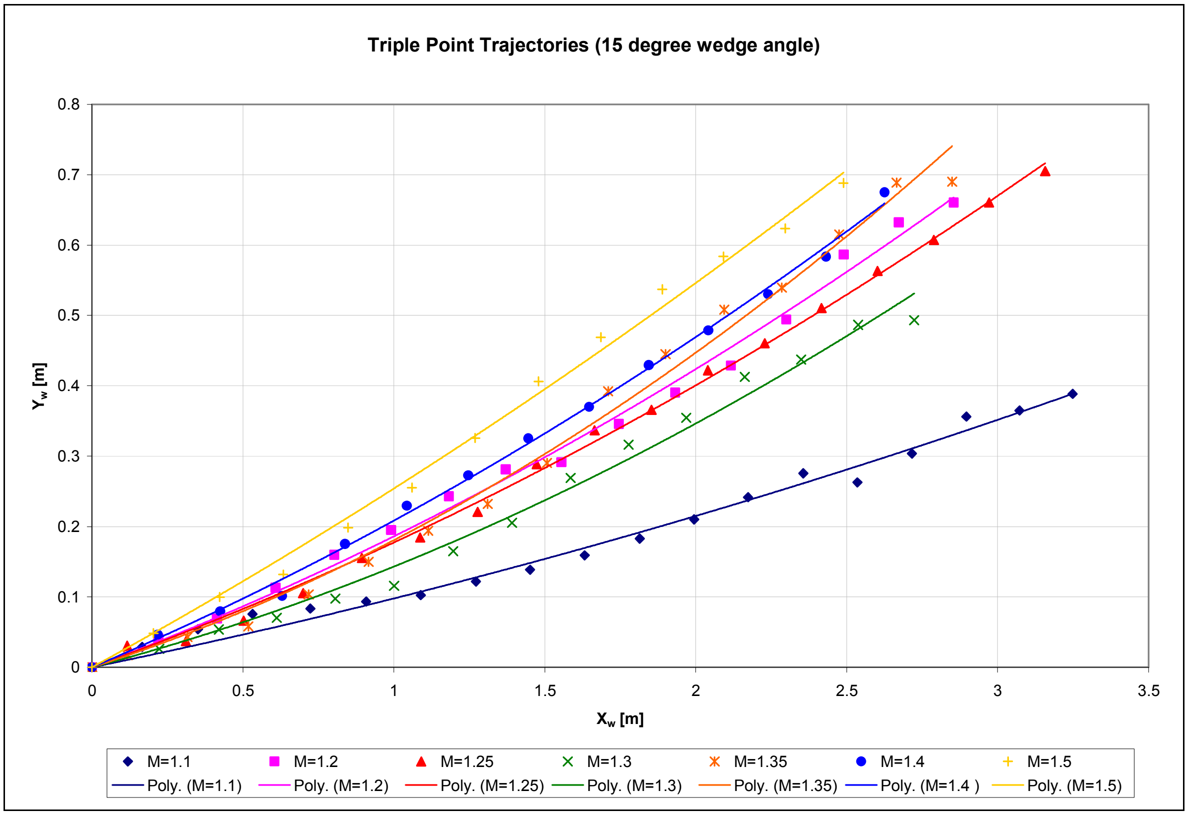

Figure 3.3.8 – Triple Point Trajectories from final CFD results for the shock tube

Further graphical results are included along with some of the readings tabulated in the CFD results section in the Appendix A – CFD Results.

3.4. New Divergent Section

As described before, a new tapering section would have to be designed and built, which would have a roughly square inlet that would expand to the test section height of the old section. The best inlet aspect ratio for efficient diaphragm rupture is 1:1, so the height of the inlet was set equal to the width of the downstream test section (100 mm).

Since the outlet height, inlet height and width were fixed, the only variable to be determined was the angle of the sloping wall (which in turn fixed the length of the section). A steep angle would cause a strong reflection, and hence the triple point (the area under investigation) would not appear in the test windows, approximately 3.6 m downstream of the reflection. A small angle would mean the Mach stem height would be low, and it has been shown that the size of the area under investigation is dependant on the height of the Mach stem. A shallow angle would also make the placement and manufacture of the section more problematic due to its length.

From the initial CFD results, it was decided that the angle of the sloping wall should be fixed to 15 degrees as this showed promising results, and the angle could be set to a smaller angle by inserting a ramp/plug if necessary.

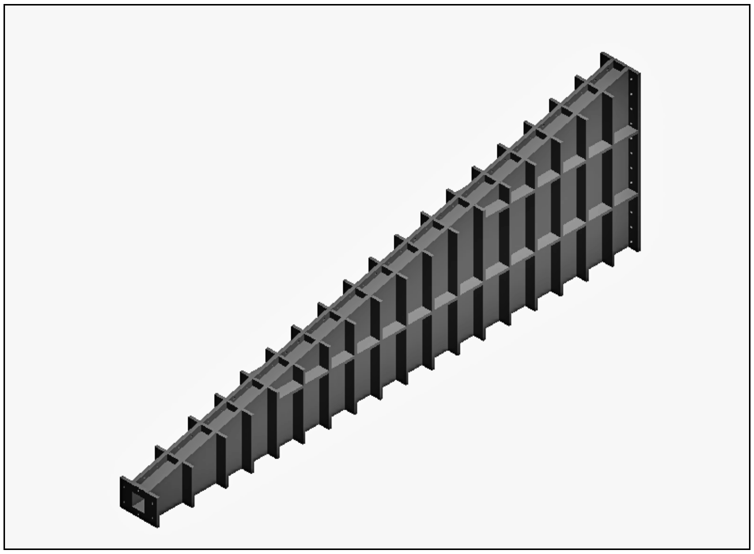

Figure 3.4.1 – Isometric View of Divergent Section

The design was based on that of the existing test section, and has similar ribs along the outside walls of the entire section, in order to increase the stiffness of the large walls. The section is therefore stronger than required, which leaves room open for other higher Mach number shock tests.

The overall dimensions of the divergent section are given in the diagram below:

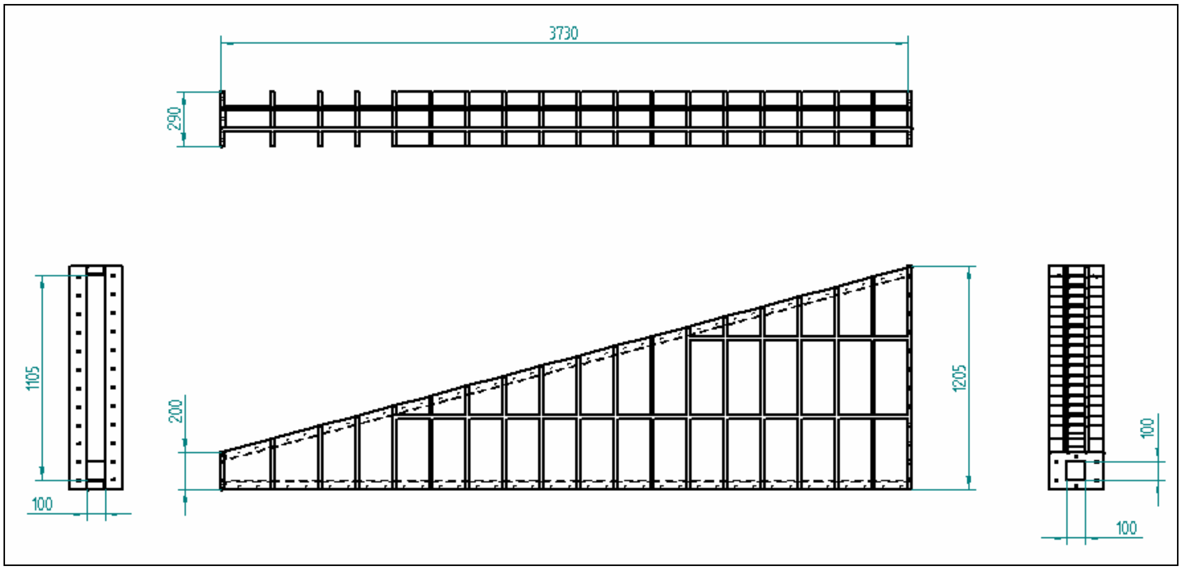

Figure 3.4.2 – Dimensions of Divergent Section (mm)

Detailed engineering drawings of the section are filed and some of these are reproduced in the Appendix B – Divergent Section Engineering Drawings.

3.5. Driver Section

The driver section was designed using standard mild steel tubing as the pressure chamber, strengthened at the ends with steel flanges. The end cover can be removed to increase the length of the driver section if required. The tube is standard Schedule 80 mild steel, round tubing with a 10.97 mm wall thickness, 1500 mm length and an external diameter of 168 mm. Two support rings were welded around the tube to mount the height-adjustable support wheels (described under Chapter 3.7 – Supports) which also function as ribs to strengthen the tube.

The driver section length was chosen after plotting the wave reflection from the diaphragm rupture, in order to delay the effect of the reflected wave on the incident wave.

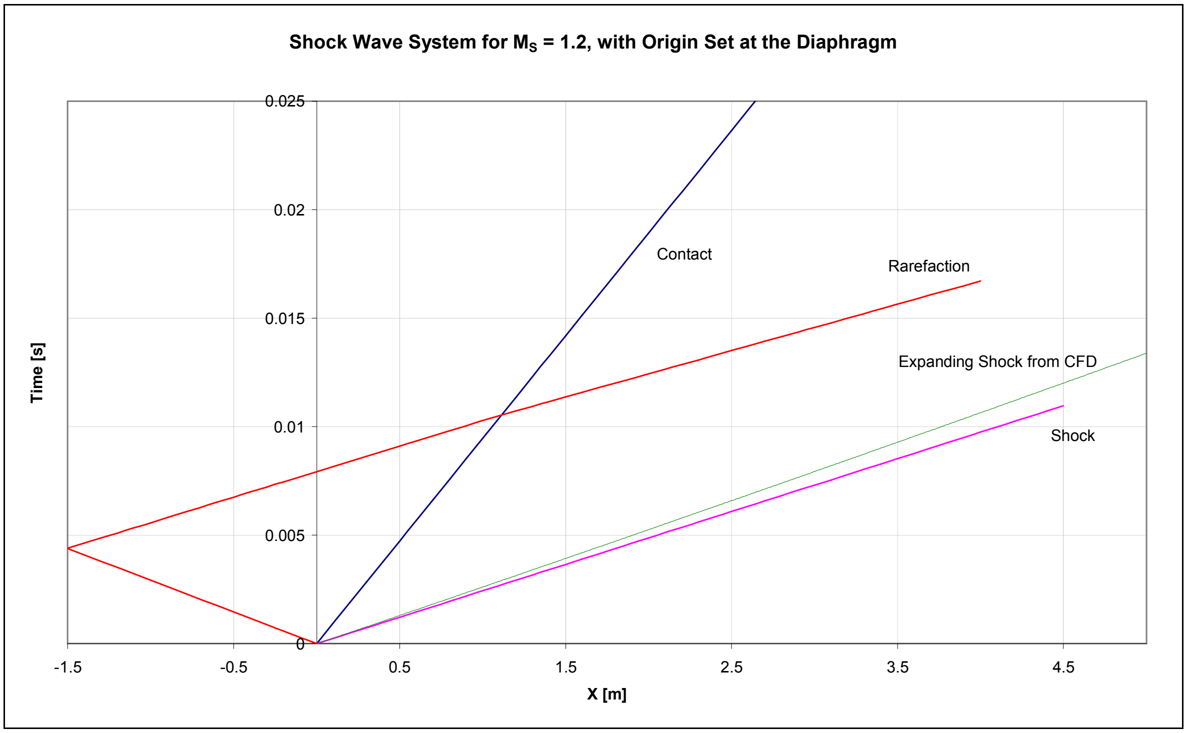

Figure 3.5.1 – Plot of the displacement versus time for the rarefaction and compression waves caused by the driver section, as well as the CFD plot of the shock wave, at an initial Mach number of 1.2

It is noted that the plots were produced for a constant cross-section tube, and a tapering section such as used on the actual tube would not drastically change the effects of rarefaction waves. This can be seen from the data points taken from the CFD results, which shows only a slight deviation from the linear curve. From these plots, it was decided that a driver section length of 1.5 m would be adequate.

The driver section was designed to take pressure differentials up to 6 bar, although in the weak shock tests to be conducted a maximum pressure differential of only 4 was required. The maximum pressure differential supplied by the low-pressure compressor available in the laboratory is 6 bar.

In order to have a 'clean' rupture of the diaphragm, it was decided to make the internal diameter of the driver section larger than the diagonal of the square-cross section of the downstream plunger section.

The internal diameter of the driver should therefore be larger than:

$$
\begin{aligned}
&d_i^2 \geq l^2 + b^2 = 100^2 + 100^2 \\
&\therefore d_i \geq \sqrt{20000} \\
&d_i \geq 141.42 \text{ mm}
\end{aligned}
$$

Two sections of round mild steel tubing with outer diameter of 168 mm were available, with wall thicknesses of the Schedule 40, 6 mm and Schedule 80, 10.97 mm. The Schedule 80 tubing was selected, as this would give an internal diameter of 146.06 mm.

Detailed design equations and explanations, as well as the engineering drawings of the driver section can be found in the Appendix C – Driver Section Design and Engineering Drawings.

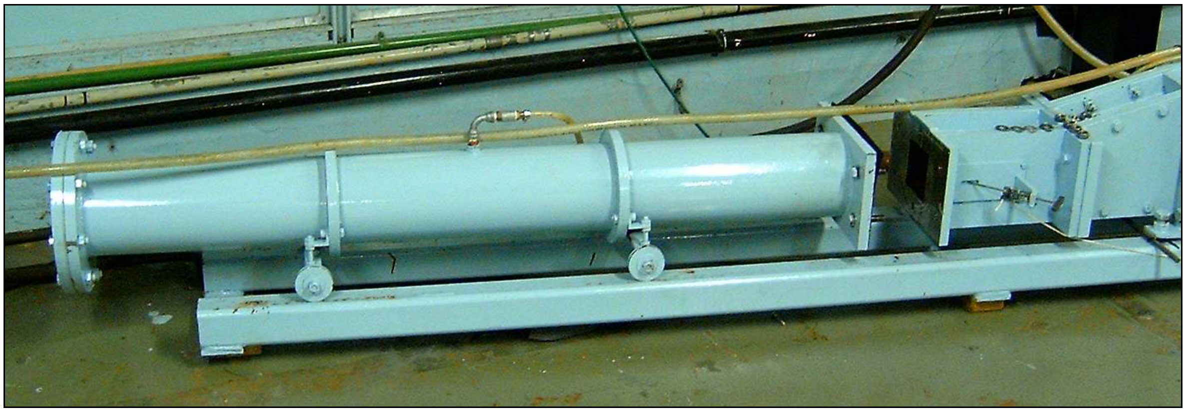

Figure 3.5.2 – Completed driver section of the shock tube

3.6. Plunger Section

A separate plunger section was designed to make the entire rig more modular, and therefore easily expandable. It was also considered to be easier to manufacture a separate section to mount the plunger than to machine extra holes in the large divergent section side wall. The plunger section is designed as in the same way as the original test section for commonality. The plunger consists of a simple, stainless steel needle, which is fired by a spring. The spring is first compressed and is kept in position by a simple catch. The plunger is triggered by the manual release of the catch, which then pricks the swollen diaphragm, causing it to rupture. Engineering drawing of the complete plunger section and mechanism can be found in the Appendix D – Plunger Section Engineering Drawings.

Figure 3.6 – Plunger Section showing separated driver section to the left, the armed plunger in the centre, and divergent section to the right.

3.7. Supports

The old shock tube supports were used to support the existing section, to prevent swaying during testing. The new divergent section was bolted to the original driver interface of the old section using 24 M14 bolts, which firmly secured the divergent section. A similar double-channel support was designed and constructed to act as a footprint for the new divergent section and as well as rails for the new driver section. Two new L-shaped supports were built to support the divergent section at its tapered end, by adjusting two M21 bolts which are in contact with the support rails.

Since the support channels had warped significantly from the welding process, two new adjustable supports were also built for the driver section. The driver supports consist of two wheels each, supported on a bracket which is differentially height-adjustable to compensate for the warping. Engineering drawings for the new supports are included in the Appendix E – Supports and Ports Engineering Drawings.

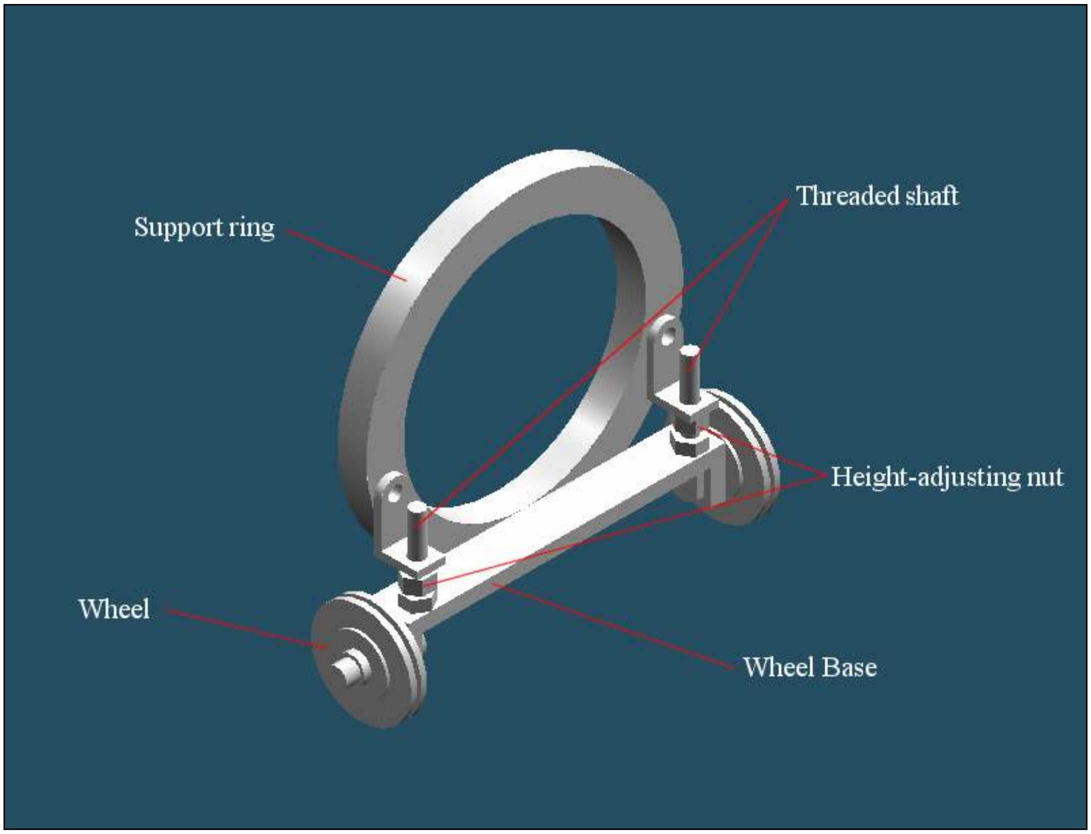

Figure 3.7 – Solid Edge © isometric view showing support ring of driver with wheel support

3.8. Completion of the Shock Tube Rig

The entire rig was complete by the end of July, 2004. The difficulty of moving the large sections became apparent, and if alterations or modifications on the existing sections are required in the future, some form of system to move the heavy (almost 1400 kg) divergent section will be needed.

The pressure transducer system was installed in August and preliminary tests were conducted to test different diaphragms and the suitability of the plunger and driver sections. A shadowgraph optical system was installed during September, and initial testing carried on through to October. This optical system did not reveal any promising results, and was thought to be not sensitive enough to reveal the region behind the triple point. During inspection of the driver section between test firings, cracks were found on the inner corners of the initial square tube section, thus halting any testing before a replacement round driver section was designed and built.

A far more sensitive schlieren optical system was installed in November during the halt in testing. The new driver section was completed and installed in early January 2005, and preliminary testing resumed immediately. Testing continued until May, during which far more consistent and promising results were obtained from the more sensitive optical system and improved driver. These results are presented later in Chapter 5 – Results.

4. Experimental Equipment and Procedures

4.1 The Shock Tube

The shock tube was designed for large-scale reflections using a cylindrical incident wave, and was built purposely for this project. The design and modification of the different sections are outlined in the previous chapter, Design Development. The complete shock tube consists of a driver section, plunger section, expanding divergent section, a constant area expansion section, and a constant area test section.

Below is a schematic diagram showing the internal dimensions (in mm) of the complete shock tube, as well as the position of the test section window centre.

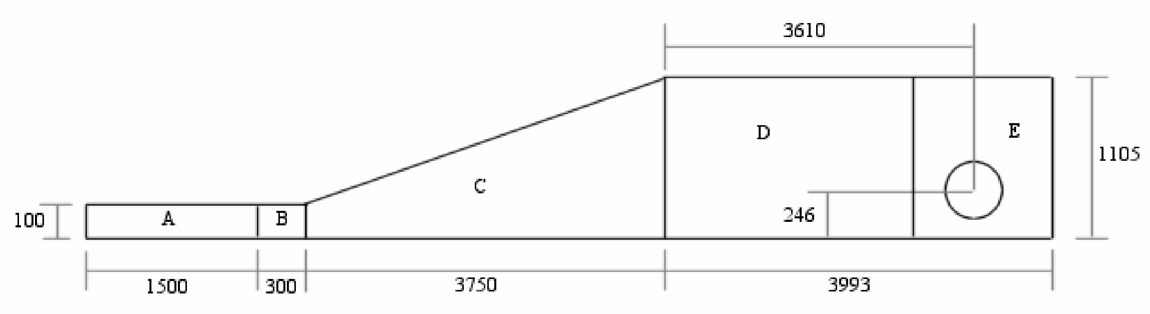

Figure 4.1.1 – Schematic of internal dimensions of the complete shock tube

In the above diagram:	A	is the driver section/compression chamber
	B	is the plunger section
	C	is the divergent section
	D	is the constant area expansion chamber
	E	is the constant area test section

The diaphragm is located between A and B.

The complete shock tube is 9.8 m long, stands 1.5 m high, and is approximately 1.5 m wide including supports.

The control console is located on the expansion section (D), close to the test section for convenience. The driver is supplied with compressed air from a low-pressure compressor, with a maximum 6 bar pressure differential, used in the Laboratory, via a control board:

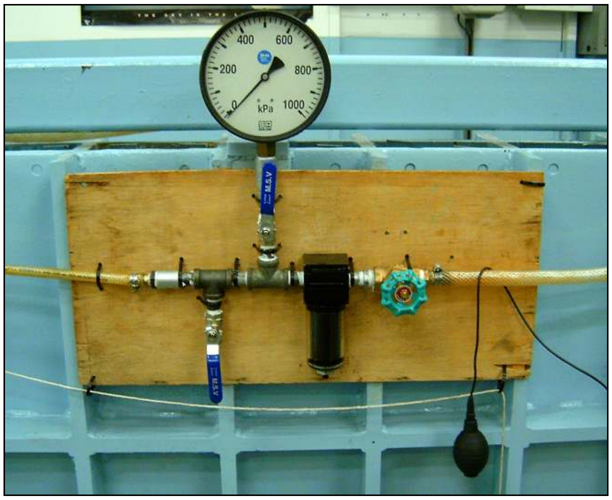

Figure 4.1.2 – Control console

The Control board consists of:

- An inlet hose from the low-pressure compressor
- A global-type ‘317’ variable inlet valve to control the flow of compressed air into the system
- An air filter, to filter any contaminants to the system
- A pressure gauge, to read the gauge pressure in the driver system
- A ball control valve, to open or close air to the pressure gauge
- A ball release valve, to release pressure from the system after tests or in an emergency
- An outlet hose which runs straight to the driver section.

The expansion chamber is open to atmospheric air, and is closed at the end of the test section with a hinged baffle. The test section consists of a rotating wall which houses two 312 mm diameter windows. Mach numbers ranging from 1.02 to 1.2 in the test section were achieved.

A more detailed explanation of each section can be found in the previous Chapter 3 – Design Development.

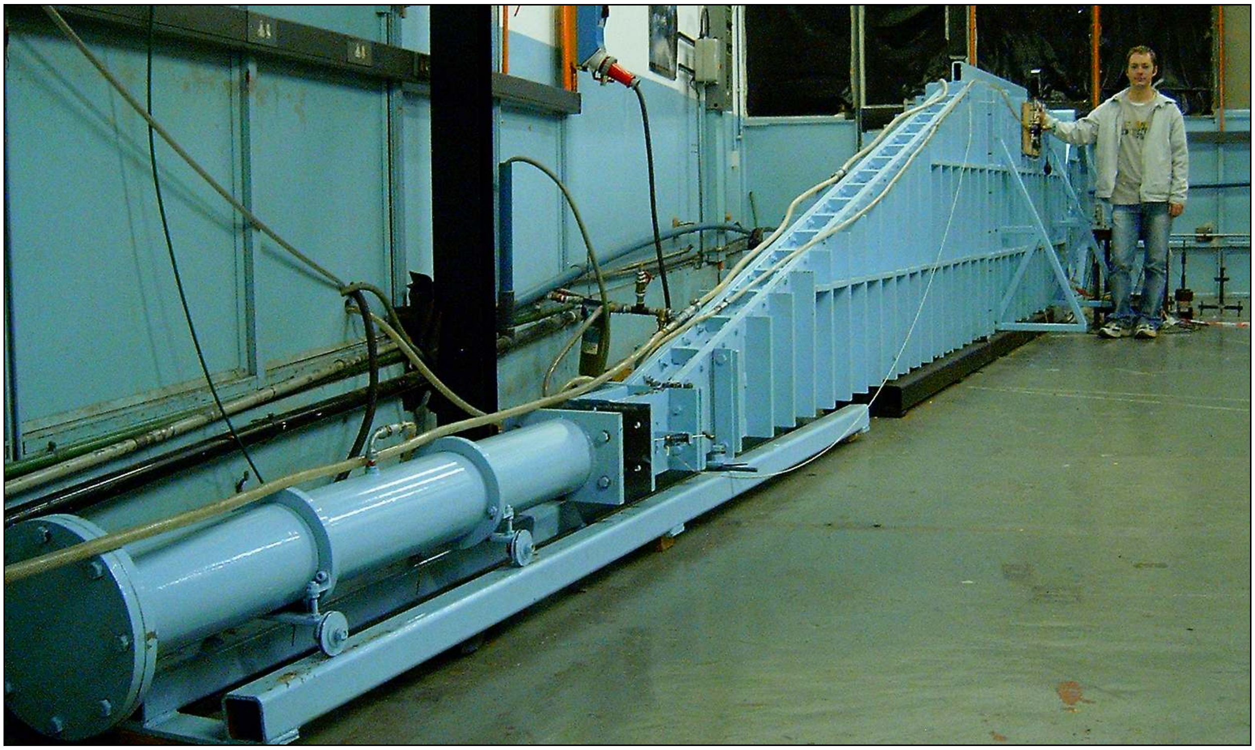

Figure 4.1.3 – Photograph of complete shock tube with the author standing next to the rig to demonstrate the scale of the equipment. The driver can be seen in the foreground.

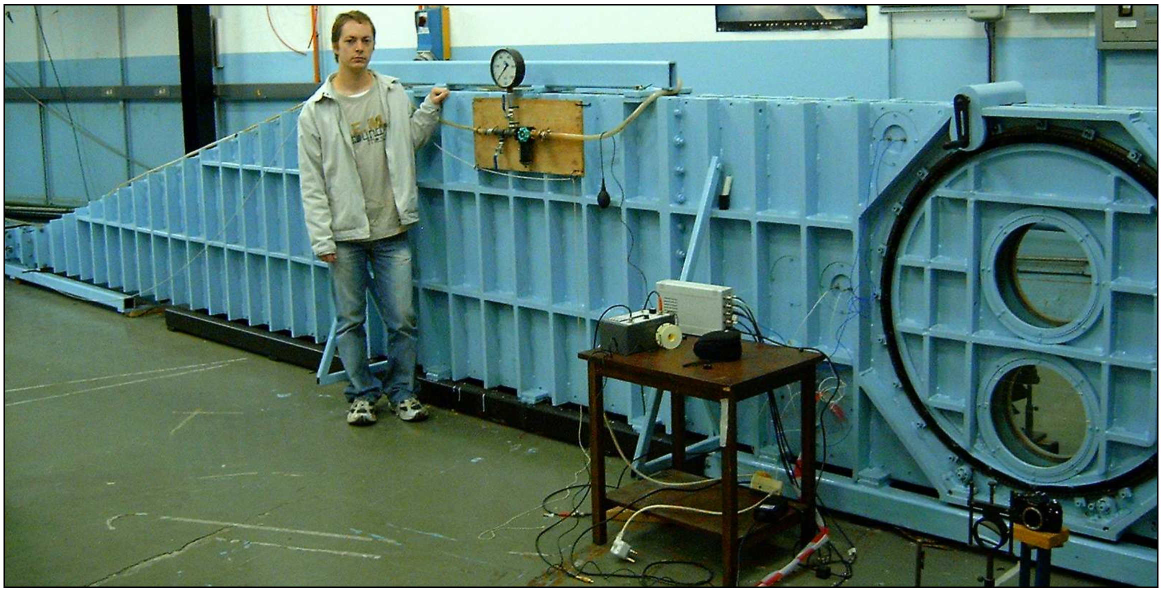

Figure 4.1.4 – Another view of the completed shock tube. The test section windows can be seen to the far right.

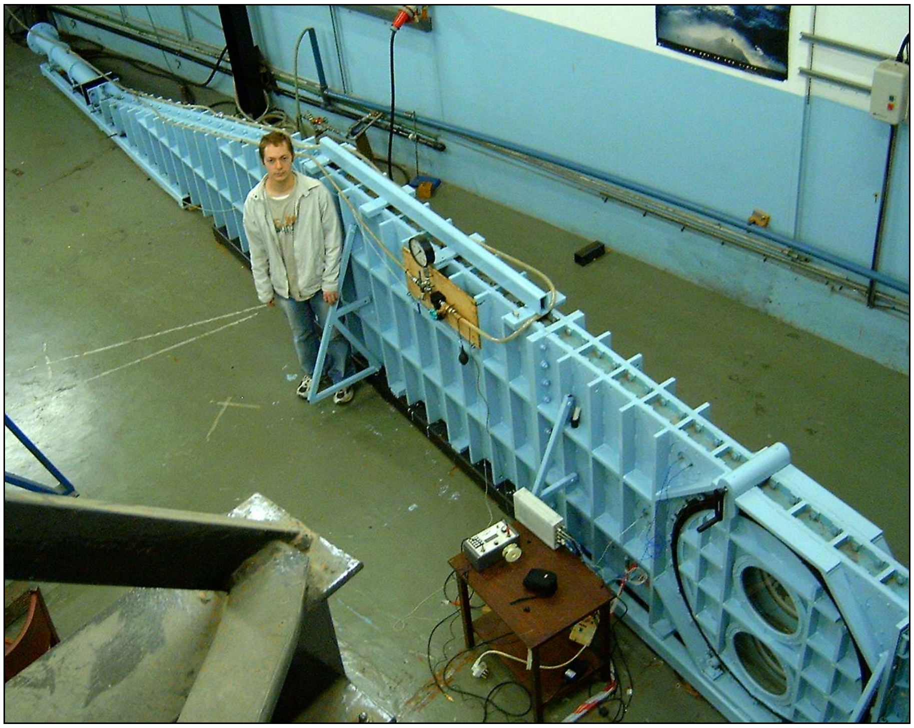

Figure 4.1.5 – Top view of the complete rig. The driver can be seen at the top left corner and the test section windows at the bottom right corner of the picture

4.2. Data Acquisition and Instrumentation

4.2.1. Pressure Measurement System

Pressure measurements inside the shock tube were measured using fast response PCB ICP sensor piezo-electric pressure transducers (Model 113A21). The signal from the pressure transducers were amplified by a PCB ICP sensor signal conditioner (Model 482A22) and the output signals were then sent to a Yokogawa DL708E digital scope where the signal voltage was plotted against time, and recorded for data processing.

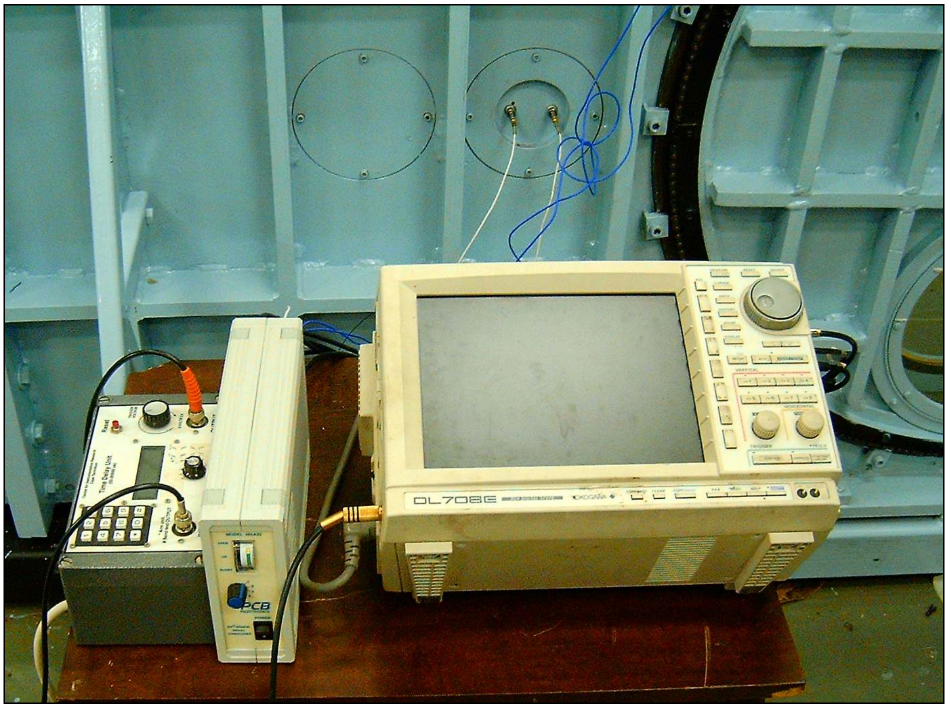

Figure 4.2.1 – Equipment setup, from left to right: Time Delay Unit, Signal Conditioner and Digital Scope. Pressure transducers for Channels 1 and 2 can be seen in the background

Four pressure transducers were placed in port positions just ahead of window test section as shown in the diagrams below:

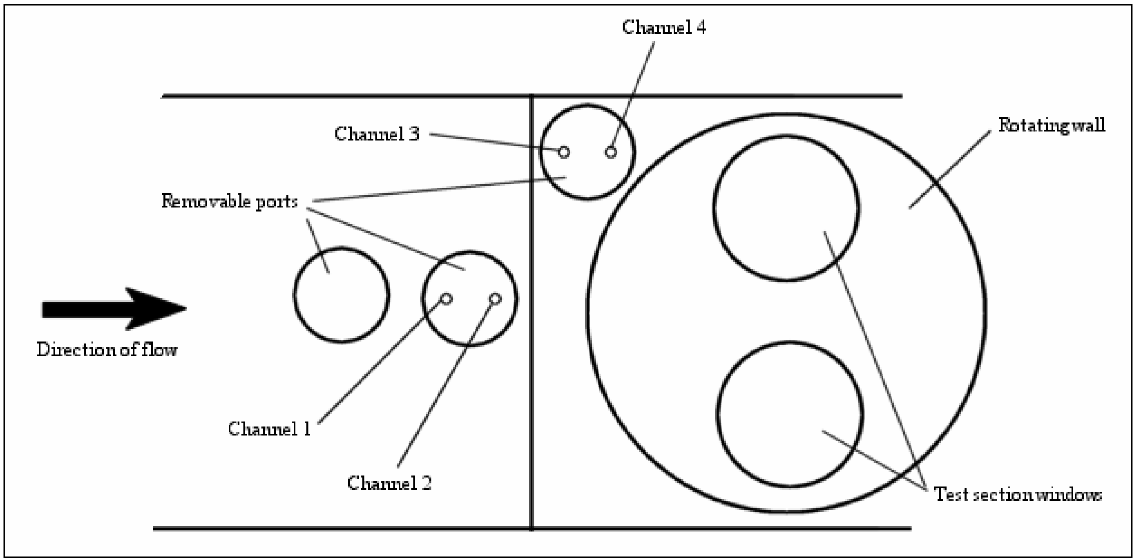

Figure 4.2.2 – Configuration of pressure transducer channels on shock tube

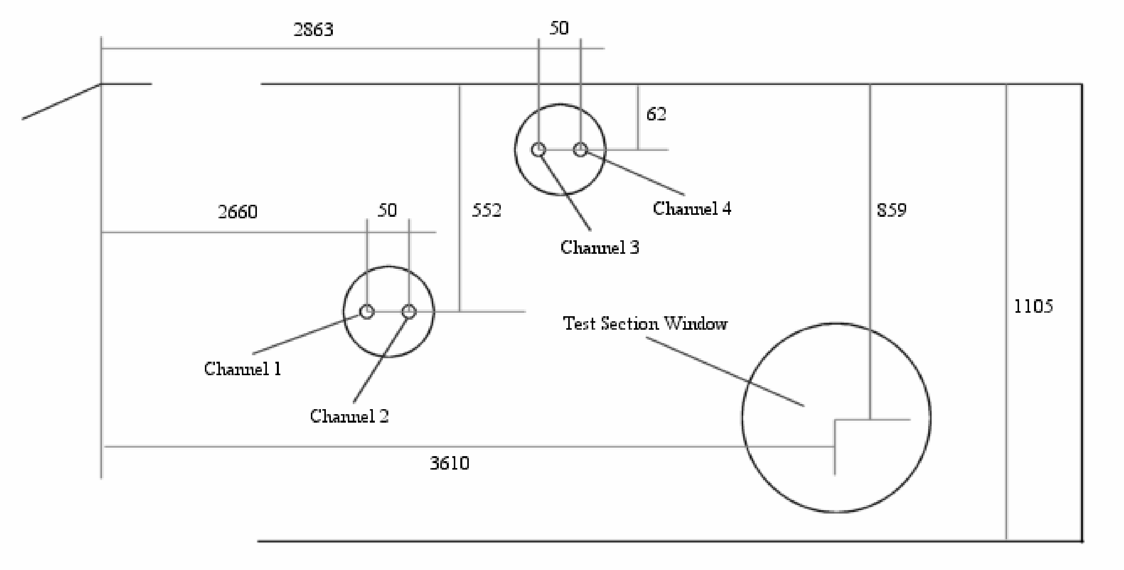

Figure 4.2.3 – Position of transducer ports and test window with respect to the reflection corner

New removable ports were designed to accommodate the pressure transducers. Channels 1 and 2 were used to measure the pressure of either the incident wave or Mach stem, depending on whether the triple point passed above or below the transducers. Similarly, channels 3 and 4 were used to measure the pressure of the Mach stem as it passed by the transducers.

4.2.2 Output Signal

The oscilloscope was also used to send a trigger output to a time delay unit. The time delay was set to a specific time (around 2000 μs), after which time the unit would send an output signal to the optical system once a shock had been detected at channel 1.

4.3. Optical System

A shadowgraph system was initially used to obtain photographs of the shock wave reflection as it passed the test section window. Later a schlieren system was used, which differs from a shadow graph by passing light past a carefully positioned knife-edge.

A schlieren system displays changes in the refractive index distribution of transparent media such as the flow of air. The refractive index distribution can be related to changes in the density, temperature, or pressure distributions in the flow. Since the density and pressure change abruptly across the interface of a shock wave, a shock wave is distinctly identified in such a system.

A 1 μs xenon flash lamp was used as a light source and passed through a thin vertical slit, and then collimated (light rays made parallel) by parabolic mirrors. The collimated light was passed through the test section windows (and hence through the flow under investigation) and brought to a focus. A vertical knife-edge was placed at the focus point, and carefully positioned so some of the light is blocked. The light which passes the knife-edge is once again collimated with the use of a lens and is photographed directly with a camera. Vertical slits and knife-edges were used, since this configuration produces higher sensitivity, and therefore more defined images for vertical shock waves, which are predominant in the reflection under study. The flash lamp was triggered by the output signal of the time delay box.

If the flow is uniform, the resulting image will be uniformly bright. If however, there are changes in density, temperature, or pressure; the light which passed through these refractive index variations would be either be blocked by the knife-edge, rendering dark areas on the image, or cause more light to pass the knife-edge, rendering lighter areas on the image.

A Nikon MF-12 35mm Analogue Camera was used to obtain photographs of the shock reflection as it passed the test section window.

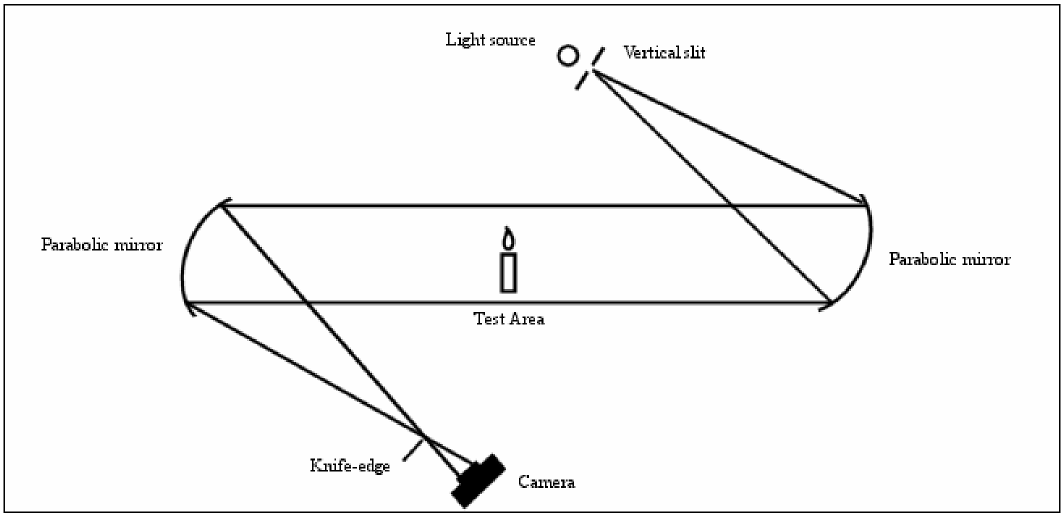

Figure 4.3.1 – Schematic of a basic Z-configuration schlieren system

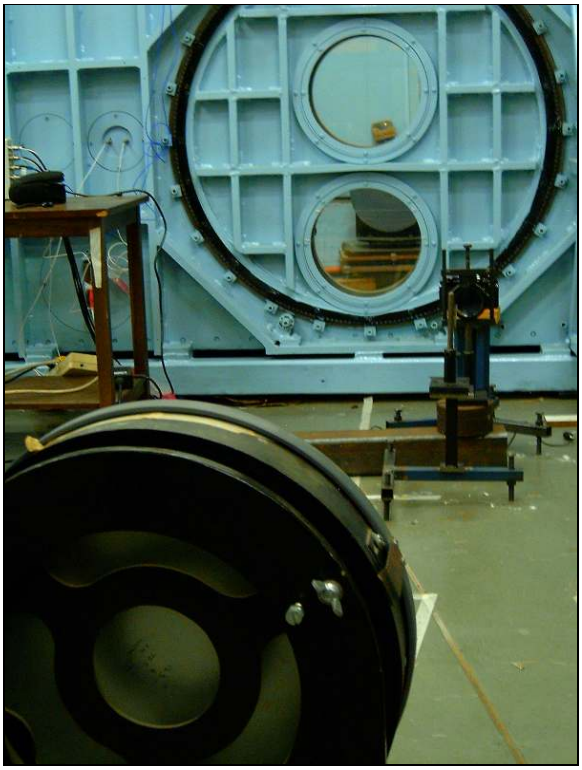

Figure 4.3.2 - Optical system showing the large parabolic mirrors (protected with grey PVC covers) in the fore- and back-ground, and the camera setup to the right of the window.

4.4. Operation of the Shock Tube

The atmospheric temperature was measured using a standard mercury thermometer, with a resolution of ± 0.5°C. The atmospheric air pressure was recorded using a digital barometer with an accuracy of ±0.01 kPa.

4.4.1. Testing Procedure

The following procedure was used for each test of the shock tube:

1. All the instrumentation was switched on and given sufficient time to reach operating conditions (for calibration of the oscilloscope etc.)
2. The driver section was moved back and the test section exit buffer was opened. The test section was then blown with high-pressure air to remove any diaphragm fragments from previous test firings. This was accomplished by detaching the hose connected to the control board and feeding it down the test section from the divergent section inlet. The hose is then re-connected and the exit buffer is closed.
3. The lights were switched off and the knife-edge of the schlieren optical system was adjusted to obtain the required sensitivity and light conditions for the photographs.
4. The lights were switched back on and the inlet valve to the system was closed to prevent air flow to the driver section.
5. The plunger was compressed back and the catch was positioned in the cocked position. A section of cellophane material was taped to the open end of the driver section to act as a diaphragm. The driver section was then moved forward and bolted to the inlet of the plunger section.
6. The camera was armed, the camera-flash trigger delay was selected, and the oscilloscope was set to record the pressure traces at the passing of a shock wave past the first transducer.
7. The inlet valve was opened, and the driver section was pressurized to the required internal pressure. The lights were turned off, a whistle was blown to warn of a test firing (giving passers-by adequate time to block their ears), the camera shutter was opened, and the plunger catch was released, triggering the shock test.
8. After a successful test, implied by the observation of a flash of the camera-flash equipment, the camera shutter was closed and the lights were switched back on.

5. Results

5.1 Data Processing

Before each test was conducted, a test run table was filled in, which recorded the date, ambient temperature (T_{atm}) and pressure (P_{atm} or P_1), the driver internal pressure (P_4), the selected camera-flash trigger delay, test-, film- and photograph-number. All these are required for data processing at a later stage, and to correlate data with the photographs obtained.

Pressure traces were obtained from the pressure transducers and displayed on a Yokogawa digital scope. These traces were saved to disc according to a specific filename sequence, 'Ammddxxx', where:

mm	is the month of the test
dd	is the day of the test, and
xxx	is the number of the test conducted on that day

These output files were then converted into MS Excel spreadsheet data tables, and processed in order to determine the Mach number of the Mach stem shock waves.

The triple point was required to pass through the test section window and therefore the test section wall was rotated so that the window was closest to the floor of the test section, in order to achieve maximum Mach stem length. This meant that on most successful tests, the triple point passed just below the first and second channels. Since all the tests were conducted with very weak, almost planar shocks (M = 1.023 - 1.129 in the test section), the Mach stem Mach number recorded at channels 1 and 2 would be approximately equal to the Mach number of the incident wave.

The actual values of the Mach numbers of the waves would be slightly less at the point where the reflection reaches the test window, as this is 950 mm and 900 mm downstream of channels 1 & 2 respectively. From the CFD results, it can be seen that this decay is very slight, and would be in the order of $\Delta M = -0.01$.

Summarized versions containing the resultant shock Mach numbers of the Mach stem for values of approximate initial driver Mach number were plotted.

Photographs were taken for every test, where possible. Cotton threads were fixed across the test window at 260 mm and 340 mm from the shock tube floor to accurately determine the height of the triple point as it passed the test windows.

Triple point heights were then plotted against the Mach numbers at channels 1 & 2, and channels 3 & 4.

5.2. Sample Test Run Calculation

Date: 21 April 2005
Test: 005 (6th test that day)
Film: #8
Photo: #9
Filename: A0421005.asd (raw data)
A0421005.xls (processed data)

P_{atm} (P_1) = 82.98 kPa
T_{atm} (T_1) = 19.5°C = 292.7 K
$P_{initial}$ (P_4) = ~140 kPa
Delay time = 2000 μs

The differential pressure ratio the driver section is pressurized to is:

$$P_{41} = \frac{P_4 + P_1}{P_1}$$
$$= 2.6872$$

The Mach number across a shock is given by:

$$M_s = \sqrt{\frac{1 + 6\lambda_s}{7}}$$

where: M_s is the Mach number across the shock
λ_s is the pressure ratio across the shock

From this we can approximate the Mach number of the plane shock wave entering the divergent section using the theoretical equation:

$$P_{41} = \lambda_s\left(1 - \left[(\lambda_s - 1)\sqrt{\frac{1}{7(1+6\lambda_s)}}\right]\right)^{-7}$$

so for $P_{41} = 2.6872$,

$\lambda_s = 1.6097$

$\therefore M_s = 1.234\ (M_{initial})$

In reality the initial Mach number would be approximately 10% less due to inefficiencies.

Ambient speed of sound (for Mach 1):

$$\begin{aligned} a_s &= \sqrt{(1.4)(287)(292.7)} \\ &= 342.9\ \text{m/s} \end{aligned}$$

The output voltages from the four channels are tabulated and converted to pressures using the following formula:

$$P_n = \frac{V_n \times 1000}{k}$$

where: P_n is the dynamic (recorded) pressure at channel n [kPa]
V_n is the voltage recorded at channel n [mV]
k is the calibration constant unique to each pressure transducer [mV/kPa]

The pressure ratio across a shock at each channel was then calculated using the formula:

$$\lambda_n = \frac{P_1 + P_n}{P_1}$$

where: λ_n is the pressure ratio at channel n

The Mach number at each channel was then determined:

$$M_n = \sqrt{\frac{1 + 6\lambda_n}{7}}$$

where: M_n is the Mach number at channel n

These values were all tabulated, and plots of the pressure traces, and Mach number of the four channels were plotted in the spreadsheets. An example of the Mach number traces is given overleaf in Figure 5.2.

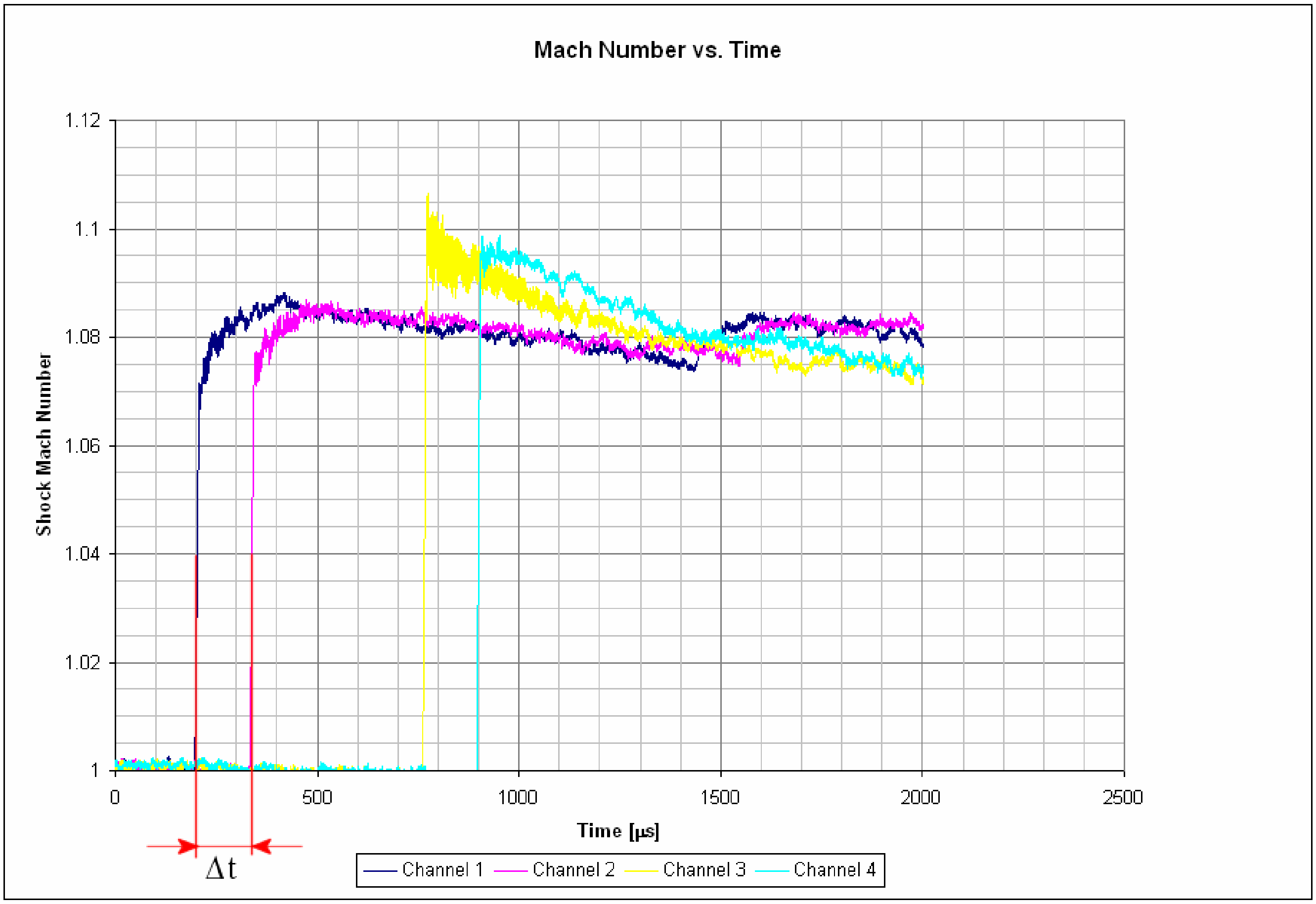

Figure 5.2 – Shock Mach number traces for four channels versus time, showing time elapsed between channels 1 & 2 in red.

The Mach number of the actual shock passing the channels was determined by obtaining the elapsed time between observed step rises in the voltages of two grouped channels (shown in red), and working out the corresponding speed of the shock between the two channels. Taking the ratio of this speed with the ratio of the speed of sound in the ambient conditions, the Mach number of the shock was determined.

Continuing with the current example,

$t_1 = 202.6$ µs

$t_2 = 338.8$ µs

$\Delta x_{12} = 50$ mm

$$\therefore v_{12} = \frac{\Delta x_{12}}{\Delta t_{12}} = \frac{0.05}{(338.8 - 202.6) \times 10^{6}}$$
$$= 367.1\ \mathrm{m/s}$$

$$\therefore M_{12} = \frac{v_{12}}{a_s}$$
$$= 1.071$$

A similar procedure is used to determine M_{34}.

Channels 1 and 2 were used to determine the Mach number of the Mach stem Shock wave just above the triple point, while channel 3 and 4's pressure traces were used in a similar way to determine the Mach number of the Mach stem close to the roof of the test section. The difference between these two values was generally between 1 and 2%.

5.3 Data Results Tables and Figures

The complete set of quantitative data is tabulated and plotted below. Although all these experiments had corresponding schlieren photographs of the test section, not all of the photos captured the triple point.

Table 5.3 – Table of results

P_4	$M_{initial}$	DataFile	M_{12}	M_{34}
200	1.297	A0425002	1.113	1.129
200	1.297	A0421004	1.113	1.129
200	1.297	A0329001	1.109	1.128
200	1.297	A0329002	1.094	1.114
200	1.296	A0323002	1.105	1.124
200	1.296	A0323001	1.107	1.124
180	1.277	A0426005	1.090	1.113
180	1.277	A0421002	1.094	1.116
180	1.276	A0428000	1.092	1.114
170	1.268	A0425001	1.089	1.108
170	1.267	A0426004	1.089	1.110
170	1.267	A0421001	1.087	1.109
170	1.266	A0428001	1.084	1.110
160	1.257	A0425004	1.084	1.108
160	1.257	A0425005	1.082	1.105
160	1.256	A0426003	1.084	1.107
150	1.246	A0309003	1.073	1.100
150	1.245	A0309000	1.074	1.099
150	1.245	A0309001	1.074	1.099
150	1.245	A0309002	1.073	1.093
150	1.245	A0426002	1.078	1.103
150	1.245	A0413001	1.075	1.101
150	1.244	A0503000	1.075	1.100
150	1.244	A0428002	1.079	1.102
140	1.235	A0425000	1.073	1.098
140	1.235	A0412006	1.069	1.097
140	1.234	A0309005	1.073	1.097
140	1.234	A0309004	1.069	1.097
140	1.234	A0421005	1.071	1.100
140	1.234	A0426001	1.074	1.099
140	1.234	A0421000	1.071	1.099
140	1.233	A0414002	1.075	1.099
130	1.223	A0425003	1.065	1.097
130	1.222	A0426000	1.066	1.096
130	1.222	A0413004	1.065	1.094

130	1.222	A0413005	1.063	1.094
130	1.222	A0310002	1.066	1.095
130	1.222	A0310000	1.064	1.096
130	1.222	A0310001	1.064	1.095
130	1.221	A0503001	1.065	1.095
130	1.221	A0503002	1.064	1.094
130	1.221	A0414001	1.065	1.096
120	1.210	A0412004	1.060	1.090
120	1.210	A0310003	1.063	1.094
120	1.210	A0310004	1.063	1.094
120	1.210	A0310005	1.062	1.094
120	1.210	A0315000	1.063	1.095
120	1.209	A0413000	1.062	1.091
120	1.209	A0413002	1.062	1.091
100	1.184	A0412005	1.057	1.084
100	1.184	A0315002	1.057	1.085
100	1.184	A0315003	1.057	1.084
100	1.184	A0413003	1.054	1.082
100	1.183	A0315001	1.057	1.084
80	1.155	A0412002	1.047	1.076
80	1.155	A0315004	1.049	1.077
80	1.155	A0404000	1.050	1.076
80	1.155	A0404002	1.047	1.078
80	1.155	A0404001	1.044	1.078
80	1.152	A0414000	1.048	1.078
70	1.140	A0411000	1.045	1.070
60	1.124	A0412001	1.038	1.065
60	1.123	A0411001	1.042	1.068
60	1.123	A0411002	1.042	1.067
50	1.106	A0411003	1.033	1.057
40	1.088	A0412000	1.032	1.054
40	1.088	A0411005	1.029	1.053
40	1.088	A0411004	1.027	1.048
30	1.069	A0411006	1.027	1.047
20	1.047	A0411007	1.023	1.039

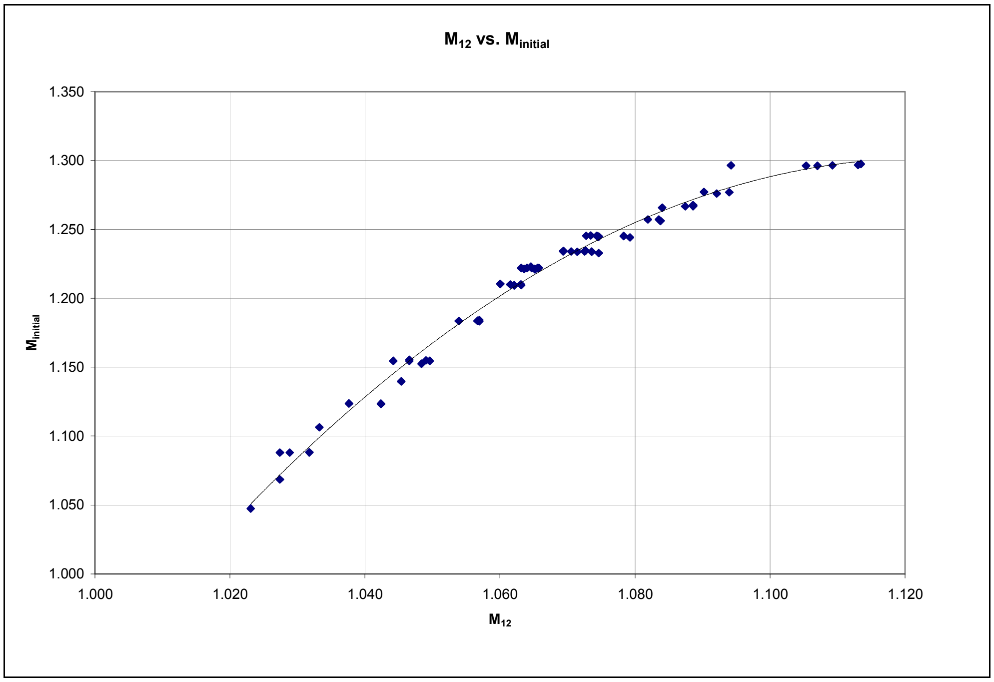

Figure 5.3.1 – Mach number recorded between Channels 1 and 2 versus the initial Mach number

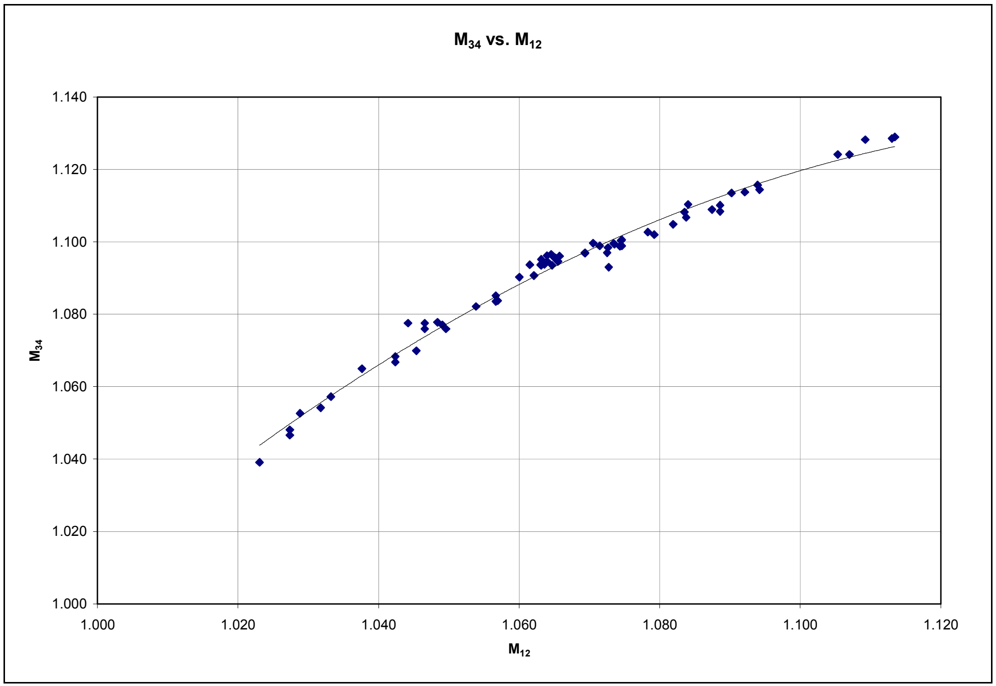

Figure 5.3.2 - Mach number recorded between Channels 3 and 4 versus Mach number recorded between Channels 1 and 2

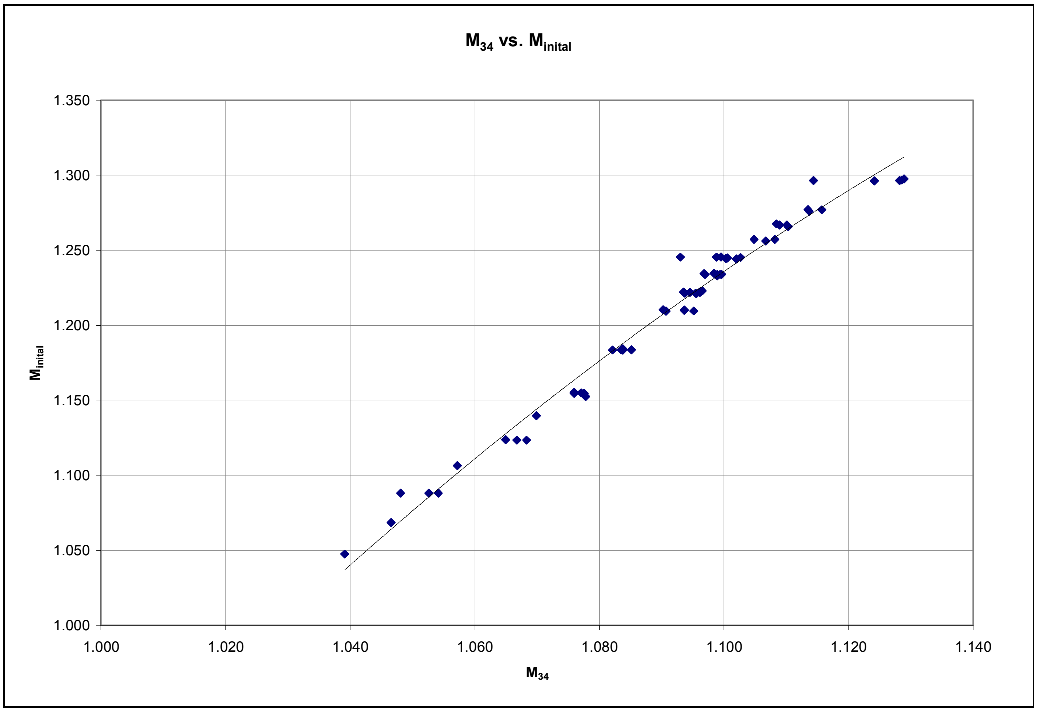

Figure 5.3.3 – Mach number recorded between Channels 3 and 4 versus the initial Mach number

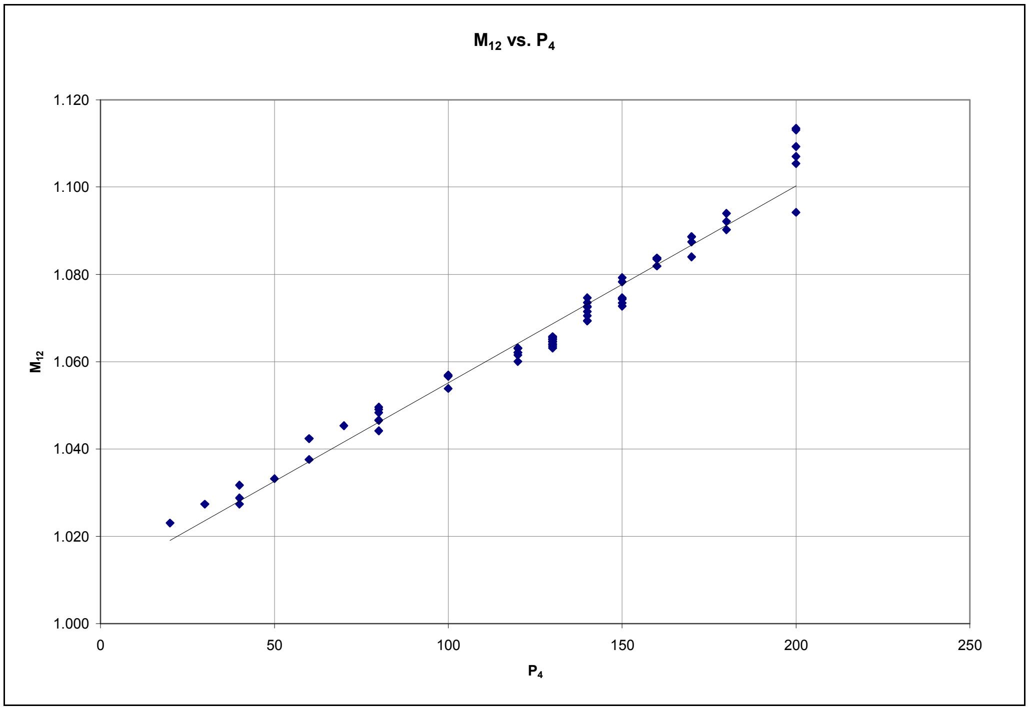

Figure 5.3.4 – Mach number recorded between Channels 1 and 2 versus driver initial pressure

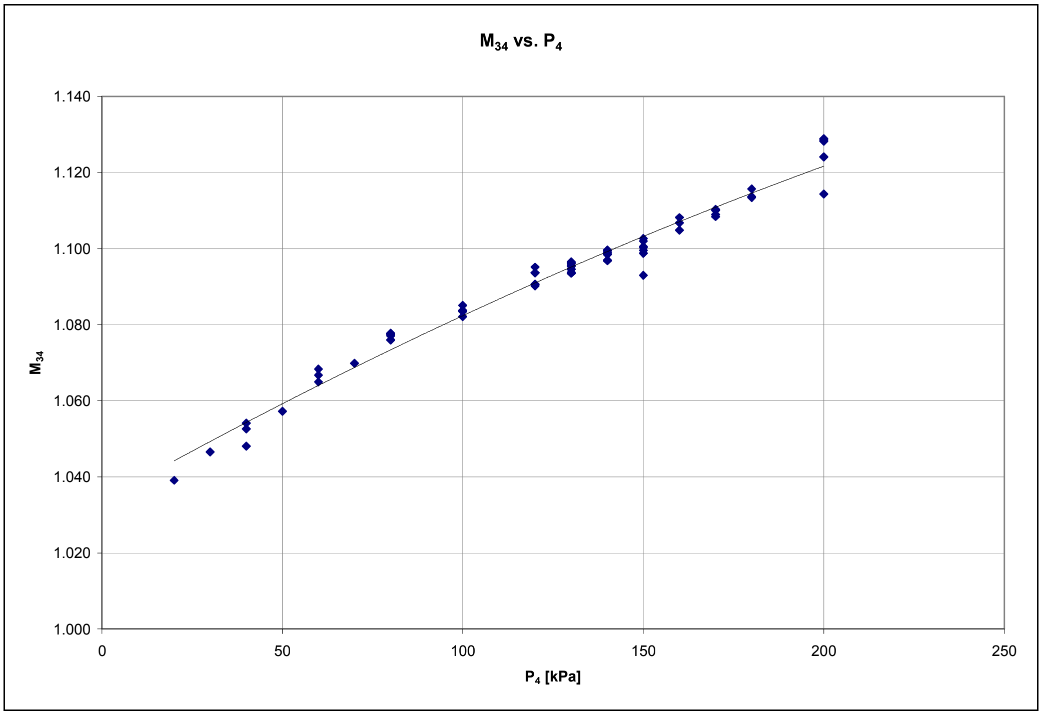

Figure 5.3.5 – Mach number recorded between Channels 3 and 4 versus driver initial pressure

5.4. Results from the Schlieren Photographs

The schlieren photographs were used to visualize the triple point region. This was the most important part of the study, since it was the main objective of the project.

From the photographs, the height of the triple point, and hence the Mach stem, was determined. It is important to note the weak reflection is 'upside down' compared to the schematic diagrams conventionally produced in textbooks. In this shock tube, the roof acts as the wedge surface.

In the table below, only the data sets where a triple point was pictured are presented, along with the photo identification and an estimation of the triple point position relative to the reflection corner.

Table 5.4 – Summarised results of test runs with triple point visualisation

Photo	P_4 [kPa]	$M_{initial}$	M_{12}	M_{34}	Datafile	MS Length (Y) [mm]	X Position [mm]
C21	180	1.277	1.090	1.113	A0426005	836	3642
C6	180	1.277	1.094	1.116	A0421002	850	3646
C22	180	1.276	1.092	1.114	A0428000	842	3644
C7	170	-	-	-	A0421003	821	3643
C11	170	1.268	1.089	1.108	A0425001	820	3641
C20	170	1.267	1.089	1.110	A0426004	825	3642
C5	170	1.267	1.087	1.109	A0421001	819	3642
C23	170	1.266	1.084	1.110	A0428001	815	3640
C14	160	1.257	1.084	1.108	A0425004	801	3640
C15	160	1.257	1.082	1.105	A0425005	797	3639
C19	160	1.256	1.084	1.107	A0426003	798	3638
A9	150	1.246	1.073	1.100	A0309003	769	
A6	150	1.245	1.074	1.099	A0309000	773	
A7	150	1.245	1.074	1.099	A0309001	772	
A8	150	1.245	1.073	1.093	A0309002	766	
C18	150	1.245	1.078	1.103	A0426002	774	3636
B29	150	1.245	1.075	1.101	A0413001	765	3637
C25	150	1.244	1.075	1.100	A0503000	772	3635
C24	150	1.244	1.079	1.102	A0428002	774	3638
C10	140	1.235	1.073	1.098	A0425000	759	3637
B27	140	1.235	1.069	1.097	A0412006	755	3631
A11	140	1.234	1.073	1.097	A0309005	766	
A10	140	1.234	1.069	1.097	A0309004	762	
C9	140	1.234	1.071	1.100	A0421005	754	3635
C17	140	1.234	1.074	1.099	A0426001	754	3633

C4	140	1.234	1.071	1.099	A0421000	755	3635
B36	140	1.233	1.075	1.099	A0414002	757	3637
C13	130	1.223	1.065	1.097	A0425003	730	3631
C16	130	1.222	1.066	1.096	A0426000	724	3628
B32	130	1.222	1.065	1.094	A0413004	731	3633
B33	130	1.222	1.063	1.094	A0413005	728	3633
A14	130	1.222	1.066	1.095	A0310002	746	
A12	130	1.222	1.064	1.096	A0310000	744	
A13	130	1.222	1.064	1.095	A0310001	732	
C26	130	1.221	1.065	1.095	A0503001	727	3629
C27	130	1.221	1.064	1.094	A0503002	715	3626
B35	130	1.221	1.065	1.096	A0414001	723	3632
B25	120	1.210	1.060	1.090	A0412004	711	3668
A15	120	1.210	1.063	1.094	A0310003	727	
A16	120	1.210	1.063	1.094	A0310004	727	
A17	120	1.210	1.062	1.094	A0310005	715	
A20	120	1.210	1.063	1.095	A0315000	722	
B28	120	1.209	1.062	1.091	A0413000	695	3626
B30	120	1.209	1.062	1.091	A0413002	694	3628

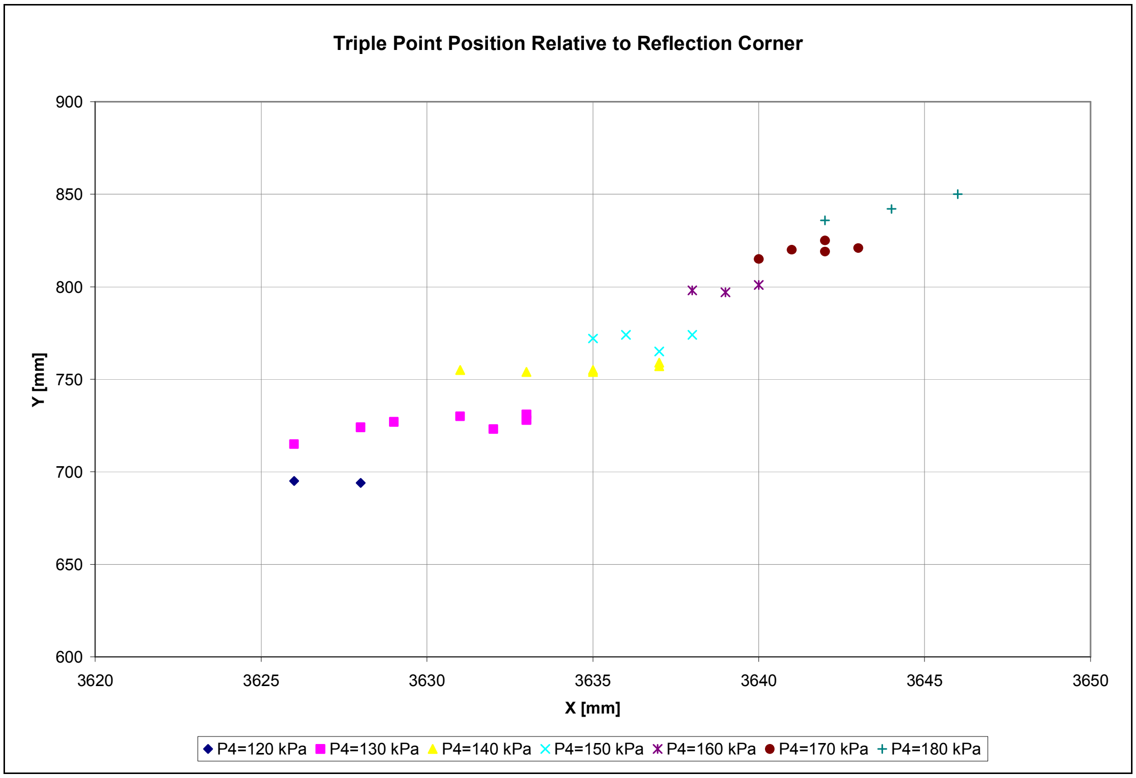

Figure 5.4.1 – Triple point position, relative to the reflection corner for various initial driver pressures

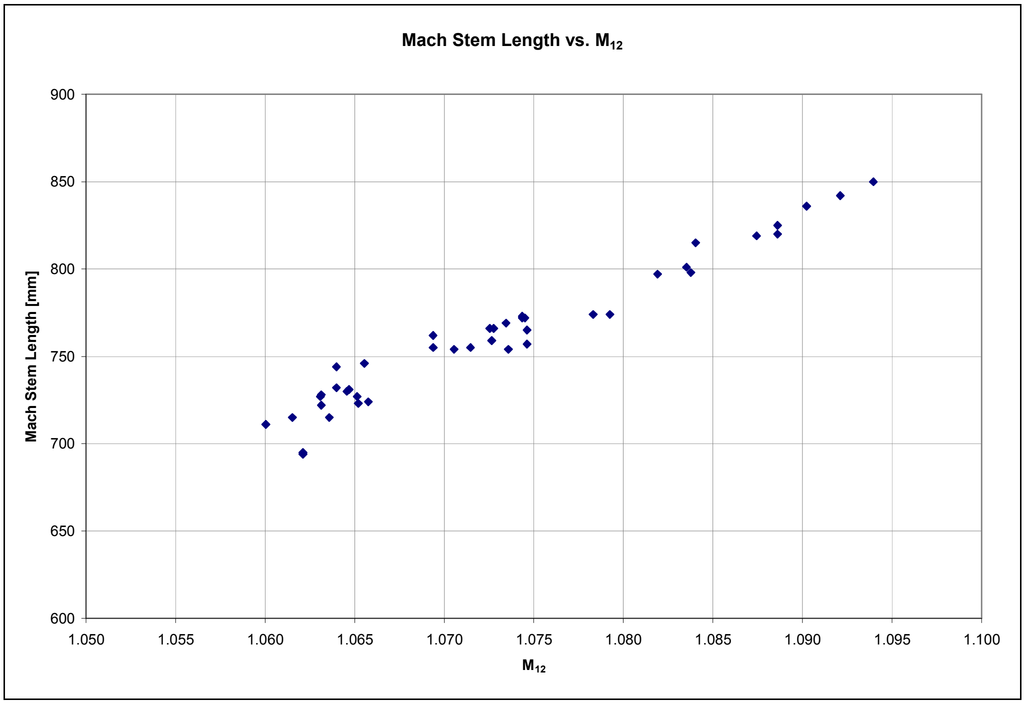

Figure 5.4.2 – Mach Stem Length versus Mach number recorded between Channels 1 and 2

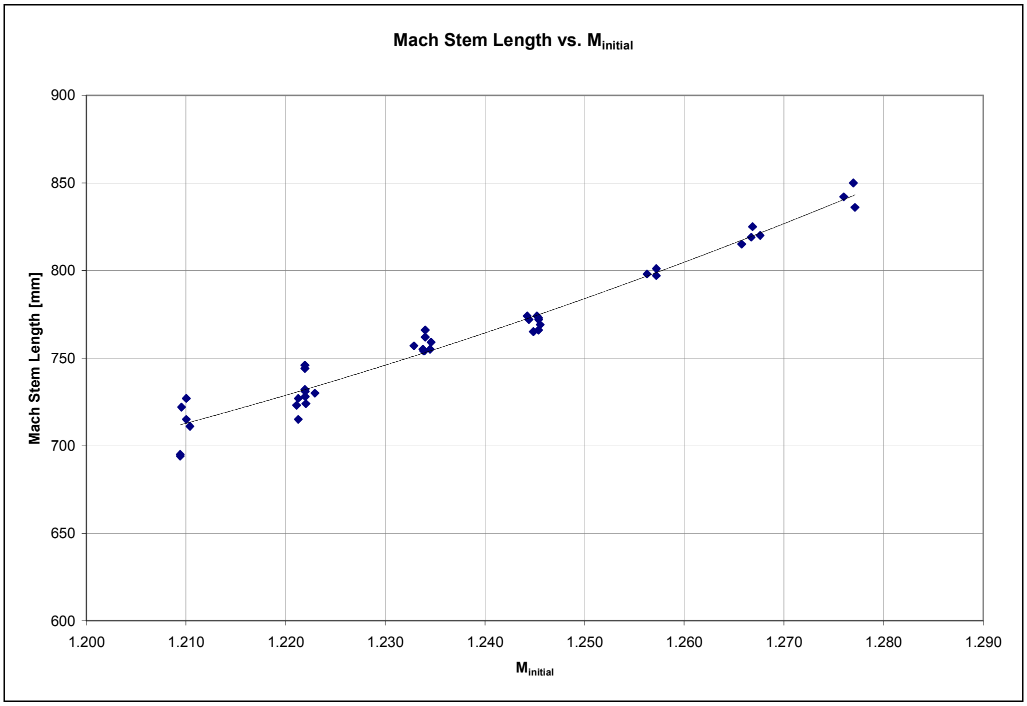

Figure 5.4.3 – Mach Stem Length versus initial driver Mach number

The configuration of the reflection is described by the schematic diagram given below.

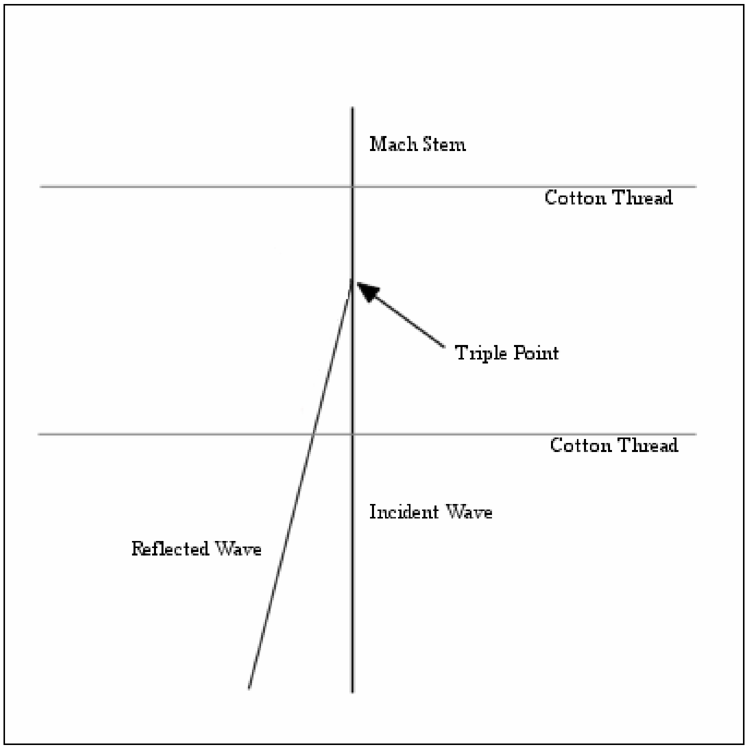

Figure 5.4.4 – Schematic representation of the reflection in the test window

The following photographs are examples of the photographs taken for a few of the test runs. All the enhanced images from the test runs are given in the Appendix F – Schlieren Photographs.

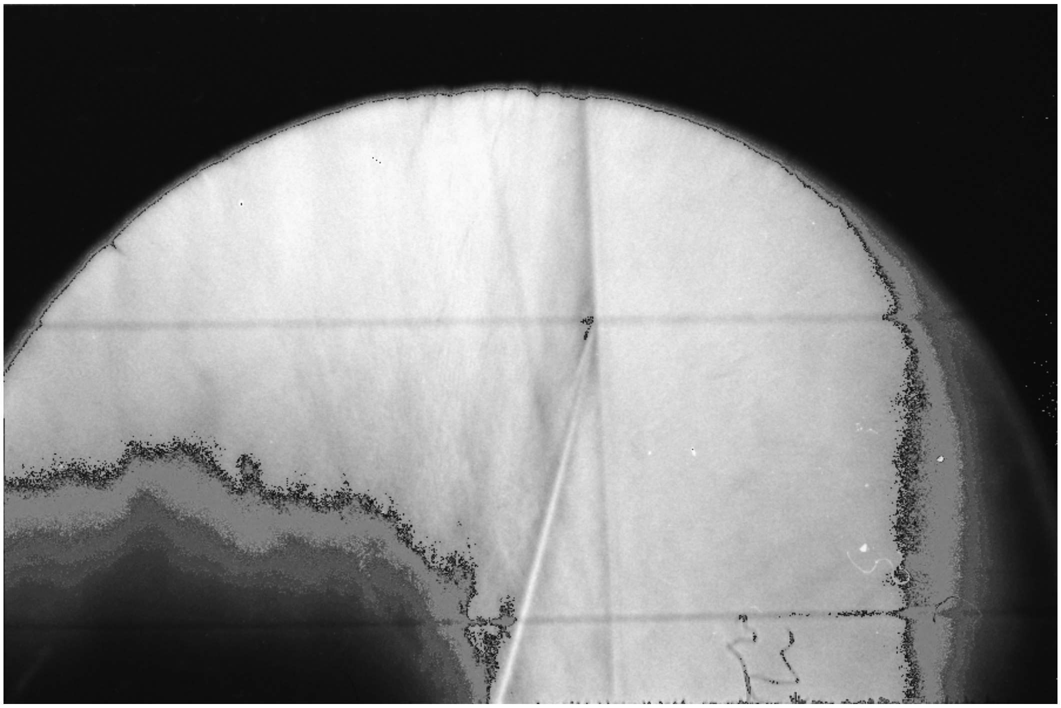

Figure 5.4.5 – Photograph number B29, $M_{12} = 1.075$, $M_{34} = 1.101$, Mach stem length = 765 mm

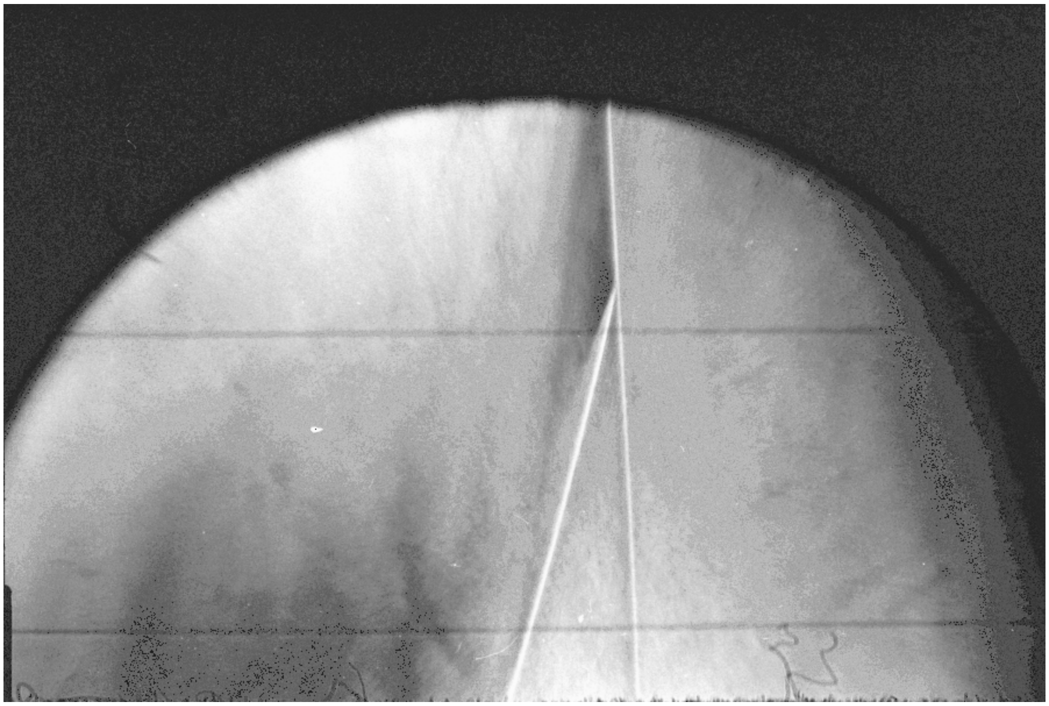

Figure 5.4.6 – Photograph number C17, $M_{12} = 1.074$, $M_{34} = 1.099$, Mach stem length = 754 mm

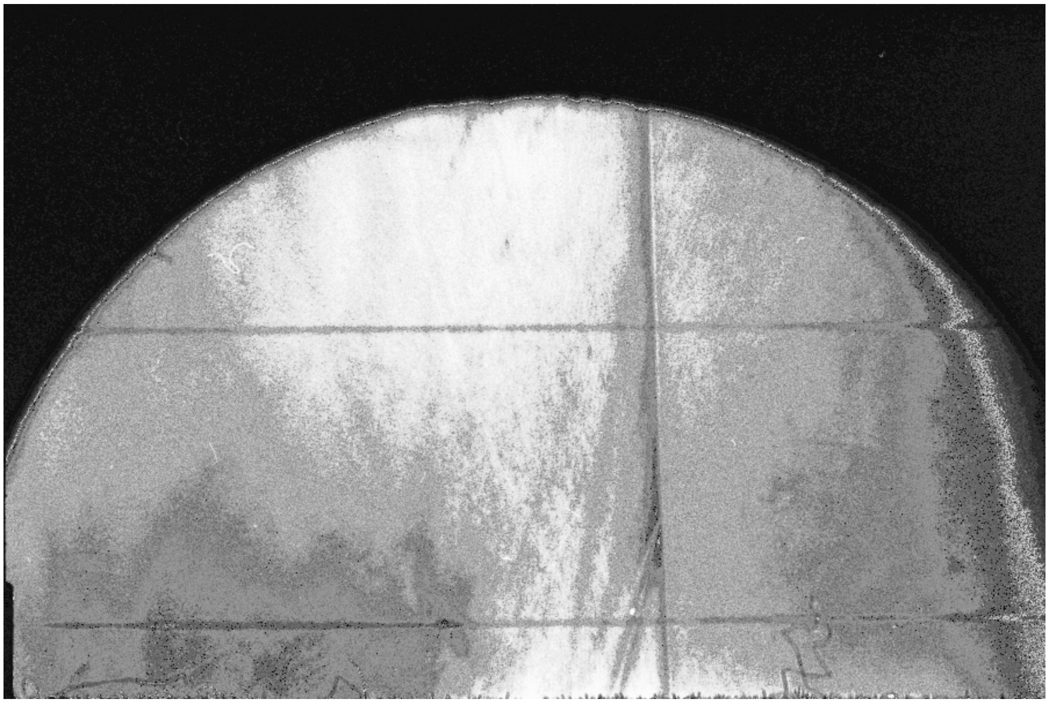

Figure 5.4.7 – Photograph number C5, $M_{12} = 1.087$, $M_{34} = 1.109$, Mach stem length = 819 mm

The photographs, together with the triple point trajectory plots from the CFD data, were used to obtain the angles of the waves relative to the flow fields around the triple point. Three sets of data were investigated over the parameter space tested: one at a higher Mach number of the range ($M_{12} = 1.094$), one at a lower Mach number of the range ($M_{12} = 1.060$), and one midway at $M_{12} = 1.073$.

5.4.1 Sample Calculation of the Wave Interaction Angles for Photograph C6

C6: $M_{initial} = 1.277$ $M_{12} = 1.094$ Triple Point Position = (3.646; 0.850) m

From CFD results, the triple point trajectory for $M_{initial} = 1.25$ can be approximated by:

$$y = 0.0312\ x^2 + 0.1199\ x$$

So for x = 3.646 m, y = 0.852 m. A difference in the height of 0.2 %

The slope of the trajectory at this point is given by:

$$\left.\frac{dy}{dx}\right|_{x=3.646} = 2(0.0312)x + 0.1199 = 0.3474$$

The triple point trajectory angle at this point is therefore:

$$\chi = \arctan(0.3474) = 19.2°$$

From the schematic diagram of the schlieren photograph C6, the incident angles of the flow relative to the waves can be calculated:

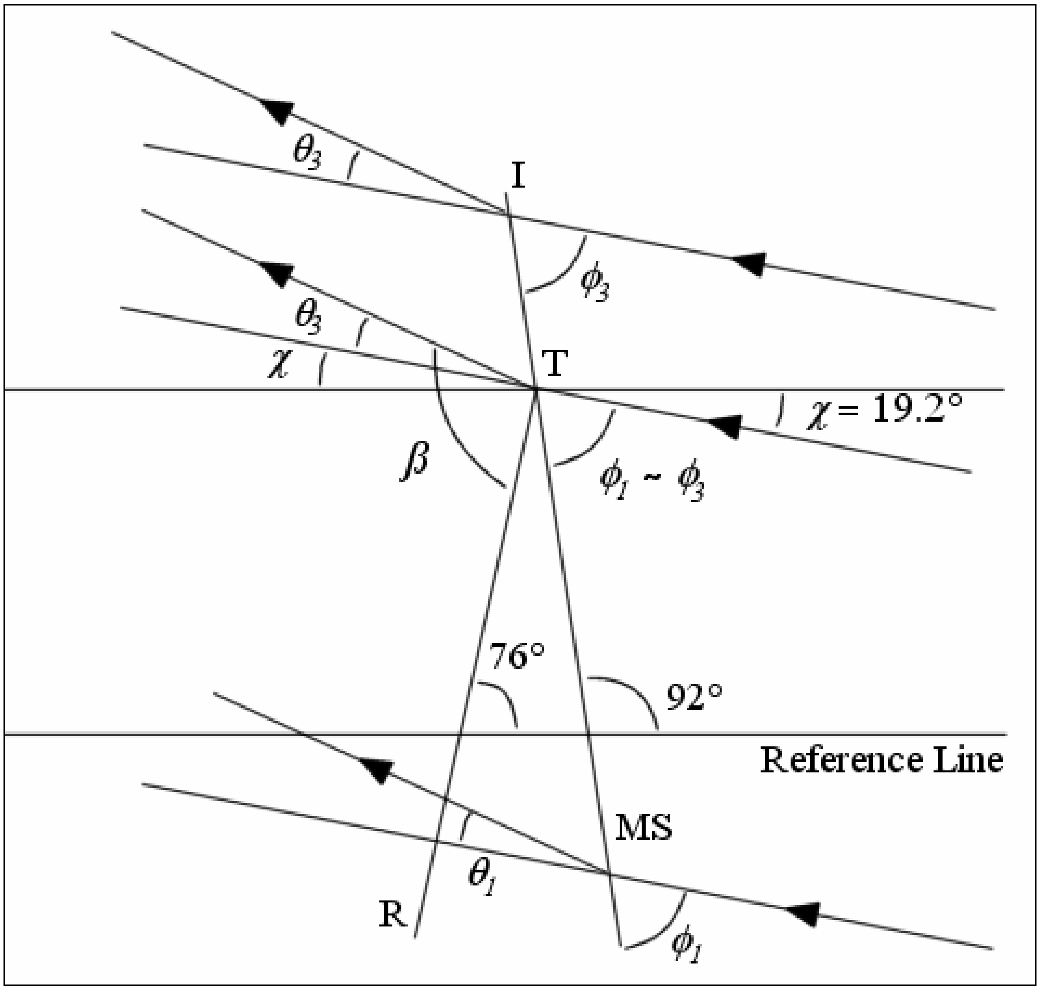

Figure 5.4.8 – Schematic diagram of wave interaction angles near the triple point.

From the photographs is it can be seen that the slopes of the incident wave and Mach stem are almost continuous near the triple point, i.e. $\phi_1 \approx \phi_3$.

$\phi_3 = 68.8°$

The angle of the flow behind the Mach stem can be calculated from the equation for the conservation of tangential momentum:

$$\rho_0 \tan \phi_3 = \rho_3 \tan(\phi_3 - \theta_3)$$

where,

$$\frac{\rho_3}{\rho_0} = \frac{6}{1 + {}^{5}\!/\!{}_{M_{12}^2}}$$

which gives,

$\theta_3 = 3°$

The angle between the flow field and the reflected wave can therefore be approximated as,

$\beta = 76° + \chi + \theta_3 = 98.2°$

which is beyond the transition point of $\beta \geq \pi/2$, where according to Colella & Henderson (1990), the three-shock theory breaks down.

6. Discussion

6.1 Discussion of Quantitative Data

The Figures 5.3.1-5.3.5 were used to determine the characteristics of the shock tube, i.e. to determine the Mach numbers of the Mach stem (M_{12} & M_{34}) and an approximation of the incident wave Mach number ($\approx M_{12}$) for given initial driver pressures (P_4) and Mach numbers ($M_{initial}$). It can be argued that the incident wave Mach number is approximately equal to the Mach number recorded at channels 1 & 2, as the triple point passes very close to this point, and the slopes of the Mach stem and the incident wave are continuous near the triple point, suggesting similar values for Mach number.

Figure 5.3.1 shows that the Mach number achievable in the test section is dependant on the initial Mach number by a squared relationship, and by increasing the initial Mach number, the Mach stem and incident wave Mach number would increase, as expected. An initial Mach number of $M_{initial} = 1.2$ would produce an incident wave Mach number of approximately $M_{12} = 1.060$, and $M_{initial} = 1.3$ would produce $M_{12} \approx 1.15$.

A similar representation is given by Figures 5.3.4 and 5.3.5, which plot the Mach number achievable in the test section with the initial driver pressure (P_4). Over such a small range, it can be seen that increasing the driver pressure increases the Mach number almost linearly. An initial pressure of $P_4 = 200$ kPa, which is the natural bursting pressure for the diaphragm used, corresponded to an incident wave Mach number of 1.09-1.12 and a Mach stem Mach number near the roof of 1.11-1.13. Higher Mach numbers were obtained by doubling the diaphragm or by using a thicker material.

From Figure 5.3.2 it can be seen that the Mach stem Mach number recorded near the triple point (M_{12}) follows an almost linear relationship with the Mach stem Mach number recorded near the roof of the test section (i.e. the base of the Mach stem). The differences in values are generally small (between 1 and 3 %), with the value recorded near the roof being higher than that near the triple point. For example, for $M_{12} = 1.07$, the value of M_{34} would be approximately 1.10, a difference of 3%.

When plotting the Mach stem Mach number near the roof of the section (M_{34}) with the initial Mach number from the driver, again an almost linear relationship can be seen, as in Figure 5.3.3. An increase in the initial Mach number would provide a smaller increase in the Mach stem Mach number.

6.2 Discussion of Results from Schlieren Photographs

The Mach stem lengths were measured by scaling the triple point position relative to the to cotton thread markers placed across the test window. Some of the earlier tests did not have the markers and hence the Mach stem lengths were estimated by using the height of the portion of the test section window visible in the photograph.

The position of the triple point was plotted for various initial driver pressures in Figure 5.4.1, for the photographs which had the cotton markers across the window. It is clear that the Mach stem length increases with increasing initial pressure in the driver, and hence initial Mach number. The displacement of the triple point along the test section from the reflection corner also naturally increases for increasing driver pressure. The triple point was visualised in the test section window for values of P_4 = 120-180 kPa and yielded Mach stem lengths of 680-850 mm. The resulting Mach stem lengths are very reproducible to within a range of 20 mm.

Figure 5.4.2 shows the triple point heights (for all the tests where the triple point was visible) plotted against the incident wave Mach number, showing the Mach stem length ranged from approximately 700 mm for M_{12} = 1.060 to around 850 mm for M_{12} = 1.094 in an almost linear dependence.

A similar graph is presented in Figure 5.4.3 which plots the Mach stem length with the initial Mach number exiting the driver section. Again the relationship is squared, but over such a small range it almost resembles a linear curve.

From the calculations done of the angle between the flow field behind the Mach stem and the reflected wave (β), it was found that over the parameter space tested, the angle was greater than $\pi/2$. For the lower Mach number (M_{12} = 1.060), β = 93°; for the mid-range value (M_{12} = 1.073), β = 93.2°; and for the higher Mach number (M_{12} = 1.094), β = 98.2 °. It can also be assumed that since the incident wave and Mach stem have an almost continuous slope near the triple point, the flow field behind the incident wave and Mach stem are very nearly parallel, which would result in a very weak reflected wave close to being a sonic wave. This can be validated by the numerical results achieved by Zakharian *et al.* (2000), where they showed that for an incident wave Mach number of 1.04 and a wedge angle of 11.46°, the reflected wave had a Mach number of only 1.003. This explains why a slipstream is not seen in any of the schlieren photographs produced.

There may, however, be a slipstream which develops further downstream of the triple point, as both the Mach stem and incident wave are perpendicular to the roof and floor at their respective reflection points.

6.3 Discussion of Structures Observed in Schlieren Photographs

As was established in Chapter 2 - Introduction, the supersonic region behind the triple point was given as a percentage of the Mach stem length, and hence a larger Mach stem would produce a larger region to visualize with the optical system.

From all the forty-plus schlieren photographs, with incident wave Mach numbers (M_{12}) ranging from 1.062-1.090, an expansion fan can clearly be seen in the region behind the triple point. It is not surprising that this expansion fan had not been detected in earlier experiments, as the region in which it occurs is extremely small compared to the length of the Mach stem. These experimental results compare very well to the numerical results obtained by Vasil'ev & Kraiko (1999) and Zakharian *et al.* (2000) and prove that Guderley's (1947) proposal of a supersonic region behind the triple point was in fact correct. It can be deduced that a four-wave geometry with an expansion fan behind the triple point is a real phenomenon for weak shock wave reflections which occur over the parameter space covered in these tests.

The expansion fan can be seen in Figures 5.4.5-5.4.7, which are random examples of the unprocessed photographs of the test section window, as well as the following Figures 6.1-6.13 which are rotated 90° clockwise and mirrored relative to the test section.

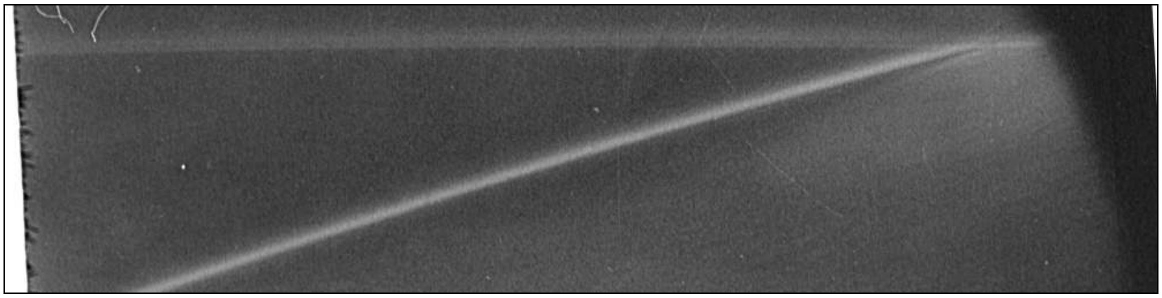

Figure 6.1 – Photograph number A16, $M_{12} = 1.063$, $M_{34} = 1.094$, Mach stem length = 727 mm

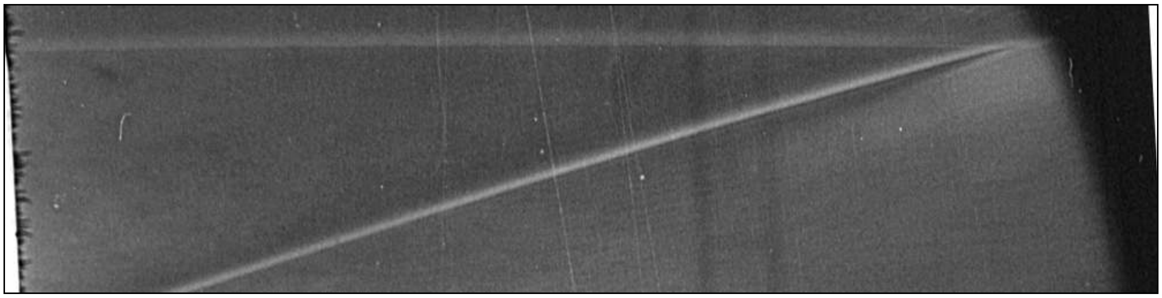

Figure 6.2 – Photograph number A20, $M_{12} = 1.063$, $M_{34} = 1.095$, Mach stem length = 722 mm

In the above two figures a distinct, lighter, contrasting line can be seen immediately behind the expansion region, indicating the existence of a terminating shock. The suggestion by Hunter & Brio (2000) that a shock may terminate the expansion wave, as occurs on a transonic airfoil, seems to prove true. This shock is referred to as the first shocklet, and was estimated to be 15 mm in length, or roughly 2% of the Mach stem length. A fairly strong density gradient can be seen behind the shocklet, which weakens along the length of the Mach stem, but no more evidence of other features can be clearly distinguished.

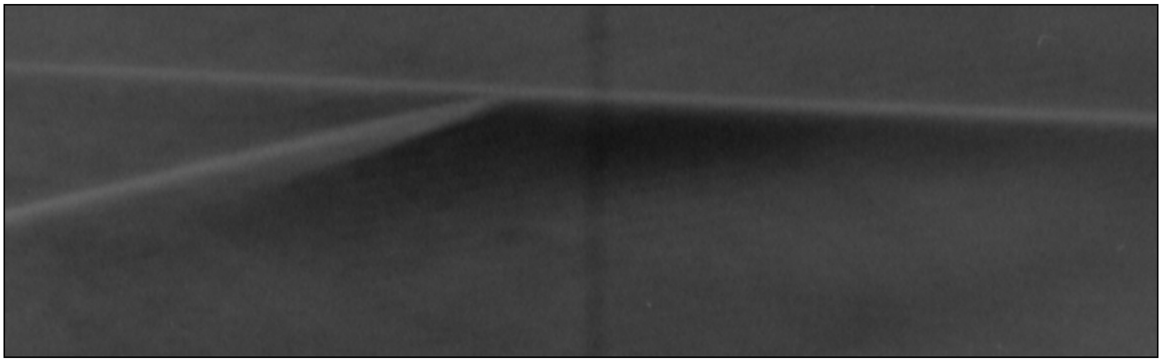

Figure 6.3 – Photograph number C18, $M_{12} = 1.078$, $M_{34} = 1.103$, Mach stem length = 774 mm

Figure 6.3 clearly shows the density gradient (dark patch) existing from behind the expansion wave up to behind and along the Mach stem. This density gradient can be seen on all the forty-plus photographs taken.

The immediate region behind the triple point was enlarged and the image contrast was adjusted in order to highlight any additional structures behind the first shocklet. The image enhancements were made by using Corel Photo-Paint © and Jasc Paint Shop Pro©. Examples of the original scan and the processed images are given below.

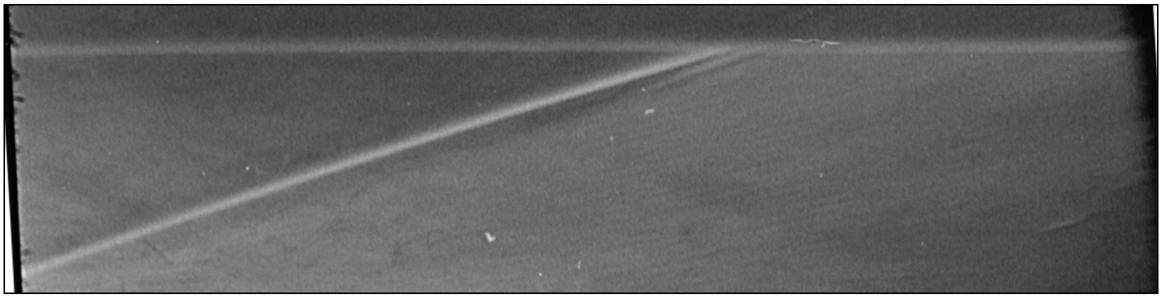

Figure 6.4 – Photograph A08, M12 = 1.073, M34 = 1.093, Mach stem length = 766 mm

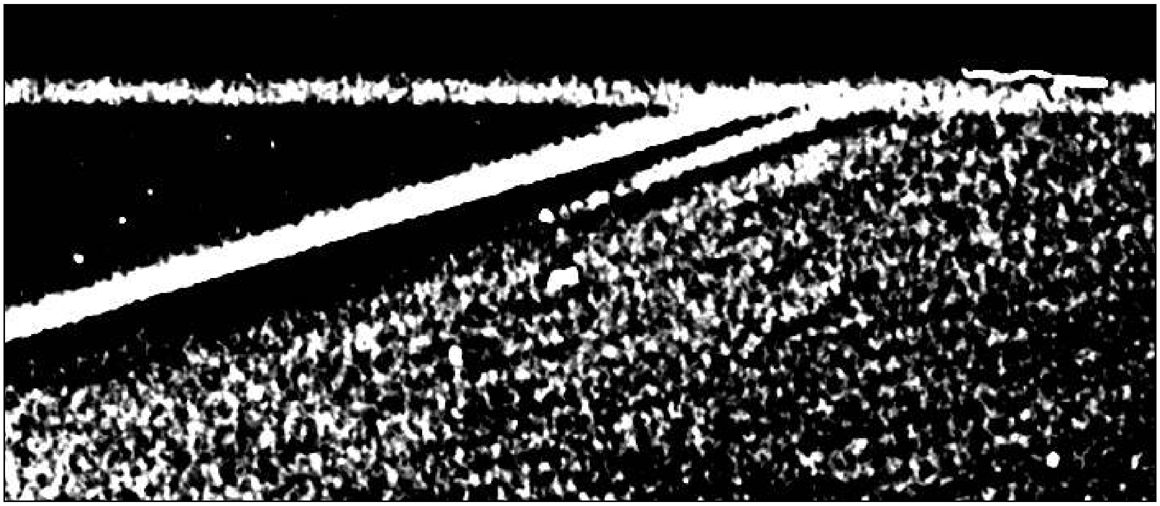

Figure 6.5 – Photograph A08 with adjusted contrast

From Figure 6.5, the first expansion region is clearly defined as the dark region immediately behind the reflected wave, centered on the triple point. In this image, the first shocklet is clearly visible as a bright line behind the reflected wave and first expansion fan. A second expansion fan can be seen immediately behind the first shocklet, and is followed by a lighter area. This implies that a second shocklet should therefore terminate the second expansion fan, a third shocklet terminate the third expansion fan and so on, as shown by Hunter & Tesdall (2002). Any features behind the second expansion fan seem to be smoothed out in the density gradient behind the Mach stem (the larger light area behind the second expansion fan). The leading triple point is also very distinct as there is no band of compression waves from the reflected wave behind the triple point, as described by Colella & Henderson (1990), and hence by definition, this reflection is not a von Neumann reflection.

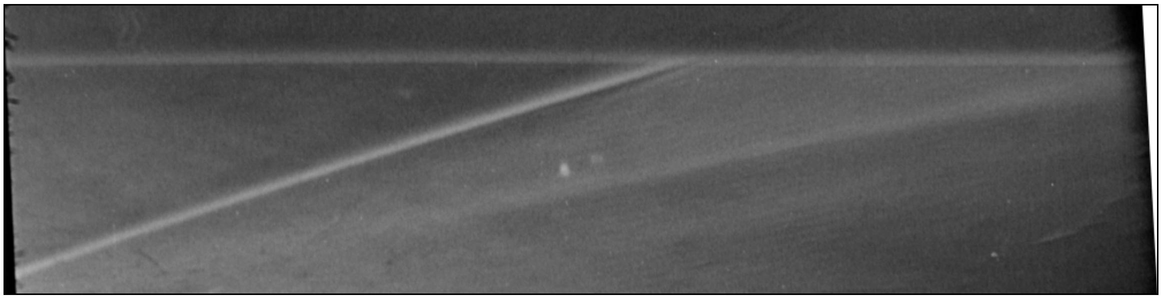

Figure 6.6 – Photograph number A07, M12 = 1.074, M34 = 1.099, Mach stem length = 772 mm

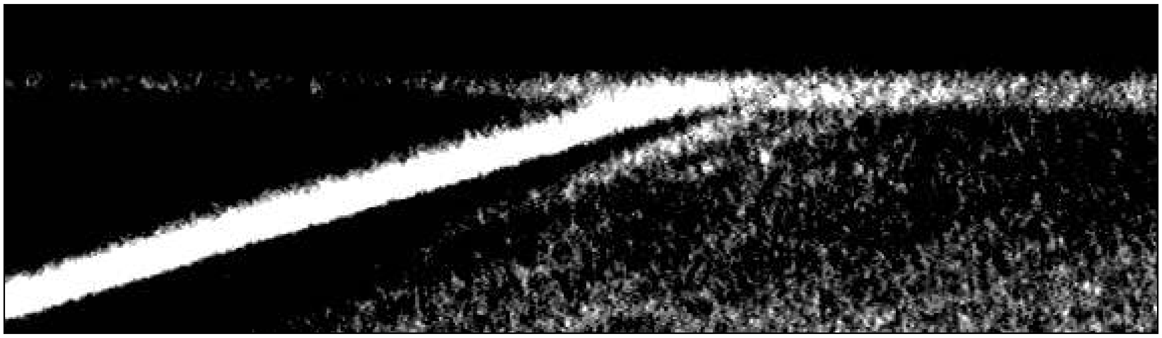

Figure 6.7 – Photograph A07 with adjusted contrast

Figure 6.7 again clearly shows the first shocklet behind the first expansion fan, but also shows clear evidence of the second shocklet behind the second expansion fan, as the lighter region behind the light region of the first shocklet. This implies that the flow structure behind the triple point may then include an infinite sequence of expansion fans, shocklets and triple points of decreasing size, as proposed by Hunter & Tesdall (2002). The subsequent shocklets and expansion fans are not distinguishable either due to viscous effects, knife-edge cutoff or a combination of these and other effects.

The first shocklet can also be seen in the following examples of magnified images with enhanced contrast, as well as some evidence of a second shocklet. All the adjusted images are included in the Appendix F – Schlieren Photographs.

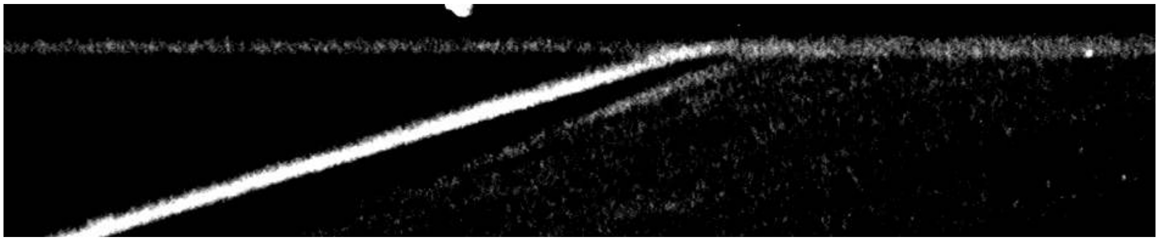

Figure 6.8 – Photograph number A11, M12 = 1.073, M34 = 1.097, Mach stem length = 766 mm

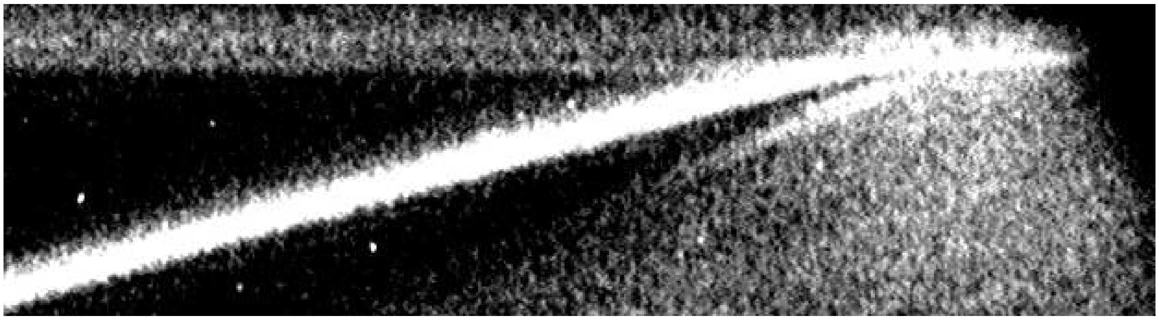

Figure 6.9 – Photograph number A15, M12 = 1.063, M34 = 1.094, Mach stem length = 727 mm

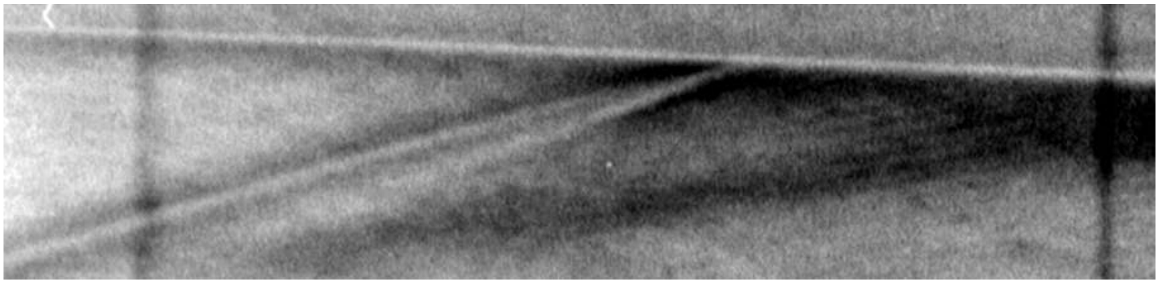

Figure 6.10 – Photograph number C15, M12 = 1.082, M34 = 1.105, Mach stem length = 797 mm

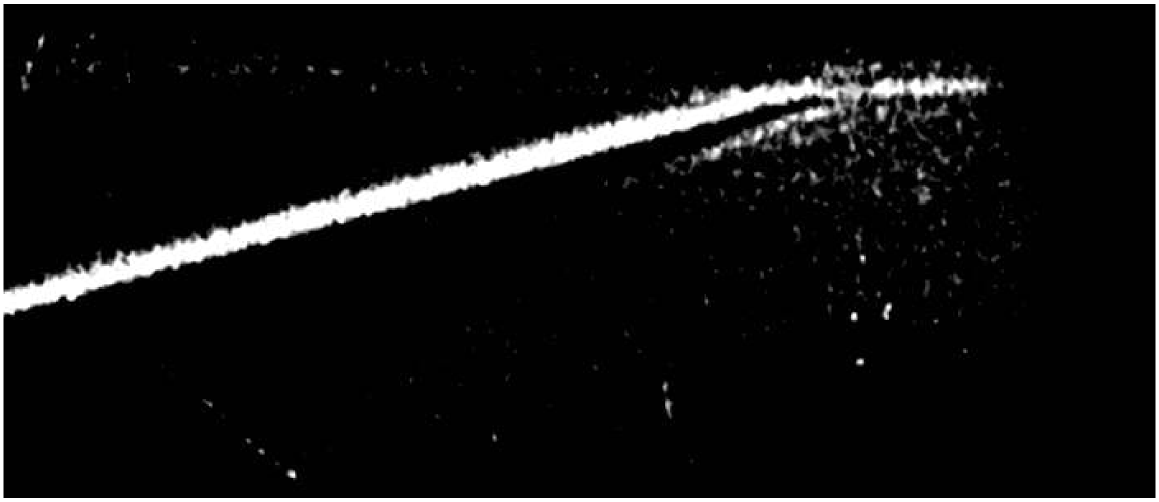

Figure 6.11 - Photograph number A16, M12 = 1.063, M34 = 1.094, Mach stem length = 727 mm

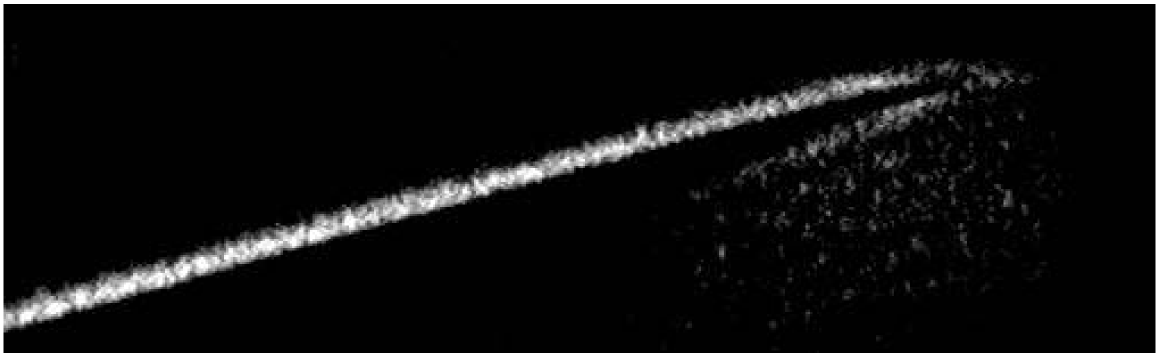

Figure 6.12 – Photograph number A20, M12 = 1.063, M34 = 1.095, Mach stem length = 722 mm

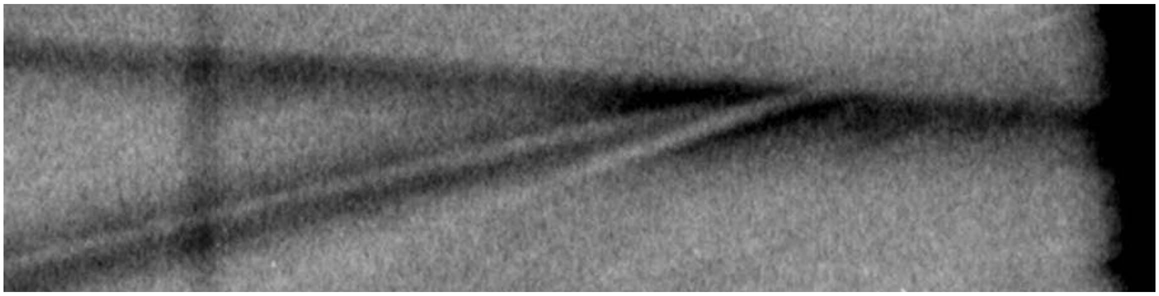

Figure 6.13 – Photograph number B33, M12 = 1.063, M34 = 1.094, Mach stem length = 728 mm

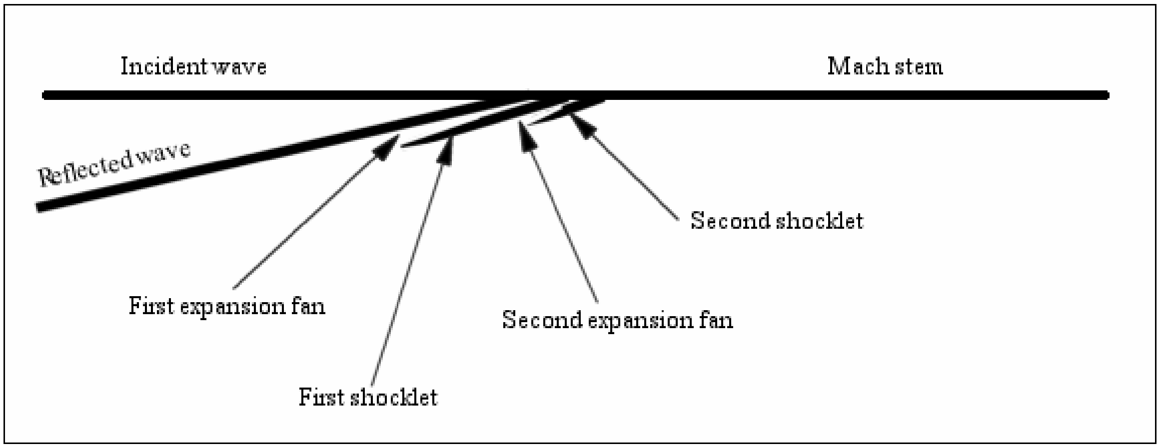

Figure 6.14 – Schematic representation of the observed wave structure behind the triple point

The diagram above gives an indication of the flow structure that can be distinguished from the photographs of the region behind the triple point. Not all of the photographs clearly showed the existence of a second shocklet or even a second expansion fan, and these effects seem to be variable due to the varying sensitivity of the optical system and other factors.

It is important to note that all the numerical studies yielding a complex flow structure, have been inviscid models. Zakharian *et al.* (2000) estimated that for a Mach stem length of 1 m (similar to this investigation) the patch would be an order of magnitude larger than the reflected shock thickness. It is not known, however, whether the small high density gradients in the complex flow structure would be smoothed out due to viscous effects.

The slipstream was not distinct in any of the photographs obtained, and hence the angle between the reflected wave and the slipstream (β) could not be measured directly from the photographs.

Although a von Neumann reflection was not observed, it is not certain whether such complex structure such as observed here is prevalent in other parameter spaces, or whether a von Neumann reflection occurs at other parameter spaces. It is clear that this type of reflection is different from the von Neumann reflection in that no band of compression waves were observed, and it may be appropriate to name this reflection, where a supersonic patch exists, as Guderley reflection in recognition of his prediction over fifty years ago.

The four-wave geometry has been shown to exist for plane incident waves from numerical results as well as experimentally in this work for cylindrical shock waves, and is therefore likely to be a common occurrence. It is likely that this geometry exists for spherical blast waves as well.

The results resolve the so-called “von Neumann Paradox” by showing that experimentally, the leading triple point is distinct, the region behind the triple point has an expansion/compression structure as described by Hunter & Brio (2000) and in some cases, multiple expansion/compression structures as described by Hunter & Tesdall (2002).

7. Conclusions

For the parameter space tested, a supersonic region clearly exists behind the triple point of a weak shock reflection, as originally proposed by Guderley (1947). The reason why this region had not been observed experimentally earlier is due to the very small size relative to the Mach stem length (roughly 2% of the Mach stem). The experimental results are consistent with recent findings of numerical studies of weak shock reflections.

An expansion fan can be seen emanating from the triple point, similar to the numerical results by Vasil'ev & Kraiko (1999) and Zakharian *et al.* (2000), in all forty-plus tests presented here. It is therefore apparent that a four-wave weak shock reflection is indeed a real physical phenomenon. A shocklet terminating the expansion fan can be seen in most of the tests, similar to the flow structure as described by Hunter & Brio (2000). In the cases where a shocklet can be seen, a second expansion fan be clearly observed behind the first shocklet. In some cases a second shocklet was observed terminating the second expansion fan. It is suggested that subsequent shocklets and expansion fans may be smoothed by viscous effects in the supersonic region. The high-resolution experiments of the reflection of weak shock waves have shown the existence of a very small complex flow structure similar to a sequence of expansion fans, shocklets, and triple points behind the leading triple point as described by Hunter & Tesdall (2002).

A von Neumann reflection as defined by Colella & Henderson (1990), consisting of a band of compression waves near the triple point, could not be reproduced experimentally. Instead, a new type of four-wave weak shock reflection was observed, as described by Tesdall & Hunter (2002). It has been proposed that such a reflection be termed a 'Guderley reflection'.

The results of this investigation finally resolve the von Neumann Paradox, by experimentally validating the numerical studies of Hunter & Tesdall (2002) and similar recent studies, as well as establishing the existence of an expansion fan behind the reflected shock, as proposed by Guderley (1947).

8. Recommendations

It is suggested that the parameter space should be expanded to cover a larger range of incident wave Mach numbers, perhaps up to the maximum allowable test section Mach number of 1.25. The wall angle of the test section should also be changed by attaching a ramp to the roof of the divergent section, thereby decreasing the wedge angle, although this will require a major modification to the current setup.

Some tests should be conducted in order to reproduce the results obtained by Colella & Henderson (1990) to observe the flow structure and hence determine the experimental existence of a von Neumann reflection.

The installation of additional pressure transducers in the test section to determine the incident wave Mach number, the decay of the incident wave Mach number, and the Mach number of the expanding cylindrical wave in the vicinity of the reflection corner would be very useful to improve the quantitative data.

It would be advantageous to have ultra-high resolution numerical analysis of the current shock tube geometry in order to determine the optimum range of experimental conditions as well as improve the resolution of the size of the supersonic patch and the strength of the waves in the system.

A high-resolution numerical study of the weak shock reflection using viscous codes should be investigated to determine the effects of viscosity on the flow structure in the supersonic patch.

The modification of the current schlieren optical system to increase sensitivity as well as magnifying the image may prove useful in resolving any additional features in the supersonic patch.

9. References

Ben-Dor, G., (1992) *Shock Wave Reflection Phenomena*, Springer-Verlag, New York.

Ben-Dor, G., Igra, O. & Elperin, T. *Handbook of Shockwaves – Volume 2, 'Shock Wave Interactions and Propagation'*

Birkhoff, G. (1950) *Hydrodynamic, a study in logic, fact and similitude.* Dover.

Brio, M. & Hunter, J. (1992) Mach reflection for the two-dimensional Burgers equation. *Physic D* **60**, 194-207.

Čanić, S. & Keyfitz, B. (1995) Oblique shock interactions and the von Neumann paradox. In *20th Int. Symp. on Shock Waves* (ed. B. Sturtevant, J. Shepherd & H. Hornung), pp. 435-440. World Scientific, 1996.

Chuse, R., (1960) *Unfired Pressure Vessels – The ASME Code Simplified* (4th Edition), F.W. Dodge Corporation, New York, 1960, pp. 57.

Colella, P. & Henderson, L. (1990) The von Neumann paradox for the diffraction of weak shock waves. *J. Fluid Mech.* **213**, 71-94.

Guderley, K. (1947) Considerations on the structure of mixed subsonic-supersonic flow patterns. *Tech.Rep.* F-TR-2168-ND. Wright Field, See also Guderley, K.G. 1962 *The Theory of Transonic Flow*, Pergamon Press, pp 144-149.

Hunter, J.K. & Brio, M. (2000) Weak shock reflection. *J. Fluid Mech.* **410**, 235-261.

Hunter, J.K. & Tesdall, A.M. (2002) Transonic solutions for the Mach reflection of weak shocks. *Proceedings of Symposium Transsonicum IV, Gottingen.*

von Neumann, J. (1943) Oblique reflection of shocks. *Tech. Rep.* 12. Bur. Ord. Explosives Research Rept.

Olim, M. & Dewey, J. (1992) A revised three-shock solution for the Mach reflection of weak shocks. *Shock Waves* **2**, 167-176.

Sakurai, A. & Takayama, F. (2004) Analytical solution of flow field for weak Mach reflection over plane surface. In *24th Int. Symp. on Shock Waves* (ed. Z. Jiang). Springer.

Sandeman, R. (1997) Conditions at the triple point in weak Mach reflection. In *21st Int. Symp. on Shock Waves* (ed. A. Houwing & A. Paull). Panther Publishing.

Sandeman, R. (2000) A simple physical theory of weak Mach reflection over plane surfaces. *Shock Waves* **10**, 103-112.

Sasoh, A., Takayama, K. & Saito, T. (1992) An experimental and numerical study on von Neumann Mach reflection. In *Shock Waves @ Marseille III, 19th Int. Symp. on Shock Waves* (ed. R. Brun & L. Dumitrescu), pp. 11-20. Springer-Verlag, 1995.

Tesdall, A.M. & Hunter, J.K. (2002) Self-similar solutions for weak shock reflection. *Siam. J. Appl. Math.* **63**, pp. 42-61.

Vasil'ev, E. & Kraiko, A. (1999) Numerical solution of weak shock diffraction over a wedge under the von Neumann paradox conditions. *Computational Mathematics and Mathematical Physics* **39**, pp. 1335-1345.

Zakharian, A., Brio, M., Hunter, J. & Webb, G. (2000) The von Neumann paradox in weak shock reflection. *J. Fluid Mech.* **422**, pp. 193-205.

ASME Boiler and Pressure Vessel Code, Section VIII, Division 2 (1968 Edition), The American Society of Mechanical Engineers, pp. 1-3.

Appendix A – CFD Results

Overall results from Initial CFD simulations to optimise shock tube geometry

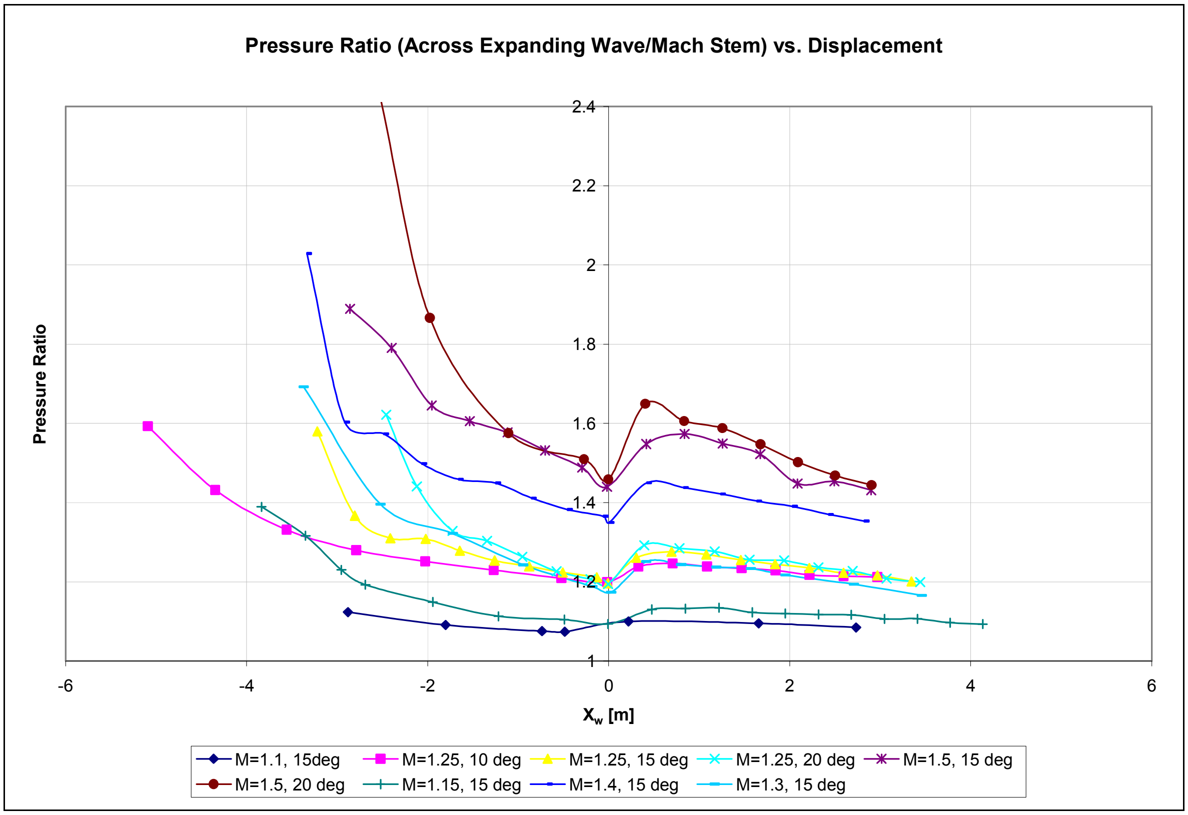

Figure A 1 – Pressure ratio across expanding wave up to reflection corner ($X_w < 0$) and across Mach stem ($X_w > 0$), plotted against displacement.

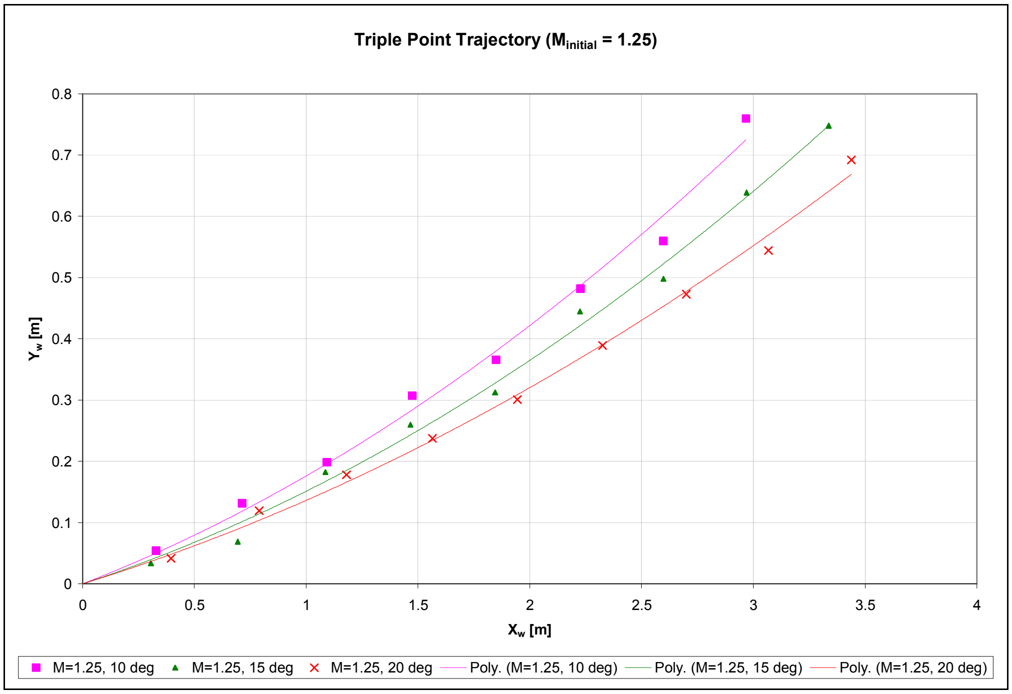

Figure A 2 – Triple Point Trajectory for $M_{initial}$ = 1.25 for various wedge angles

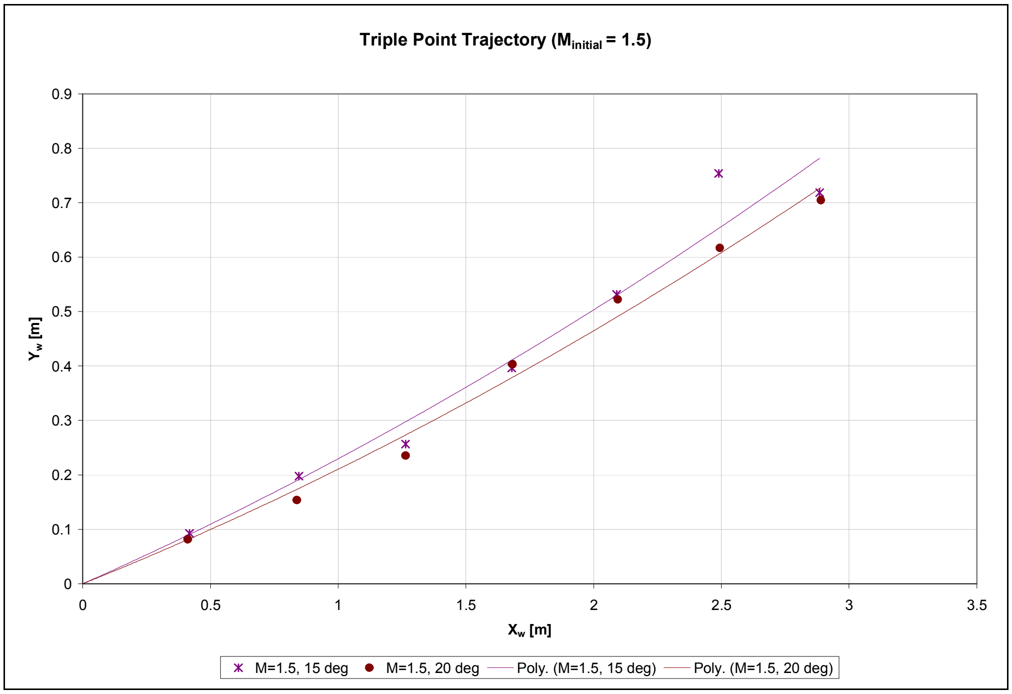

Figure A 3 – Triple Point Trajectory for $M_{initial}$ = 1.5 for various wedge angles

Example Data Set for $M_{initial} = 1.25$, $\theta_w = 15°$

Table A 1 – Data extracted from CFD

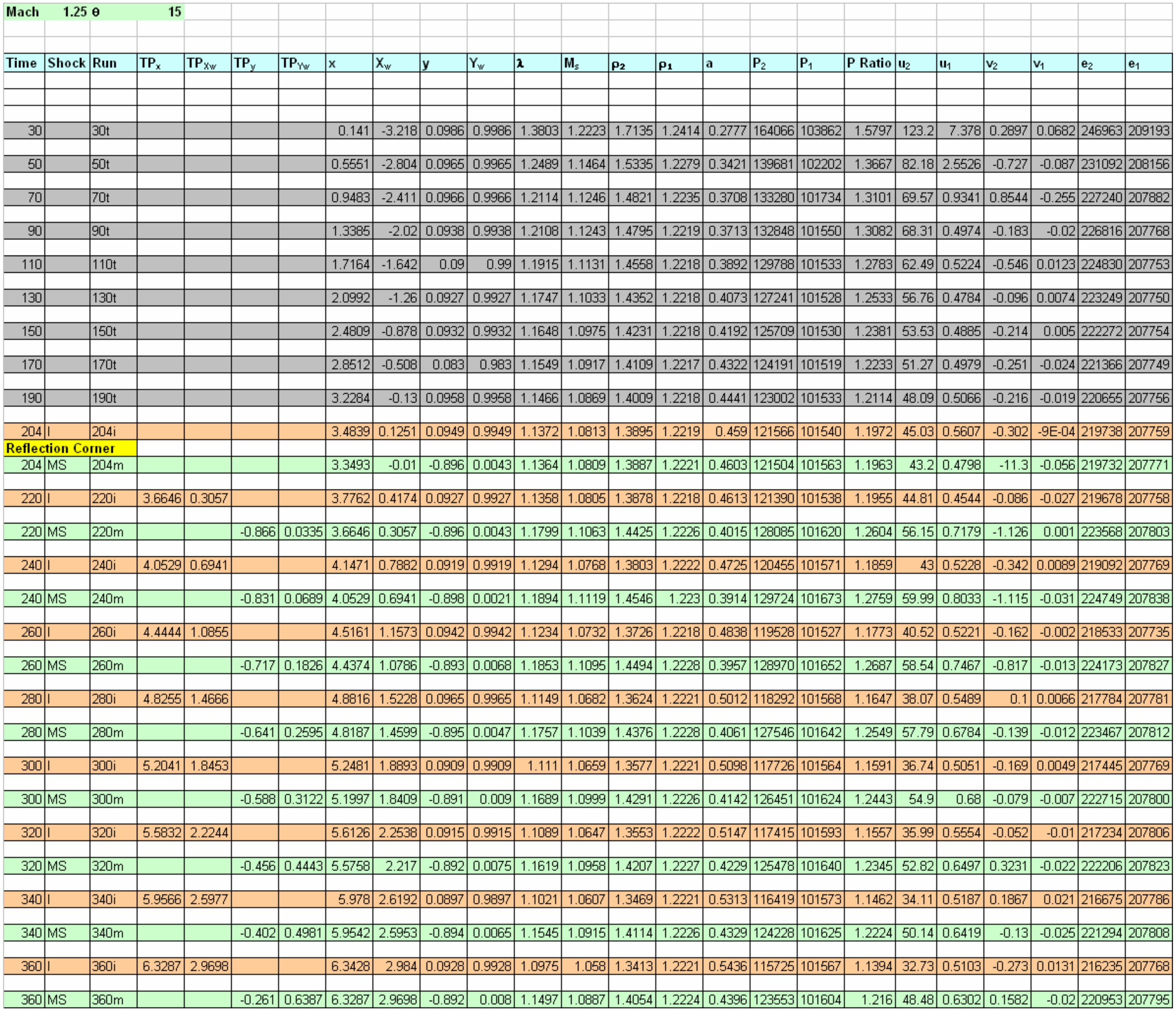

Mach 1.25 θ 15

Time	Shock	Run	TP_x	TP_{Xw}	TP_y	TP_{Yw}	x	X_w	y	Y_w	λ	M_s	ρ_2	ρ_1	a	P_2	P_1	P Ratio	u_2	u_1	v_2	v_1	e_2	e_1
30		30t					0.141	-3.218	0.0986	0.9986	1.3803	1.2223	1.7135	1.2414	0.2777	164066	103862	1.5797	123.2	7.378	0.2897	0.0682	246963	209193
50		50t					0.5551	-2.804	0.0965	0.9965	1.2489	1.1464	1.5335	1.2279	0.3421	139681	102202	1.3667	82.18	2.5526	-0.727	-0.087	231092	208156
70		70t					0.9483	-2.411	0.0966	0.9966	1.2114	1.1246	1.4821	1.2235	0.3708	133280	101734	1.3101	69.57	0.9341	0.8544	-0.255	227240	207882
90		90t					1.3385	-2.02	0.0938	0.9938	1.2108	1.1243	1.4795	1.2219	0.3713	132848	101550	1.3082	68.31	0.4974	-0.183	-0.02	226816	207768
110		110t					1.7164	-1.642	0.09	0.99	1.1915	1.1131	1.4558	1.2218	0.3892	129788	101533	1.2783	62.49	0.5224	-0.546	0.0123	224830	207753
130		130t					2.0992	-1.26	0.0927	0.9927	1.1747	1.1033	1.4352	1.2218	0.4073	127241	101528	1.2533	56.76	0.4784	-0.096	0.0074	223249	207750
150		150t					2.4809	-0.878	0.0932	0.9932	1.1648	1.0975	1.4231	1.2218	0.4192	125709	101530	1.2381	53.53	0.4885	-0.214	0.005	222272	207754
170		170t					2.8512	-0.508	0.083	0.983	1.1549	1.0917	1.4109	1.2217	0.4322	124191	101519	1.2233	51.27	0.4979	-0.251	-0.024	221366	207749
190		190t					3.2284	-0.13	0.0958	0.9958	1.1466	1.0869	1.4009	1.2218	0.4441	123002	101533	1.2114	48.09	0.5066	-0.216	-0.019	220655	207756
204	I	204i					3.4839	0.1251	0.0949	0.9949	1.1372	1.0813	1.3895	1.2219	0.459	121566	101540	1.1972	45.03	0.5607	-0.302	-9E-04	219738	207759
Reflection Corner																								
204	MS	204m					3.3493	-0.01	-0.896	0.0043	1.1364	1.0809	1.3887	1.2221	0.4603	121504	101563	1.1963	43.2	0.4798	-11.3	-0.056	219732	207771
220	I	220i	3.6646	0.3057			3.7762	0.4174	0.0927	0.9927	1.1358	1.0805	1.3878	1.2218	0.4613	121390	101538	1.1955	44.81	0.4544	-0.086	-0.027	219678	207758
220	MS	220m			-0.866	0.0335	3.6646	0.3057	-0.896	0.0043	1.1799	1.1063	1.4425	1.2226	0.4015	128085	101620	1.2604	56.15	0.7179	-1.126	0.001	223568	207803
240	I	240i	4.0529	0.6941			4.1471	0.7882	0.0919	0.9919	1.1294	1.0768	1.3803	1.2222	0.4725	120455	101571	1.1859	43	0.5228	-0.342	0.0089	219092	207769
240	MS	240m			-0.831	0.0689	4.0529	0.6941	-0.898	0.0021	1.1894	1.1119	1.4546	1.223	0.3914	129724	101673	1.2759	59.99	0.8033	-1.115	-0.031	224749	207838
260	I	260i	4.4444	1.0855			4.5161	1.1573	0.0942	0.9942	1.1234	1.0732	1.3726	1.2218	0.4838	119528	101527	1.1773	40.52	0.5221	-0.162	-0.002	218533	207735
260	MS	260m			-0.717	0.1826	4.4374	1.0786	-0.893	0.0068	1.1853	1.1095	1.4494	1.2228	0.3957	128970	101652	1.2687	58.54	0.7467	-0.817	-0.013	224173	207827
280	I	280i	4.8255	1.4666			4.8816	1.5228	0.0965	0.9965	1.1149	1.0682	1.3624	1.2221	0.5012	118292	101568	1.1647	38.07	0.5489	0.1	0.0066	217784	207781
280	MS	280m			-0.641	0.2595	4.8187	1.4599	-0.895	0.0047	1.1757	1.1039	1.4376	1.2228	0.4061	127546	101642	1.2549	57.79	0.6784	-0.139	-0.012	223467	207812
300	I	300i	5.2041	1.8453			5.2481	1.8893	0.0909	0.9909	1.111	1.0659	1.3577	1.2221	0.5098	117726	101564	1.1591	36.74	0.5051	-0.169	0.0049	217445	207769
300	MS	300m			-0.588	0.3122	5.1997	1.8409	-0.891	0.009	1.1689	1.0999	1.4291	1.2226	0.4142	126451	101624	1.2443	54.9	0.68	-0.079	-0.007	222715	207800
320	I	320i	5.5832	2.2244			5.6126	2.2538	0.0915	0.9915	1.1089	1.0647	1.3553	1.2222	0.5147	117415	101593	1.1557	35.99	0.5554	-0.052	-0.01	217234	207806
320	MS	320m			-0.456	0.4443	5.5758	2.217	-0.892	0.0075	1.1619	1.0958	1.4207	1.2227	0.4229	125478	101640	1.2345	52.82	0.6497	0.3231	-0.022	222206	207823
340	I	340i	5.9566	2.5977			5.978	2.6192	0.0897	0.9897	1.1021	1.0607	1.3469	1.2221	0.5313	116419	101573	1.1462	34.11	0.5187	0.1867	0.021	216675	207786
340	MS	340m			-0.402	0.4981	5.9542	2.5953	-0.894	0.0065	1.1545	1.0915	1.4114	1.2226	0.4329	124228	101625	1.2224	50.14	0.6419	-0.13	-0.025	221294	207808
360	I	360i	6.3287	2.9698			6.3428	2.984	0.0928	0.9928	1.0975	1.058	1.3413	1.2221	0.5436	115725	101567	1.1394	32.73	0.5103	-0.273	0.0131	216235	207768
360	MS	360m			-0.261	0.6387	6.3287	2.9698	-0.892	0.008	1.1497	1.0887	1.4054	1.2224	0.4396	123553	101604	1.216	48.48	0.6302	0.1582	-0.02	220953	207795

380	I	380i	6.6959	3.337			6.7094	3.3505	0.0941	0.9941	1.0944	1.0562	1.3375	1.2221	0.5523	115252	101575	1.1346	31.72	0.456	-0.033	-3E-04	215932	207794
380	MS	380m			-0.152	0.7477	6.7049	3.346	-0.891	0.0086	1.1397	1.0828	1.393	1.2223	0.4549	121996	101587	1.2009	45.68	0.4847	-0.302	-0.022	219986	207780

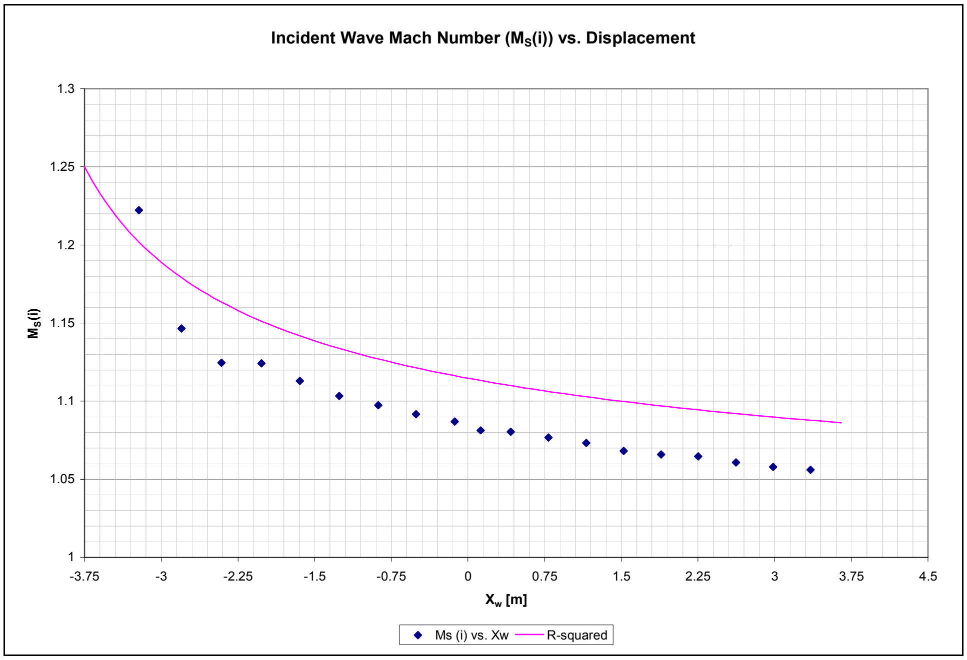

Figure A 4 - Incident wave Mach number from CFD results plotted with $1/R^2$ decay rate versus displacement.

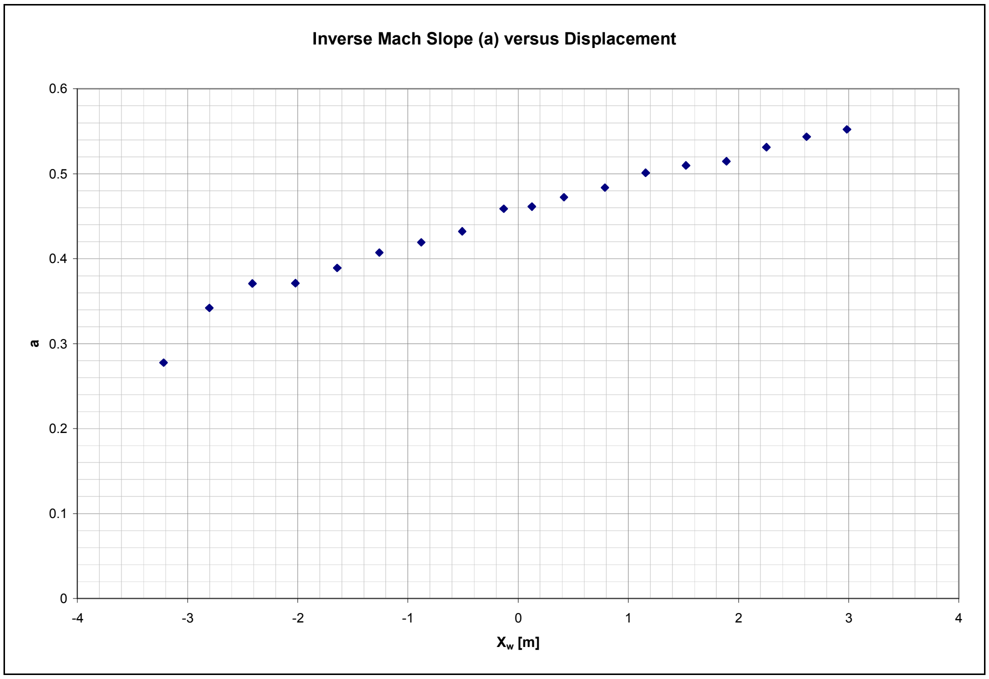

Figure A 5 – Inverse Mach slope versus displacement from the reflection corner

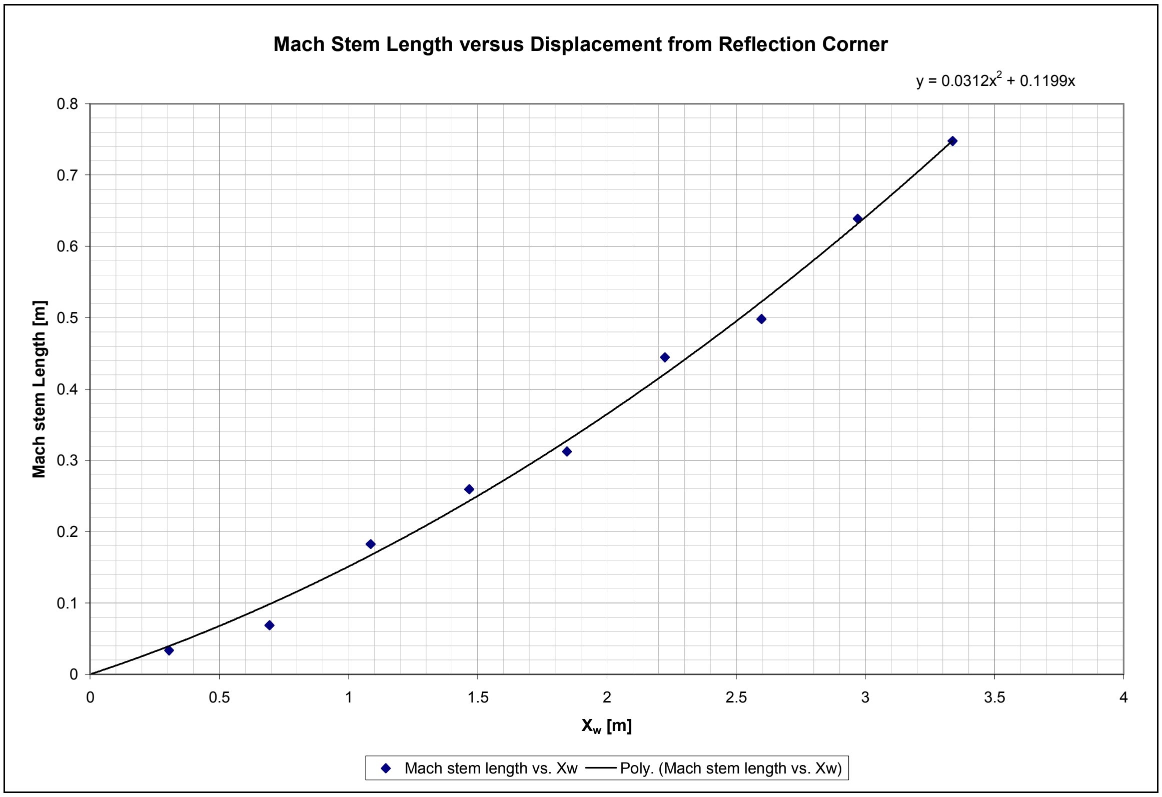

Figure A 6 – Mach stem length versus displacement from reflection corner

Example Data Set from Final CFD Results for $M_{initial} = 1.2$

Table A 2 – Data extracted Pre-reflection

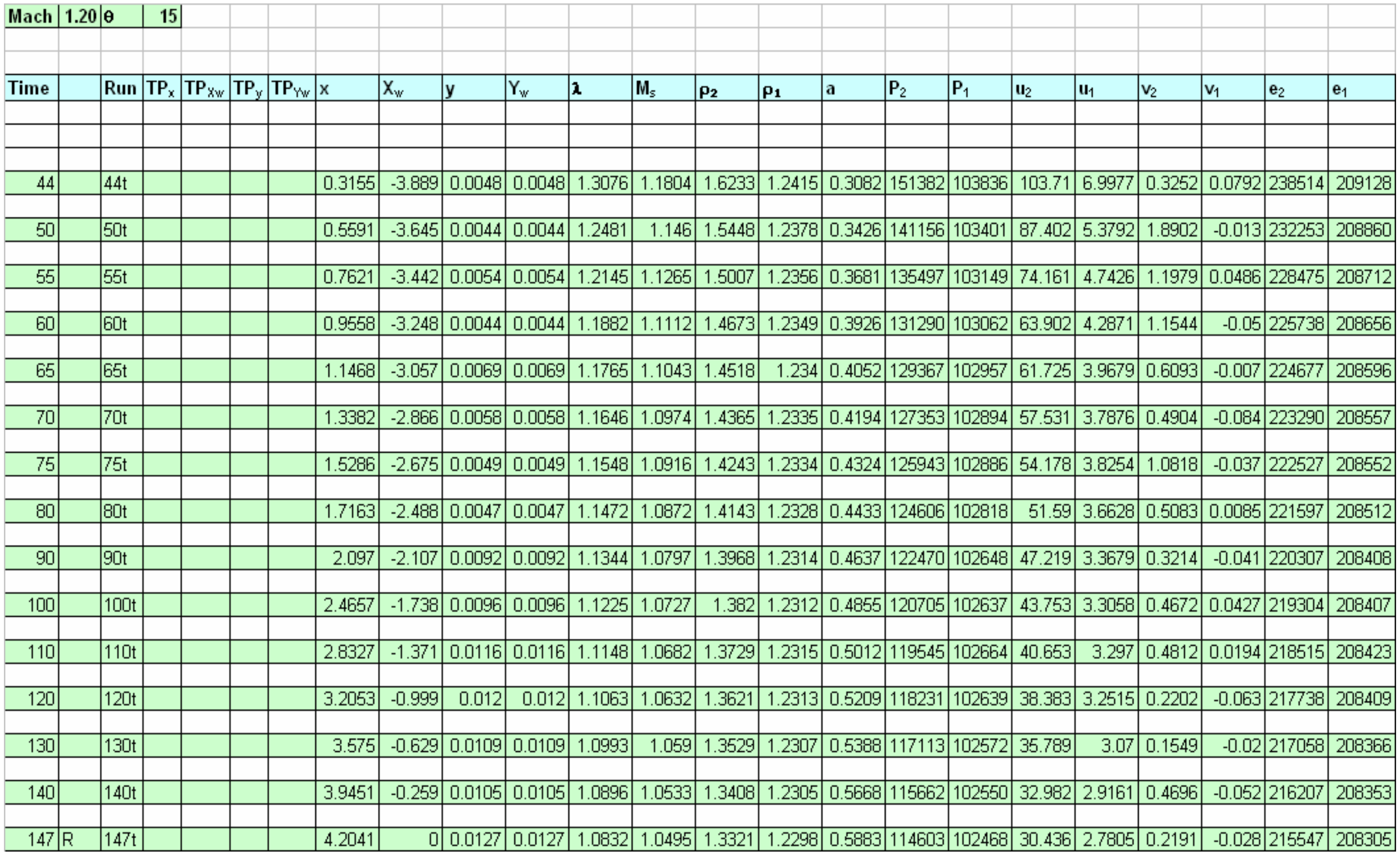

Mach	1.20	θ	15

Time		Run	TP_x	TP_{Xw}	TP_y	TP_{Yw}	x	X_w	y	Y_w	λ	M_s	ρ_2	ρ_1	a	P_2	P_1	u_2	u_1	v_2	v_1	e_2	e_1
44		44t					0.3155	-3.889	0.0048	0.0048	1.3076	1.1804	1.6233	1.2415	0.3082	151382	103836	103.71	6.9977	0.3252	0.0792	238514	209128
50		50t					0.5591	-3.645	0.0044	0.0044	1.2481	1.146	1.5448	1.2378	0.3426	141156	103401	87.402	5.3792	1.8902	-0.013	232253	208860
55		55t					0.7621	-3.442	0.0054	0.0054	1.2145	1.1265	1.5007	1.2356	0.3681	135497	103149	74.161	4.7426	1.1979	0.0486	228475	208712
60		60t					0.9558	-3.248	0.0044	0.0044	1.1882	1.1112	1.4673	1.2349	0.3926	131290	103062	63.902	4.2871	1.1544	-0.05	225738	208656
65		65t					1.1468	-3.057	0.0069	0.0069	1.1765	1.1043	1.4518	1.234	0.4052	129367	102957	61.725	3.9679	0.6093	-0.007	224677	208596
70		70t					1.3382	-2.866	0.0058	0.0058	1.1646	1.0974	1.4365	1.2335	0.4194	127353	102894	57.531	3.7876	0.4904	-0.084	223290	208557
75		75t					1.5286	-2.675	0.0049	0.0049	1.1548	1.0916	1.4243	1.2334	0.4324	125943	102886	54.178	3.8254	1.0818	-0.037	222527	208552
80		80t					1.7163	-2.488	0.0047	0.0047	1.1472	1.0872	1.4143	1.2328	0.4433	124606	102818	51.59	3.6628	0.5083	0.0085	221597	208512
90		90t					2.097	-2.107	0.0092	0.0092	1.1344	1.0797	1.3968	1.2314	0.4637	122470	102648	47.219	3.3679	0.3214	-0.041	220307	208408
100		100t					2.4657	-1.738	0.0096	0.0096	1.1225	1.0727	1.382	1.2312	0.4855	120705	102637	43.753	3.3058	0.4672	0.0427	219304	208407
110		110t					2.8327	-1.371	0.0116	0.0116	1.1148	1.0682	1.3729	1.2315	0.5012	119545	102664	40.653	3.297	0.4812	0.0194	218515	208423
120		120t					3.2053	-0.999	0.012	0.012	1.1063	1.0632	1.3621	1.2313	0.5209	118231	102639	38.383	3.2515	0.2202	-0.063	217738	208409
130		130t					3.575	-0.629	0.0109	0.0109	1.0993	1.059	1.3529	1.2307	0.5388	117113	102572	35.789	3.07	0.1549	-0.02	217058	208366
140		140t					3.9451	-0.259	0.0105	0.0105	1.0896	1.0533	1.3408	1.2305	0.5668	115662	102550	32.982	2.9161	0.4696	-0.052	216207	208353
147	R	147t					4.2041	0	0.0127	0.0127	1.0832	1.0495	1.3321	1.2298	0.5883	114603	102468	30.436	2.7805	0.2191	-0.028	215547	208305

Table A 3 – Triple point position estimated from CFD results

Triple Point Position

Run	Time	TP_x	TP_{Xw}		TP_y	TP_{Yw}
147	0	4.0573	0.00659		1.09796	0.00704
155	8	4.36074	0.31003		1.06657	0.03843
160	13	4.5526	0.50189		1.02307	0.08193
165	18	4.74557	0.69486		1.00267	0.10233
170	23	4.93569	0.88498		0.948982	0.156018
175	28	5.12255	1.07184		0.933276	0.171724
180	33	5.31547	1.26476		0.844171	0.260829
185	38	5.51921	1.4685		0.84115	0.26385
190	43	5.70855	1.65784		0.80596	0.29904
195	48	5.89442	1.84371		0.779728	0.325272
200	53	6.07934	2.02863		0.746032	0.358968
205	58	6.26423	2.21352		0.691039	0.413961
210	63	6.45279	2.40208		0.649229	0.455771
215	68	6.63154	2.58083		0.619113	0.485887
220	73	6.81772	2.76701		0.564318	0.540682
225	78	7.00091	2.9502		0.52436	0.58064
230	83	7.18276	3.13205		0.480516	0.624484
235	88	7.36574	3.31503		0.435202	0.669798

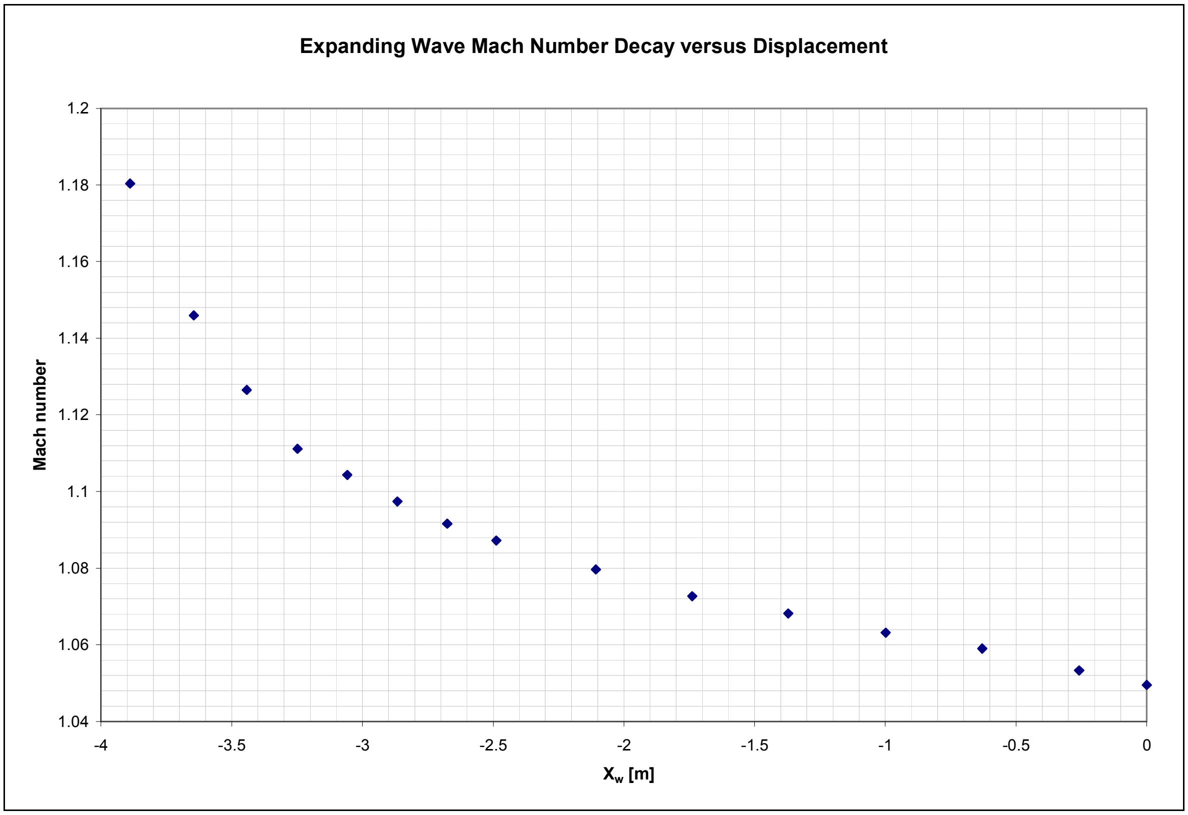

Figure A 7 – Mach number decay of the expanding wave as a function of displacement leading up to the reflection corner

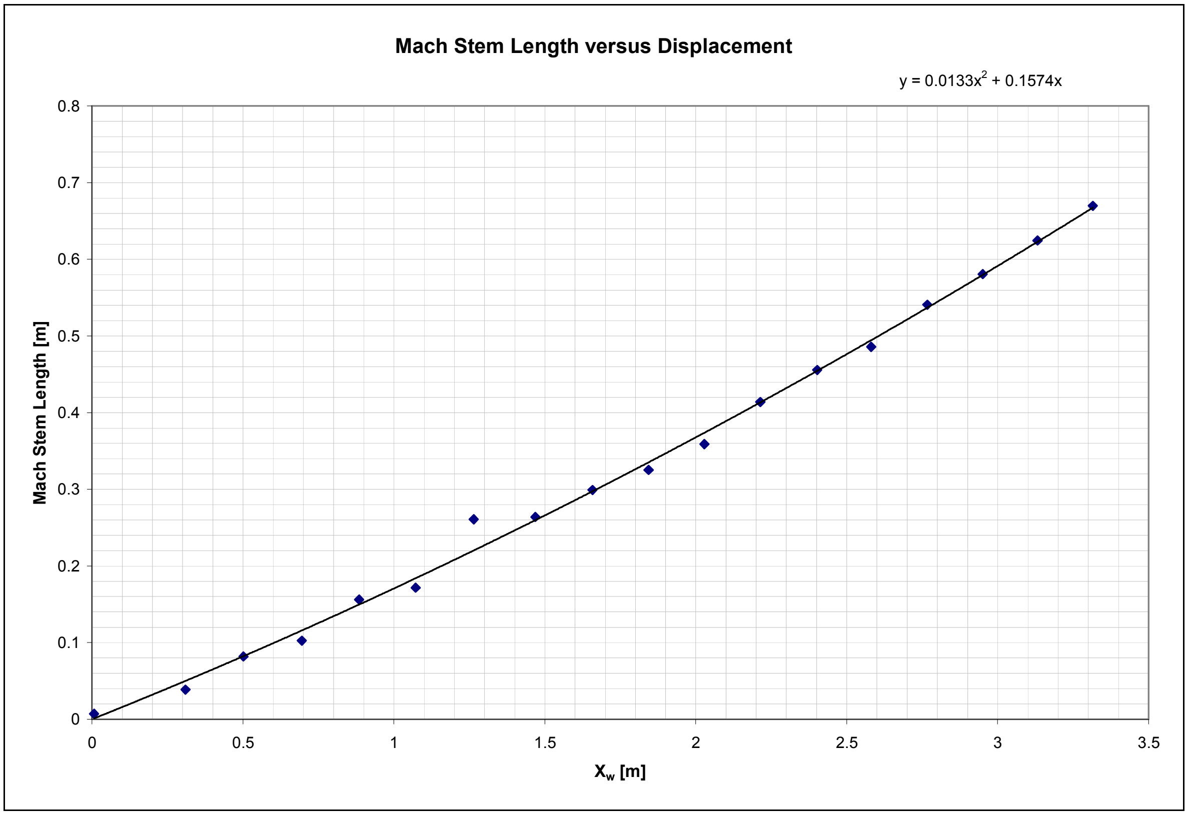

Figure A 8 – Mach stem length versus displacement from the reflection corner

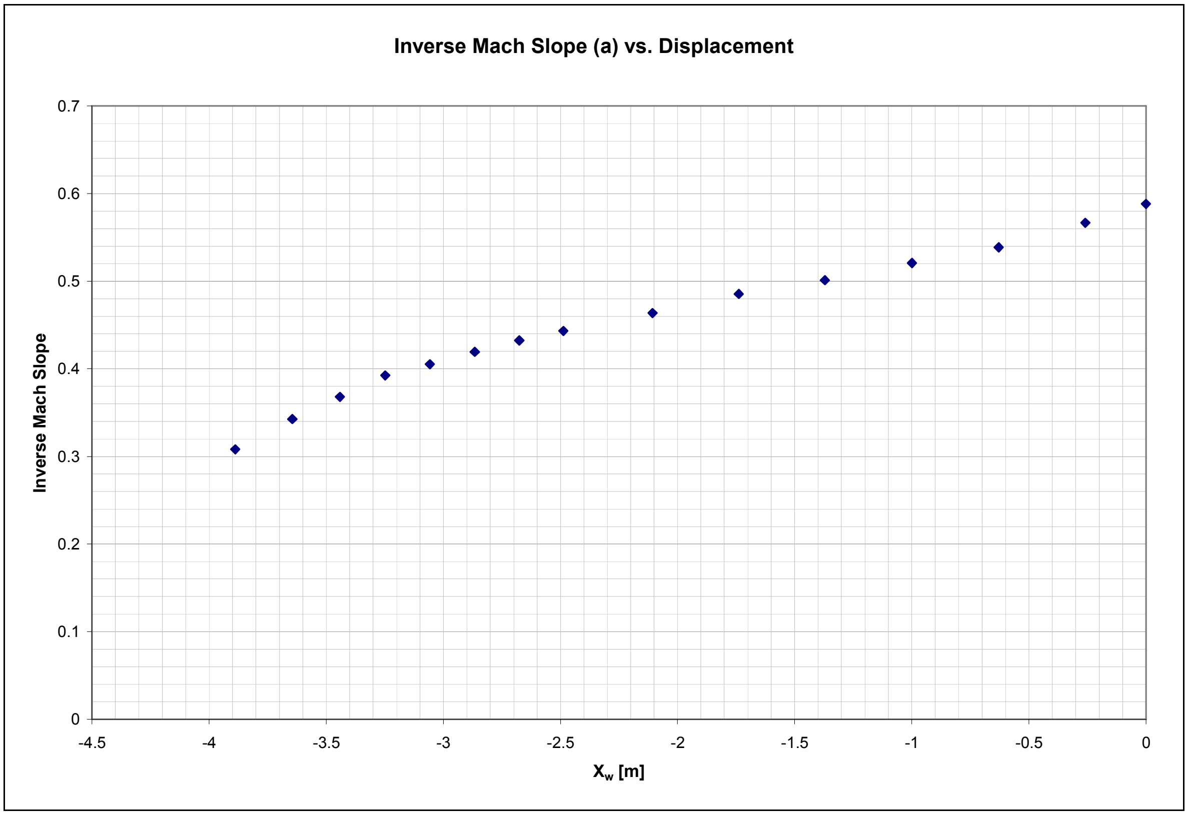

Figure A 9 – Inverse Mach slope as a function of displacement leading up to the reflection corner

Appendix B – Divergent Section Engineering Drawings

The following engineering drawings are reproduced here:

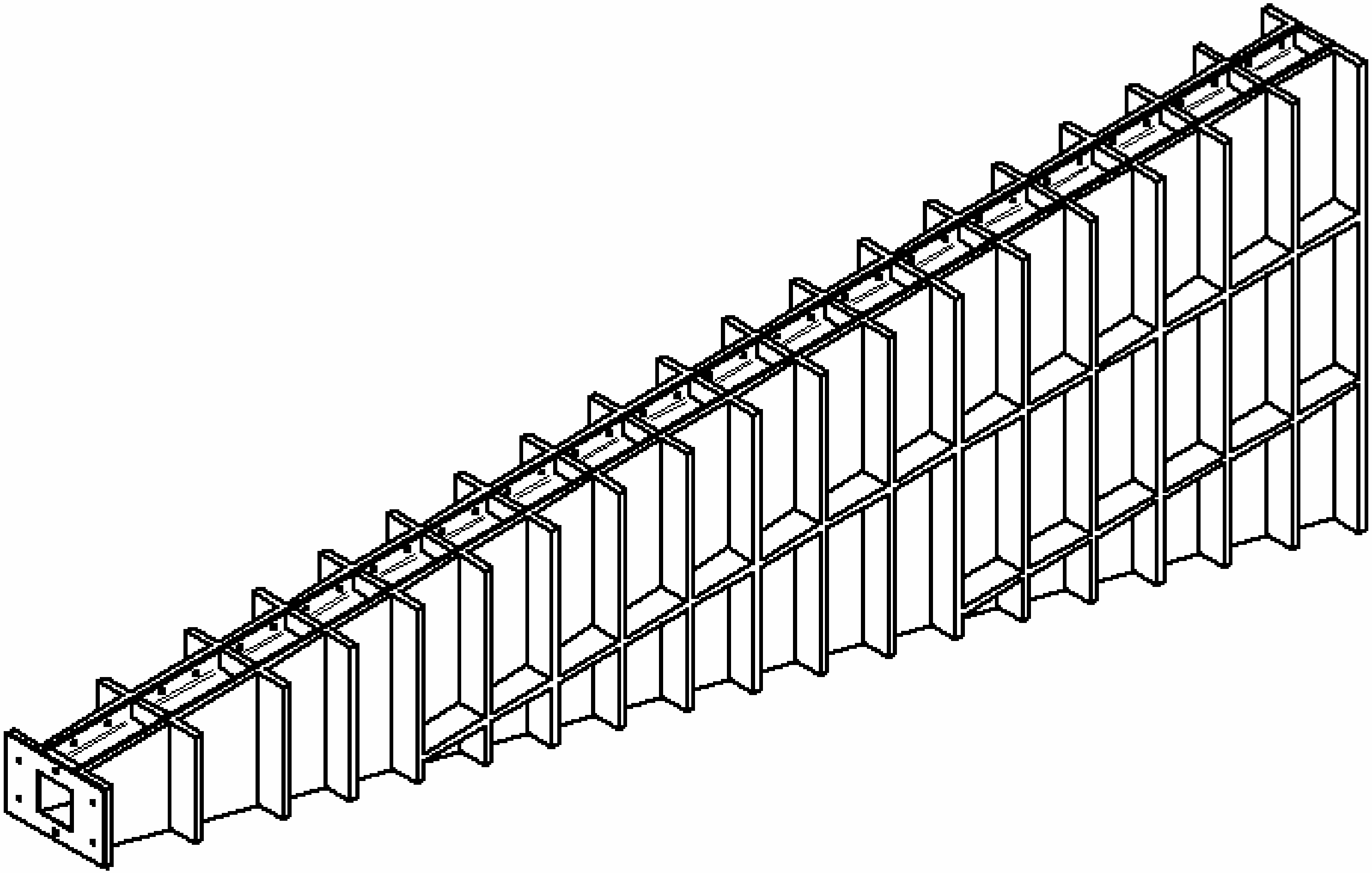

Divergent Section Isometric View

Jason Ashworth 9900131F

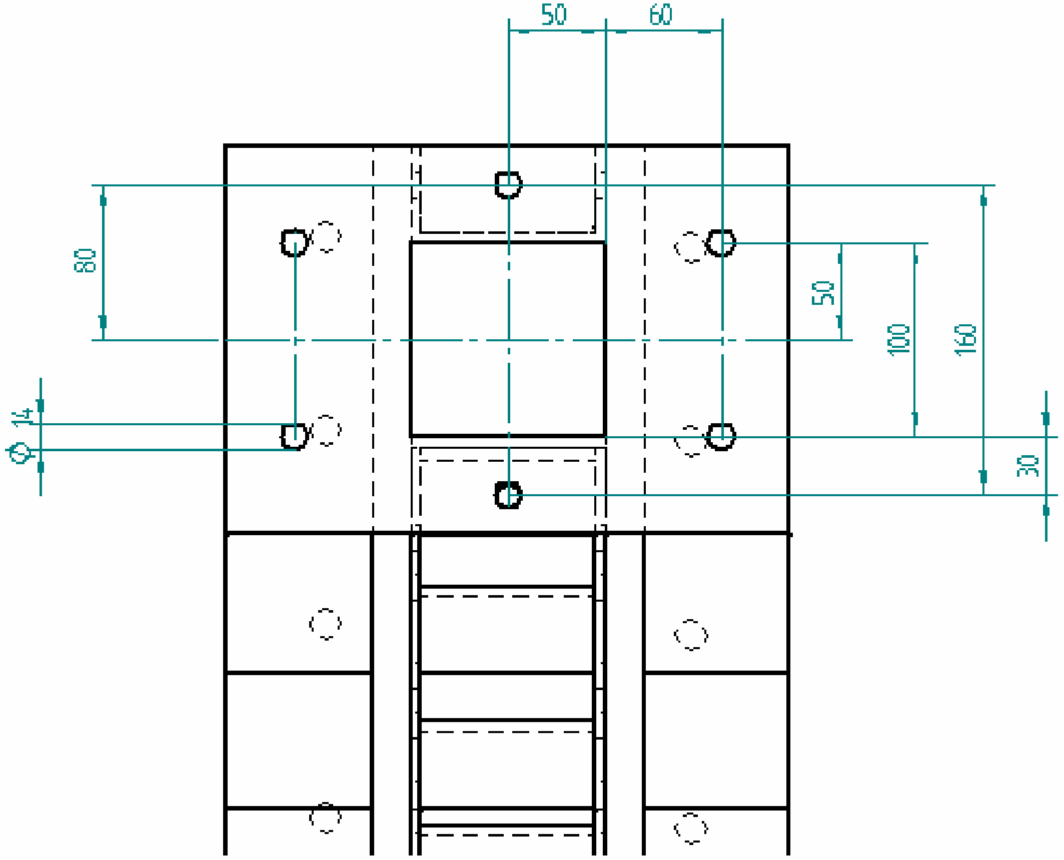

Divergent Section Flange Front View

Jason Ashworth 9900131F

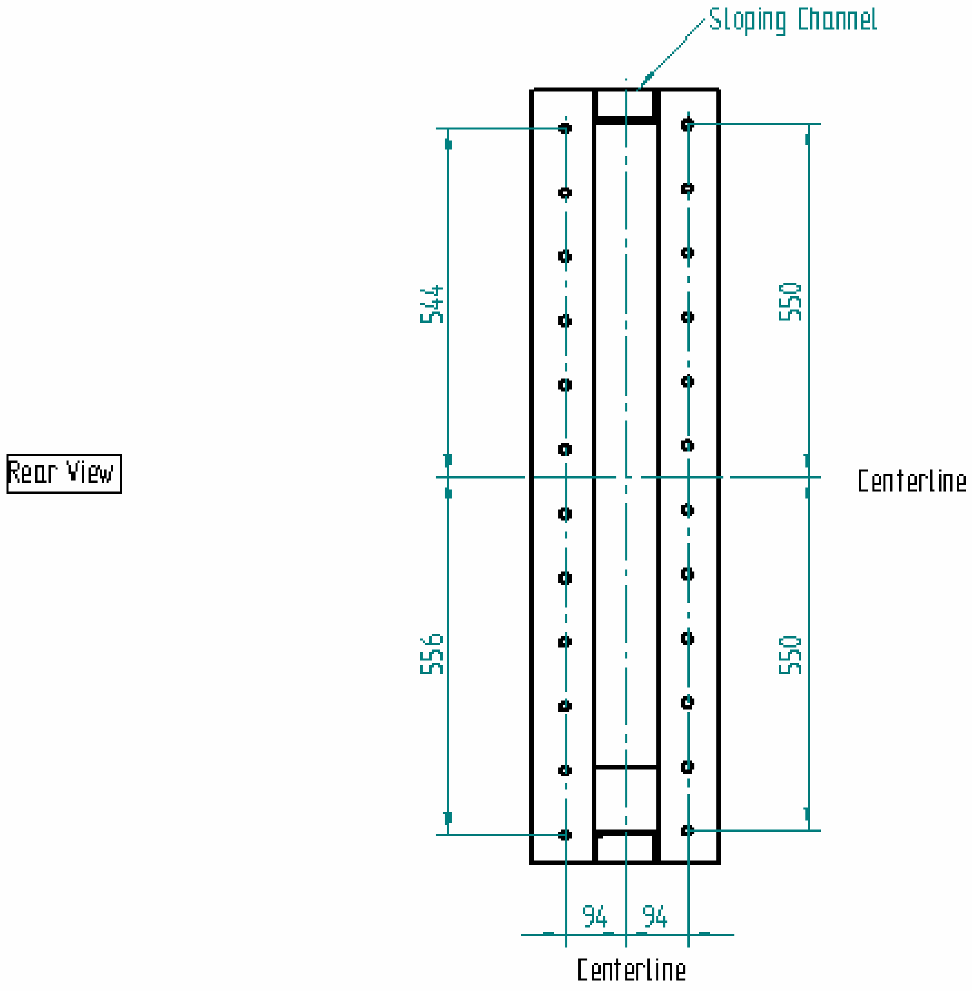

Divergent-Test Section Holes

Jason Ashworth 9900131F

Hole Table		
Hole	X	Y
1.1	-94	544
1.2	-94	444
1.3	-94	344
1.4	-94	244
1.5	-94	144
1.6	-94	44
1.7	-94	-56
1.8	-94	-156
1.9	-94	-256
1.10	-94	-356
1.11	-94	-456
1.12	-94	-556
1.13	94	550
1.14	94	450
1.15	94	350
1.16	94	250
1.17	94	150
1.18	94	50
1.19	94	-50
1.20	94	-150

Hole Table		
Hole	X	Y
1.21	94	-250
1.22	94	-350
1.23	94	-450
1.24	94	-550

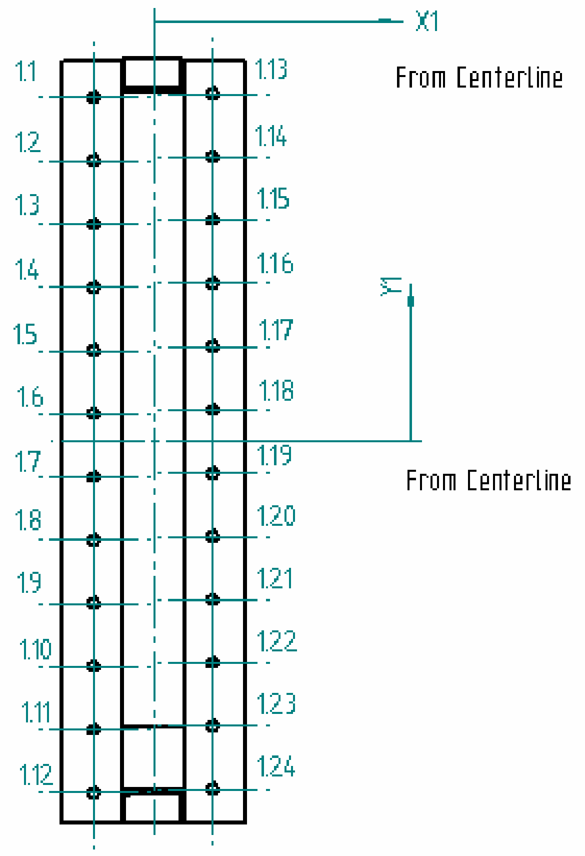

Rear View

Divergent-Test Section Holes

Jason Ashworth 9900131F

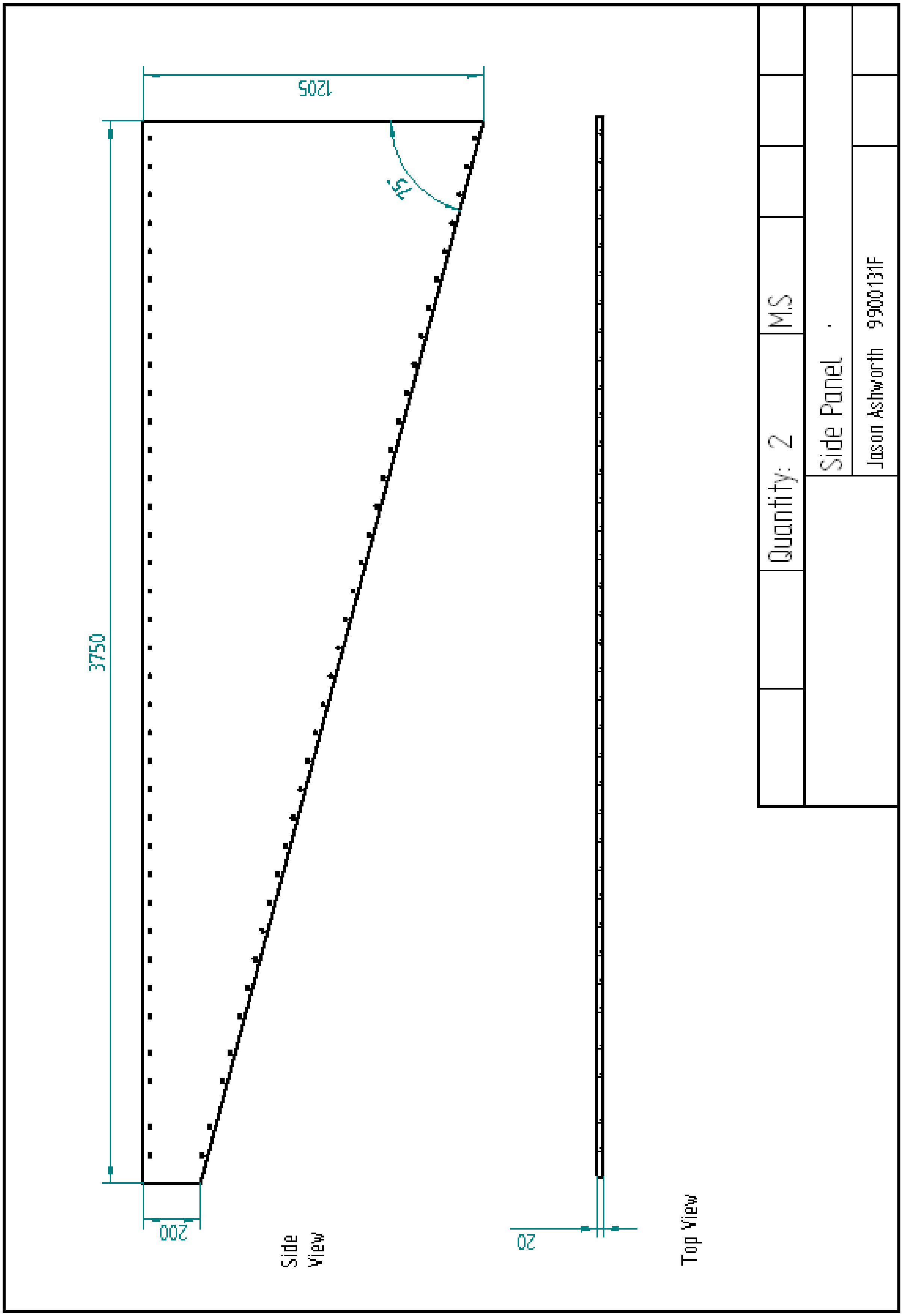
1205
3750
15
200
Side View
20
Top View
Quantity: 2
M.S
Side Panel
Jason Ashworth 9900131F

All holes M14
Threaded

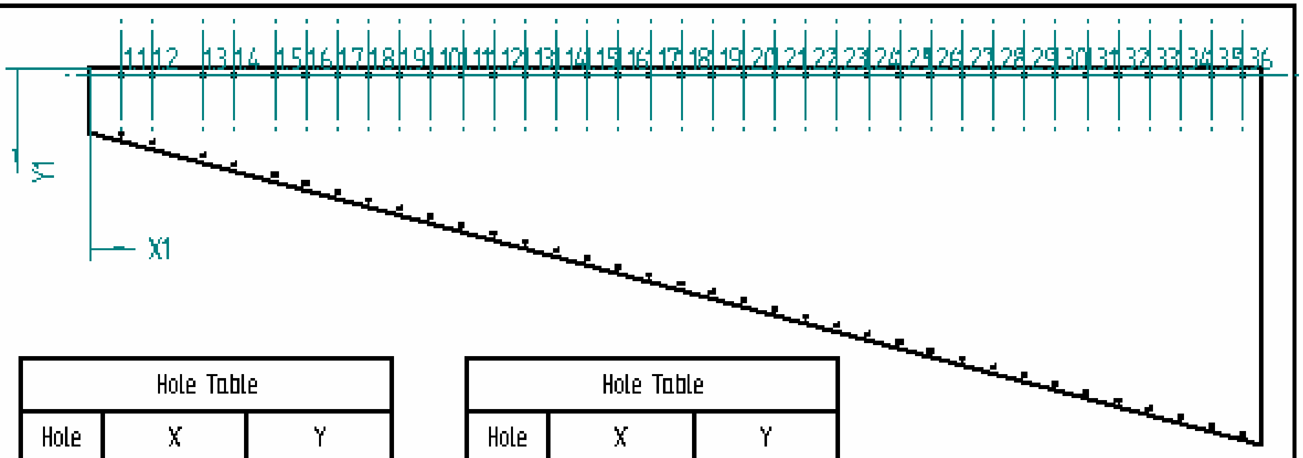

Hole Table		
Hole	X	Y
1.1	97,5	-20
1.2	197,5	-20
13	360	-20
1.4	460	-20
1.5	590	-20
1.6	690	-20
1.7	790	-20
1.8	890	-20
1.9	990	-20
1.10	1090	-20

Hole Table		
Hole	X	Y
1.11	1190	-20
1.12	1290	-20
1.13	1390	-20
1.14	1490	-20
1.15	1590	-20
1.16	1690	-20
1.17	1790	-20
1.18	1890	-20
1.19	1990	-20
120	2090	-20

Hole Table		
Hole	X	Y
1.21	2190	-20
1.22	2290	-20
123	2390	-20
124	2490	-20
125	2590	-20
1.26	2690	-20
1.27	2790	-20
1.28	2890	-20
1.29	2990	-20
130	3090	-20

Hole Table		
Hole	X	Y
1.31	3190	-20
1.32	3290	-20
133	3390	-20
1.34	3490	-20
135	3590	-20
1.36	3690	-20

Side Panel Threaded Holes Table 1
Jason Ashworth 9900131F

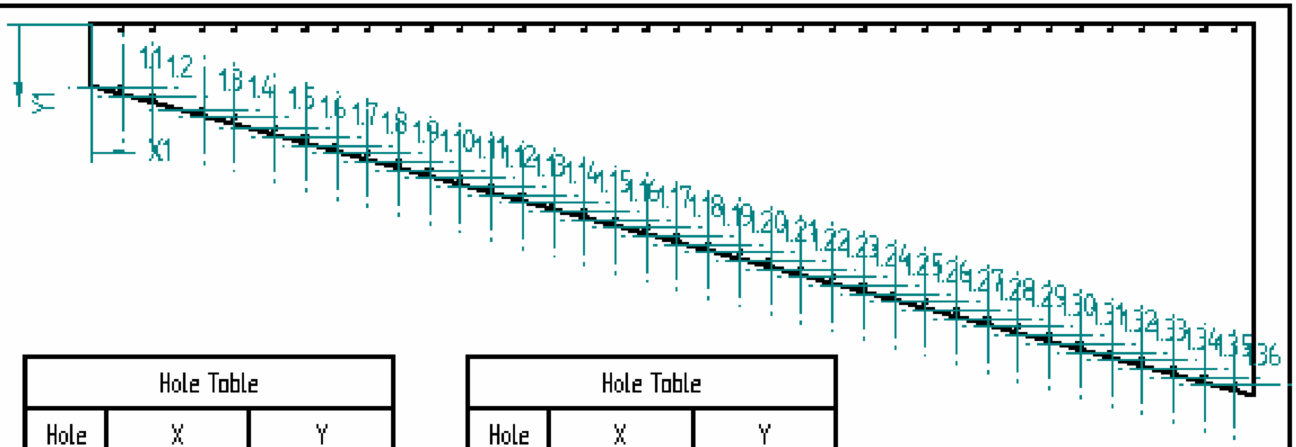

All holes M14
Threaded

Hole Table		
Hole	X	Y
1.1	97,5	-207,18
1.2	197,5	-233,98
13	360	-277,53
1.4	460	-304,33
1.5	590	-339,17
1.6	690	-365,97
1.7	790	-392,77
1.8	890	-419,57
1.9	990	-446,37
1.10	1090	-473,17

Hole Table		
Hole	X	Y
1.11	1190	-499,97
1.12	1290	-526,77
1.13	1390	-553,57
1.14	1490	-580,37
1.15	1590	-607,17
1.16	1690	-633,97
1.17	1790	-660,77
1.18	1890	-687,57
1.19	1990	-714,37
1.20	2090	-741,17

Hole Table		
Hole	X	Y
1.21	2190	-767,97
1.22	2290	-794,77
1.23	2390	-821,57
1.24	2490	-848,37
1.25	2590	-875,17
1.26	2690	-901,97
1.27	2790	-928,77
1.28	2890	-955,57
1.29	2990	-982,37
130	3090	-1009,17

Hole Table		
Hole	X	Y
131	3190	-1035,97
132	3290	-1062,77
133	3390	-1089,57
134	3490	-1116,37
135	3590	-1143,17
136	3690	-1169,97

Side Panel Threaded Holes Table 2

Jason Ashworth 9900131F

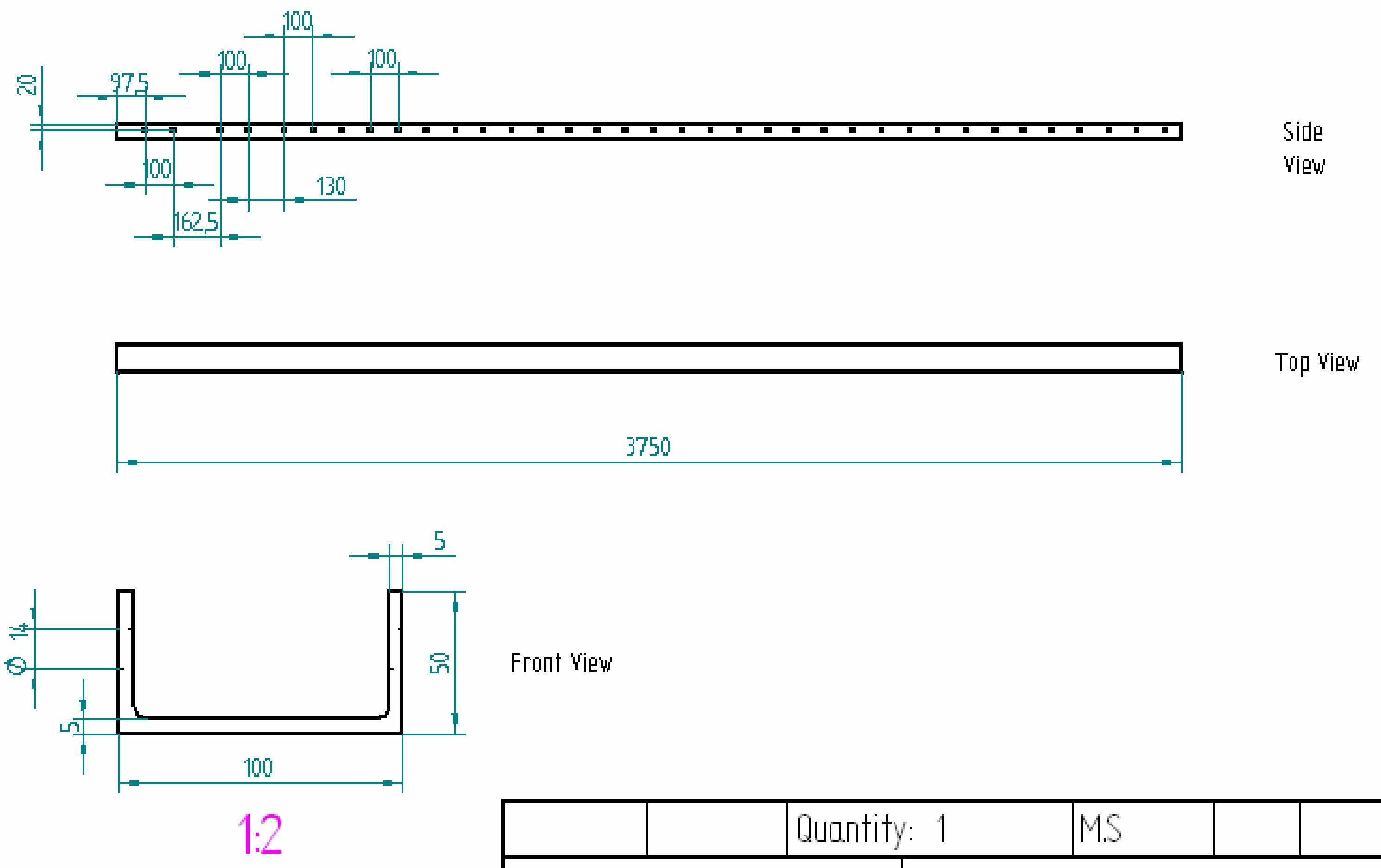

		Quantity: 1	M.S			

(Std. 100x50x5 Steel Channel)	Top Channel ·		
	Jason Ashworth 9900131F		

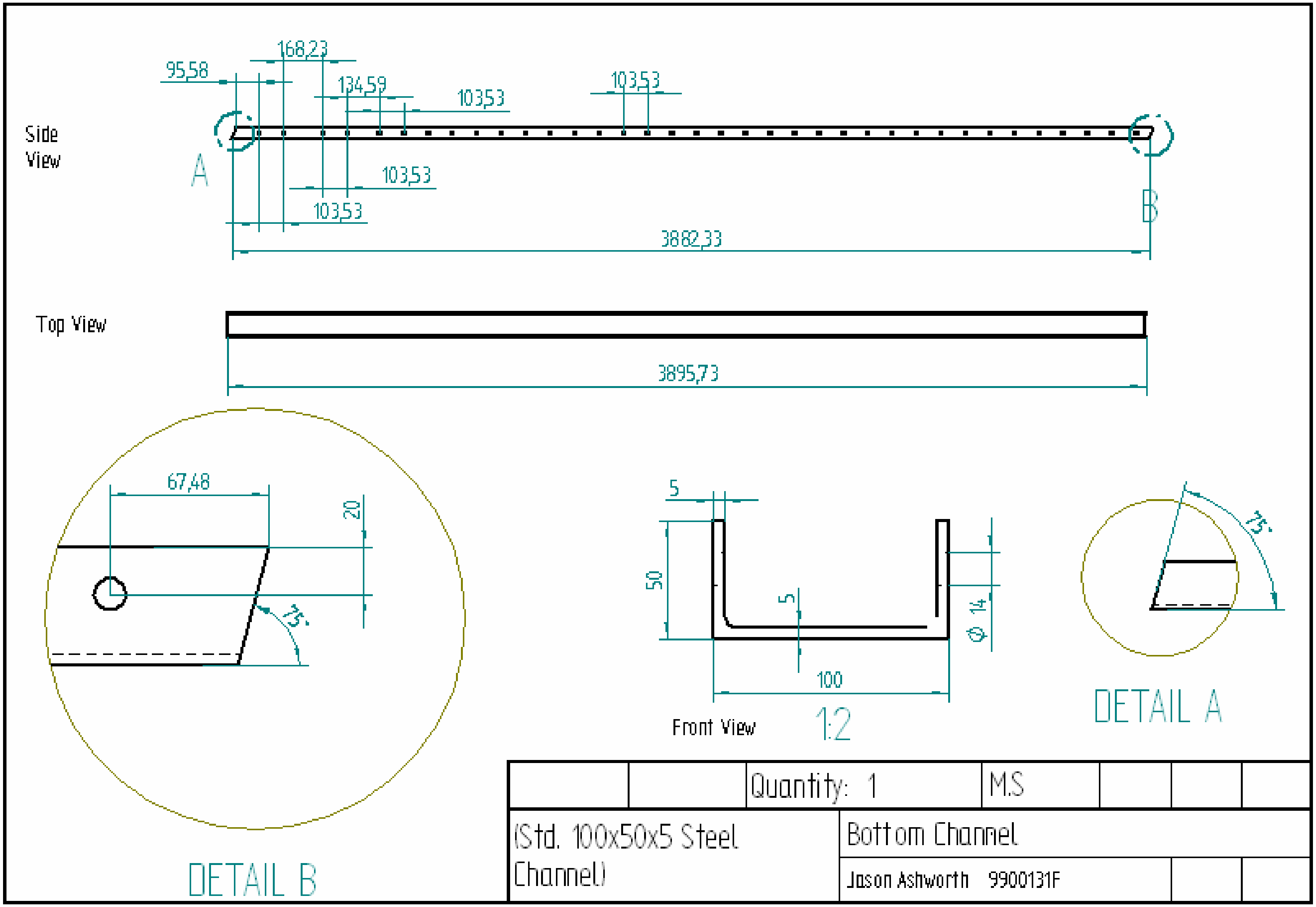
Side View
95,58
168,23
134,59
103,53
103,53
103,53
103,53
A
B
3882,33
Top View
3895,73
67,48
20
75°
DETAIL B
5
50
5
100
Ø 14
Front View
1:2
75°
DETAIL A
Quantity: 1
M.S
(Std. 100x50x5 Steel Channel)
Bottom Channel
Jason Ashworth 9900131F

Appendix C – Driver Section Design and Engineering Drawings

The following engineering drawings are reproduced here:

Cylindrical Pressure Vessel Equations

Hoop Stress:	Longitudinal Stress:
$\sigma_1 = \frac{pr}{t}$	$\sigma_2 = \frac{pr}{2t}$

Radial Stress:

$$(\sigma_3)_{max} = p$$

where: *p* is the pressure applied

r is the inner radius of the pressure vessel

t is the wall thickness of the pressure vessel

Dimensions of the driver tube:

d_o:	outer diameter = 168 mm
d_i:	inner diameter = 146.06 mm
t:	wall thickness = 10.97 mm
l:	length = 1500 mm

Let p = 600 kPa (limit of low-pressure compressor)
Factor of Safety (*F.S.*) = 10.

$\therefore (p)_{max} = 6$ MPa

$$\sigma_1 = \frac{pd_i}{2t} = \frac{(6\times10^6)(146.06\times10^{-3})}{2(10.97\times10^{-3})}$$
$$= 39.94 \text{ MPa}$$

$$\sigma_2 = \frac{pd_i}{4t}$$
$$= 19.97 \text{ MPa}$$

$$(\sigma_3)_{max} = 6 \text{ MPa}$$

The yield-stress (σ_y) of mild steel is approximately 200 MPa; therefore the driver is much stronger than required.

Pressure Testing

The driver section (pressure chamber) was not certified with the relevant ASME code for pressure vessels, since it does not require certification due to its low volume, as well as internal diameter.

The volume of the driver section is:

$$V = A \times L$$
$$= 0.0168 \text{ m}^2 \times 1.5 \text{ m}$$
$$= 0.0252 \text{ m}^3$$

or 25.2 litres, and the internal diameter is 146 mm.

From Chuse (1960), (‘Table 2.23 – Vessels exempt from inspection’):

Vessels not within code jurisdiction:

- Vessels having inside diameter of 6 in. (152.4 mm) or less

From '*ASME Boiler and Pressure Vessel Code, Section VIII, Division 2'* (1968)):

A-121 Classifications Outside Jurisdiction of this Division of Section VIII:

(b) Vessels with a nominal water-containing capacity of 120 gallons (0.4542 m^3) or less for containing water under pressure, including those containing air, the compression of which serves only as a cushion;

(e) Vessels having an inside diameter not exceeding 6 in. (152.4 mm), with no limitation on pressure.

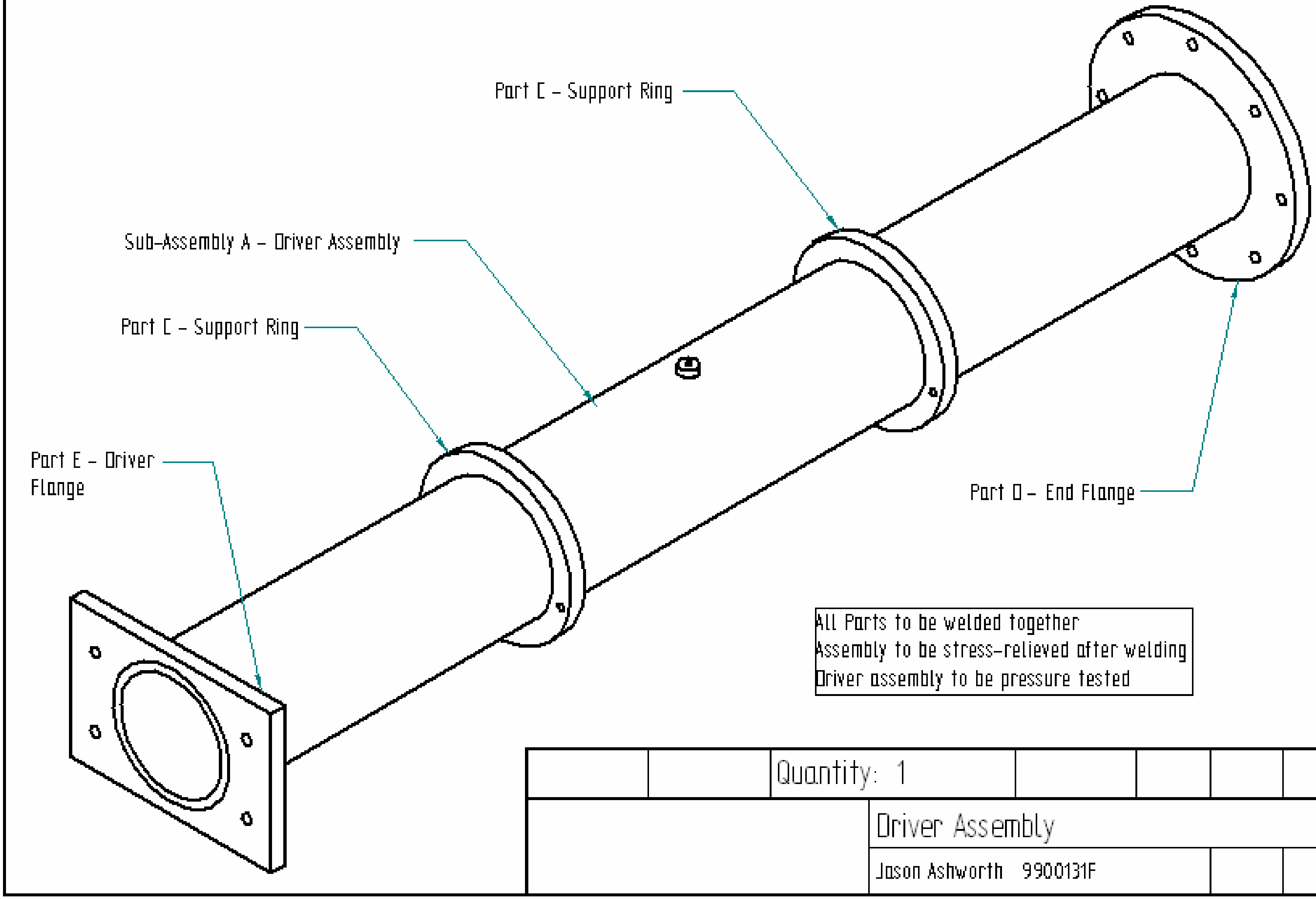

All Parts to be welded together
Assembly to be stress-relieved after welding
Driver assembly to be pressure tested

Quantity: 1

Driver Assembly

Jason Ashworth 9900131F

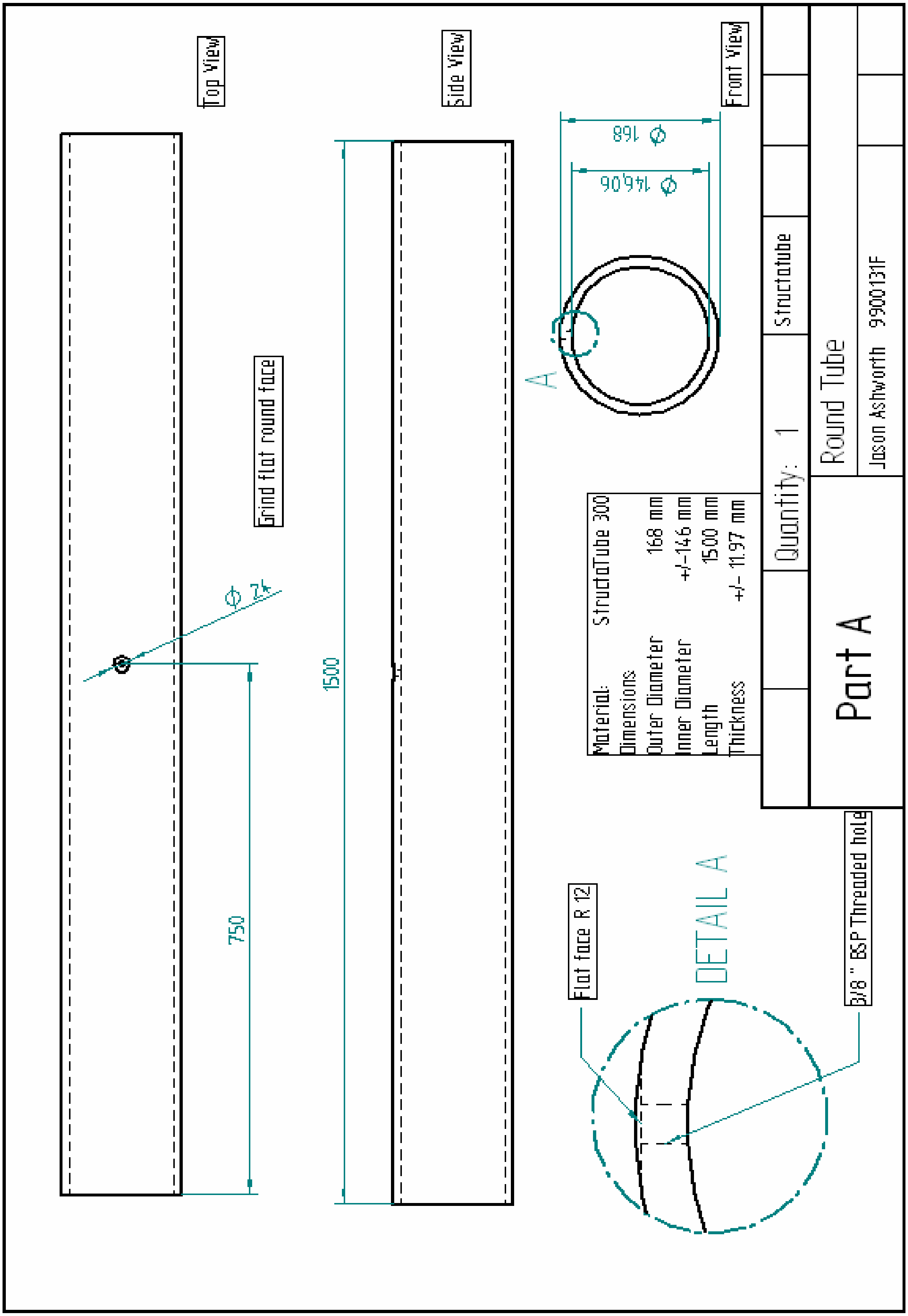
Top View
Side View
Front View
Grind flat round face
Ø 24
750
1500
Ø 168
Ø 146,06
A
DETAIL A
Flat face R 12
3/8 " BSP Threaded hole
Material: StructaTube 300
Dimensions
Outer Diameter 168 mm
Inner Diameter +/-146 mm
Length 1500 mm
Thickness +/- 11.97 mm
Quantity: 1
Structatube
Part A
Round Tube
Jason Ashworth 9900131F

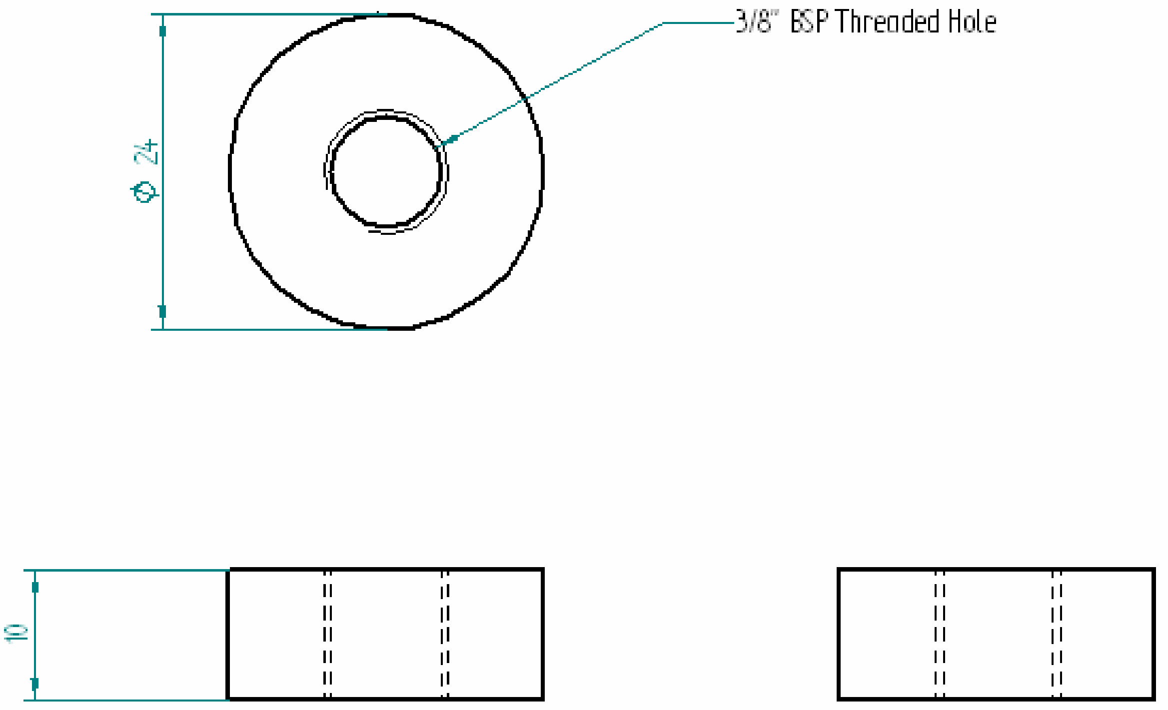

	M.S.	Quantity: 1				
Part B		Inlet Plug				
		Jason Ashworth 9900131F				

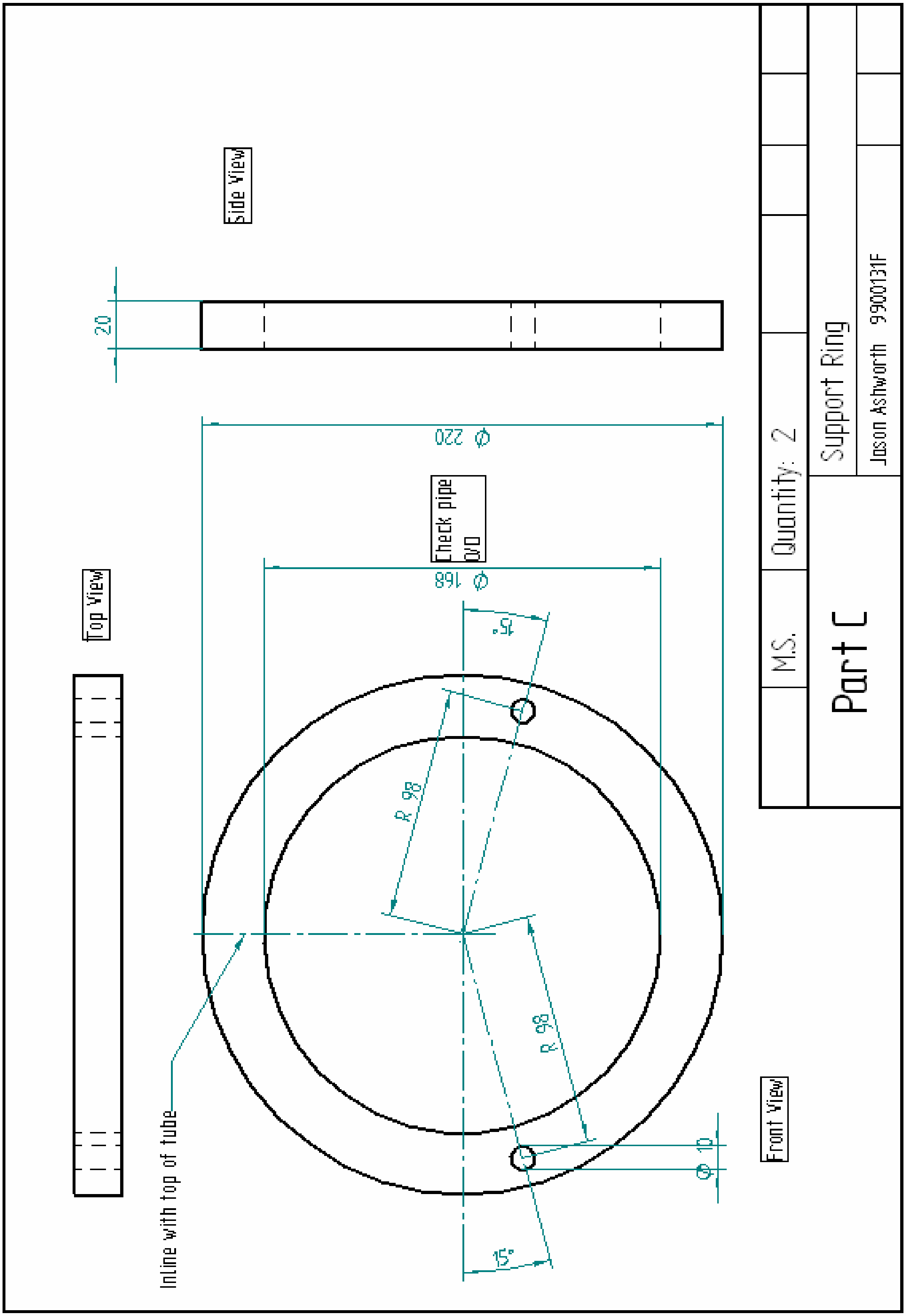
Side View
20
Top View
Inline with top of tube
Front View
Check pipe O/D
Φ 220
Φ 168
15°
R 98
R 98
Φ 10
15°
M.S.
Quantity: 2
Part C
Support Ring
Jason Ashworth 9900131F

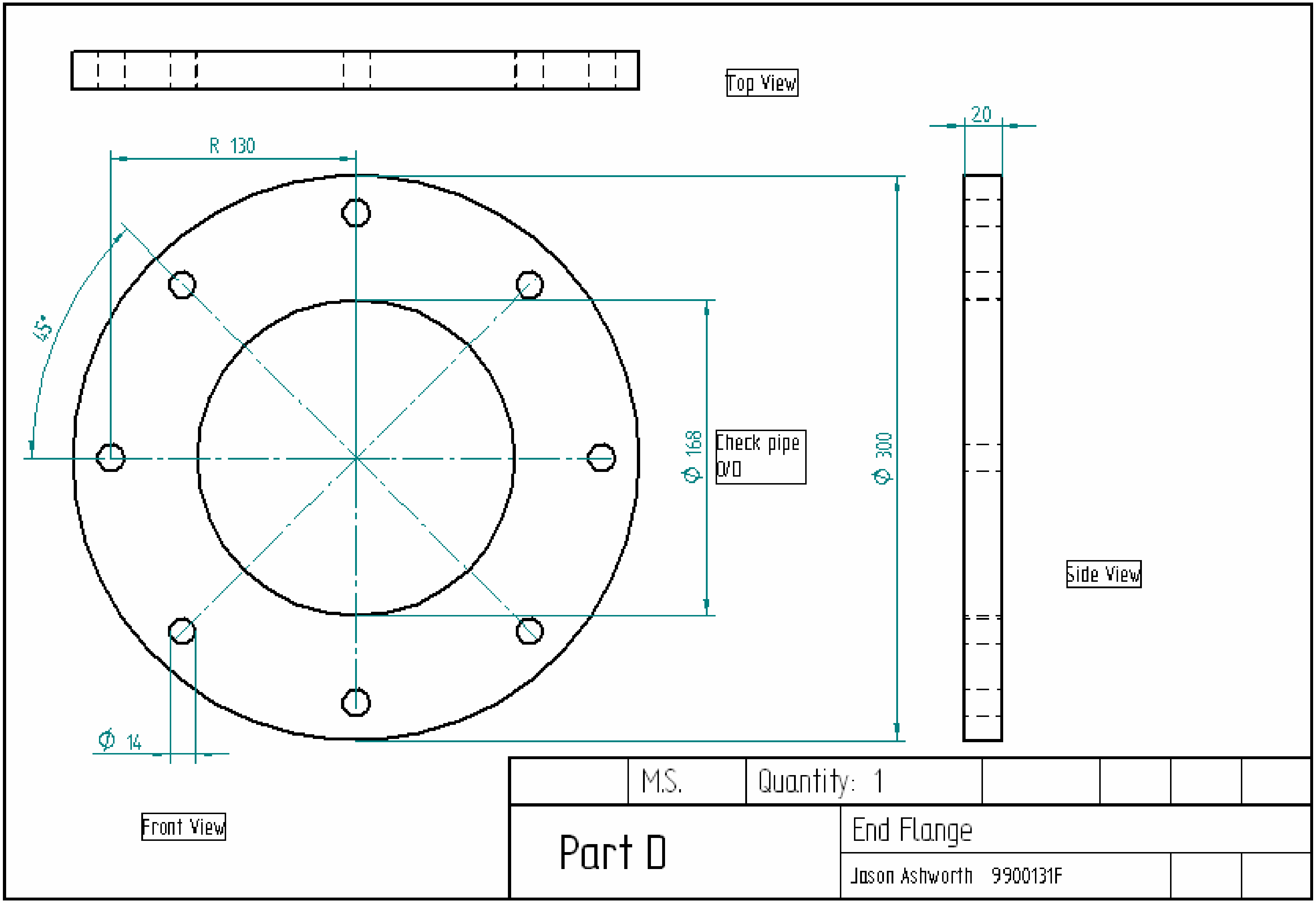
Top View
R 130
45°
20
Φ 168
Check pipe
O/D
Φ 300
Side View
Φ 14
Front View
M.S.
Quantity: 1
Part D
End Flange
Jason Ashworth 9900131F

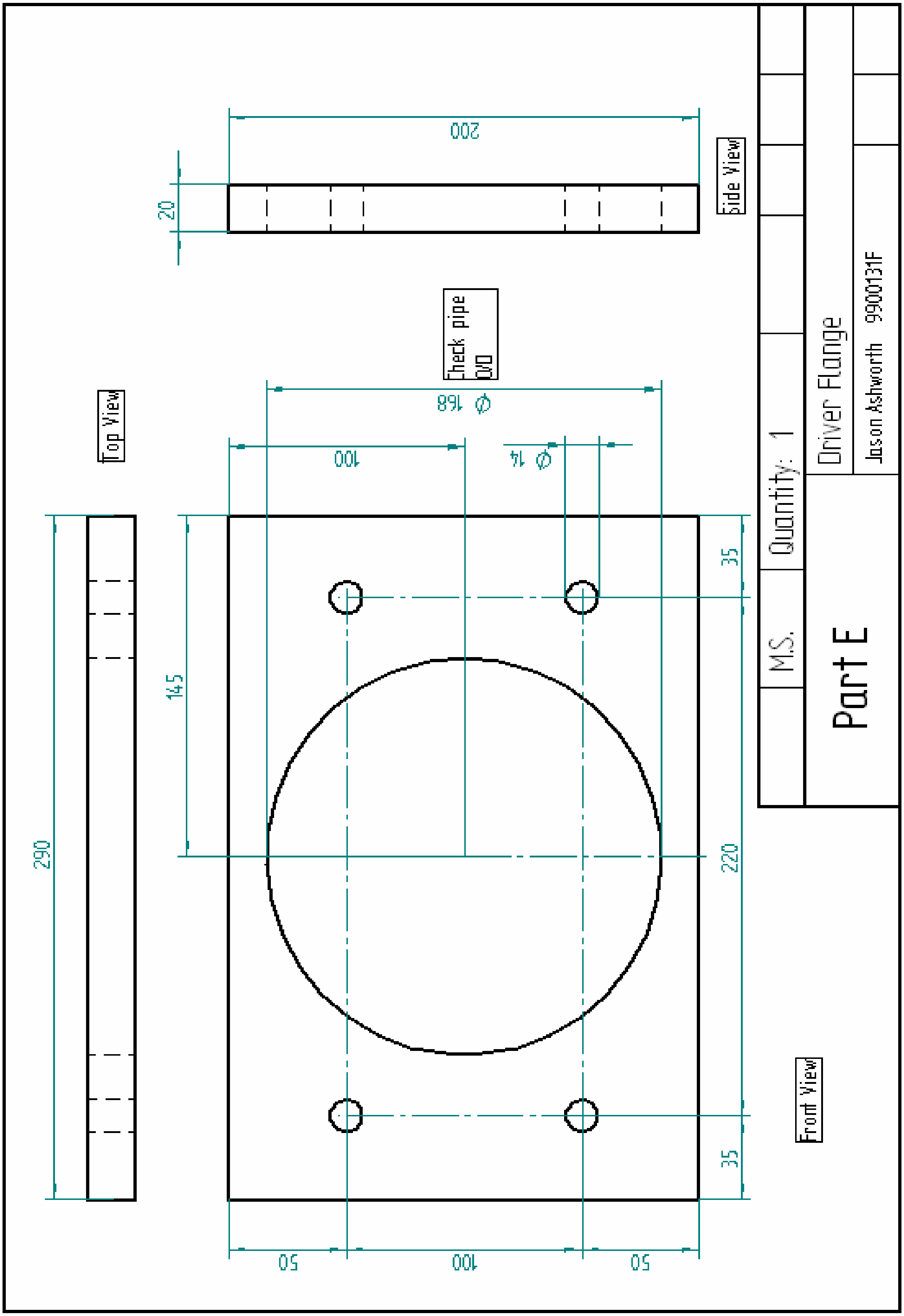
Top View
290
Side View
200
20
Front View
145
100
Ø 168
Check pipe OD
Ø 14
35
220
35
50
100
50
Quantity: 1
M.S.
Driver Flange
Jason Ashworth 9900131F
Part E

Appendix D – Plunger Section Engineering Drawings

The following engineering drawings are reproduced here:

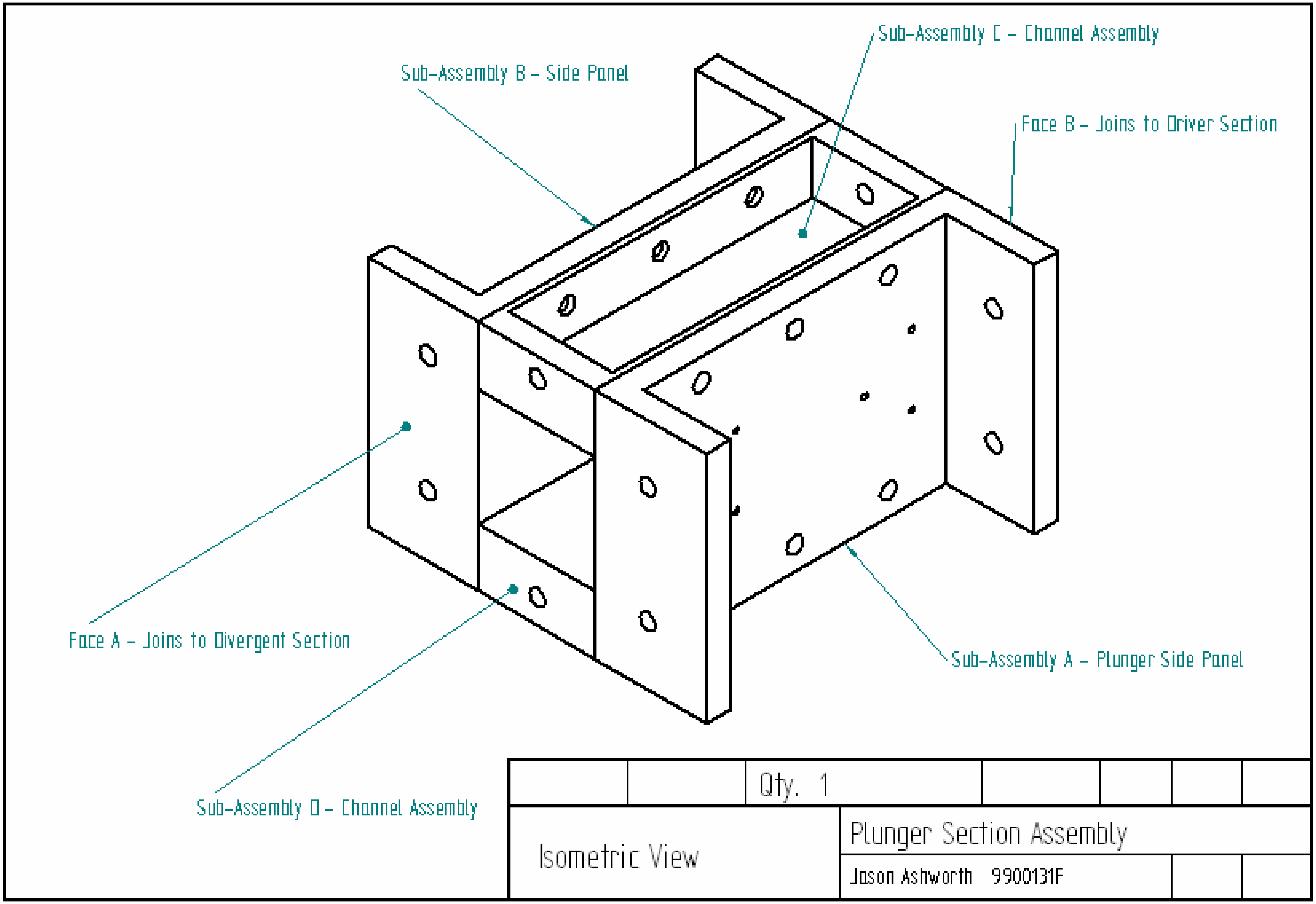

Qty. 1

Isometric View

Plunger Section Assembly

Jason Ashworth 9900131F

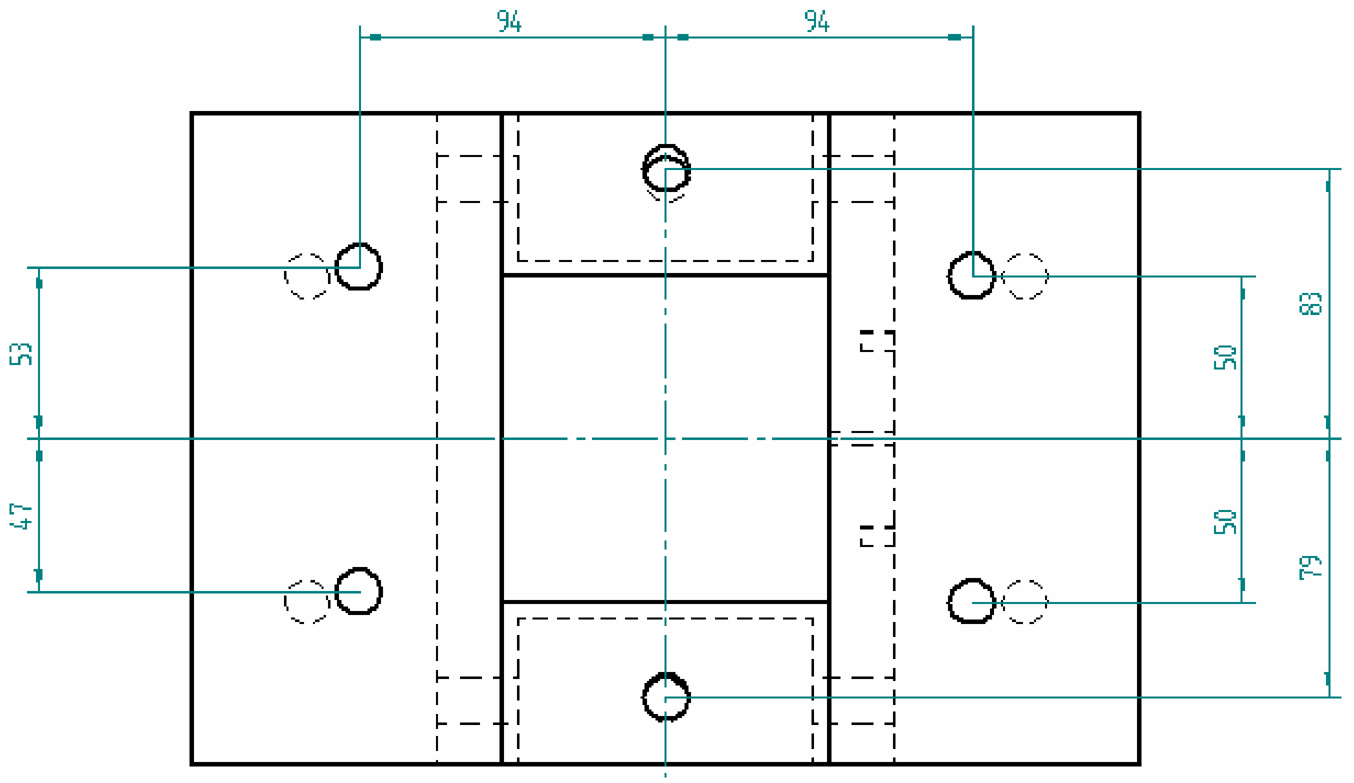

All holes on this face Diameter 14 mm

Rear View – Face to join with Divergent Section

Qty. 1

M.S

Plunger Section Assembly

Jason Ashworth 9900131F

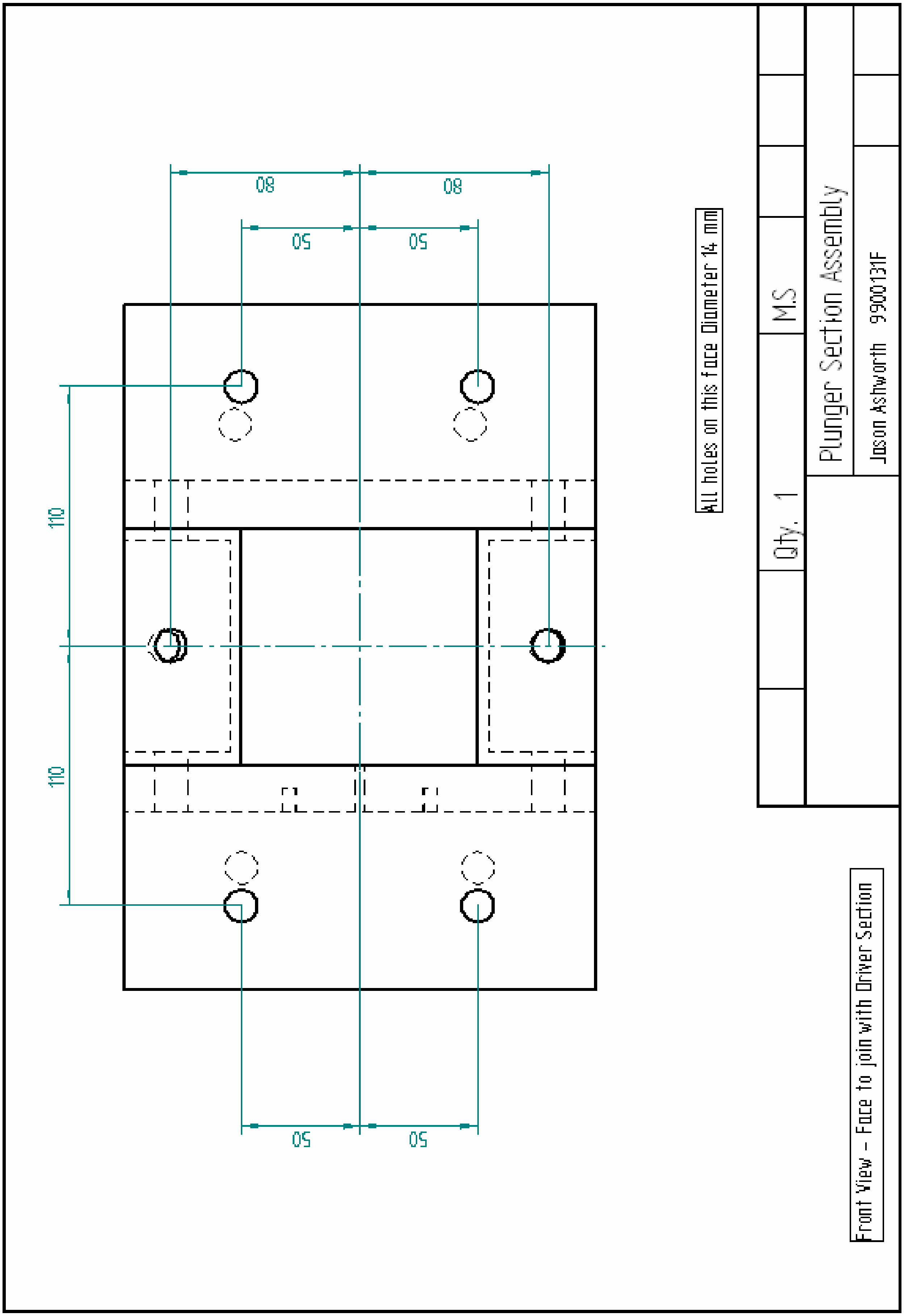
80
80
50
50
110
110
50
50
All holes on this face Diameter 14 mm
Qty. 1
M.S
Plunger Section Assembly
Jason Ashworth 9900131F
Front View - Face to join with Driver Section

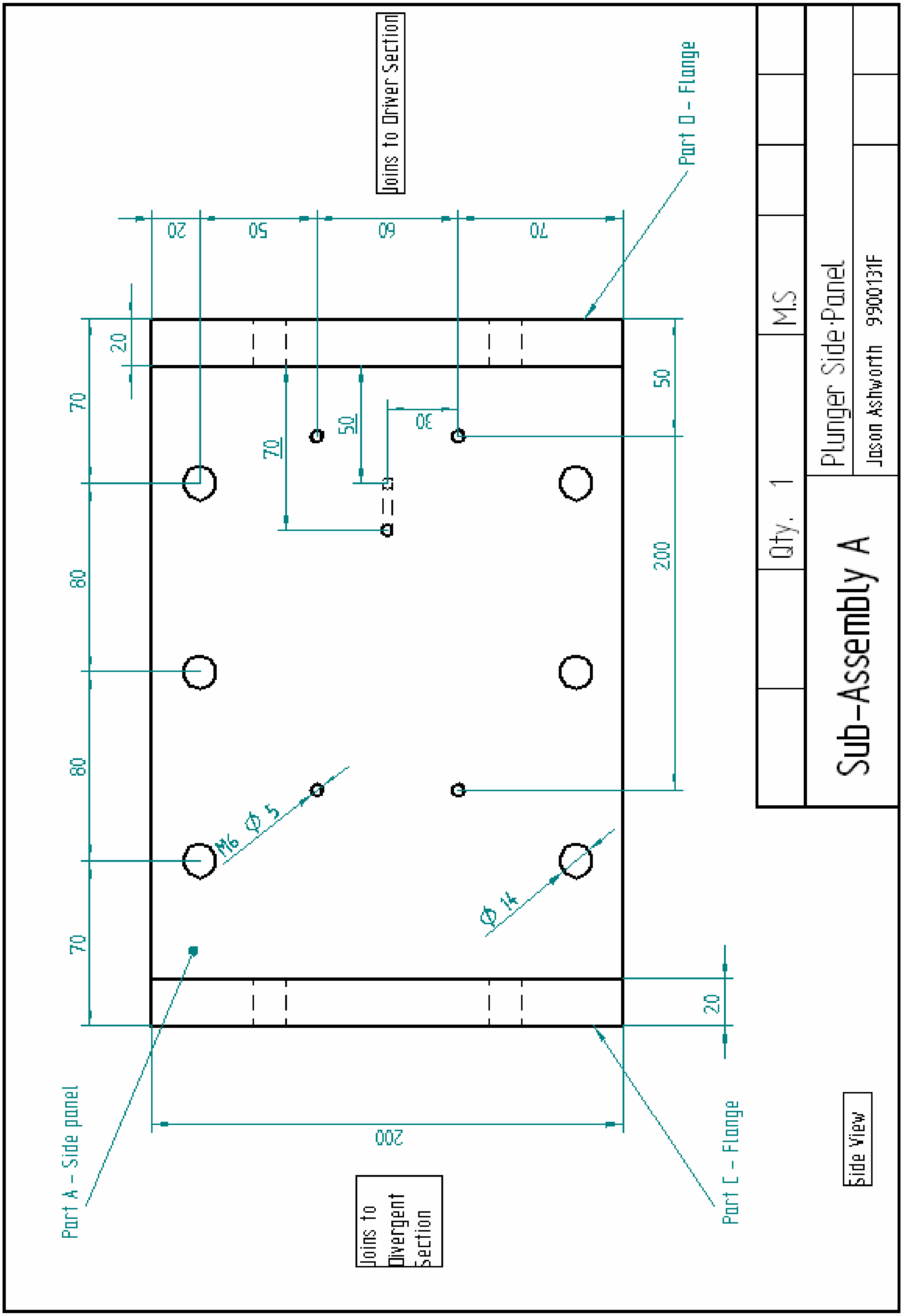
Sub-Assembly A
Plunger Side·Panel
Jason Ashworth 9900131F
Qty. 1
M.S
Side View
Joins to Driver Section
Joins to Divergent Section
Part A - Side panel
Part C - Flange
Part D - Flange
Ø 14
M6 Ø 5
70
80
80
70
20
20
200
200
50
20
50
60
70
70
50
30

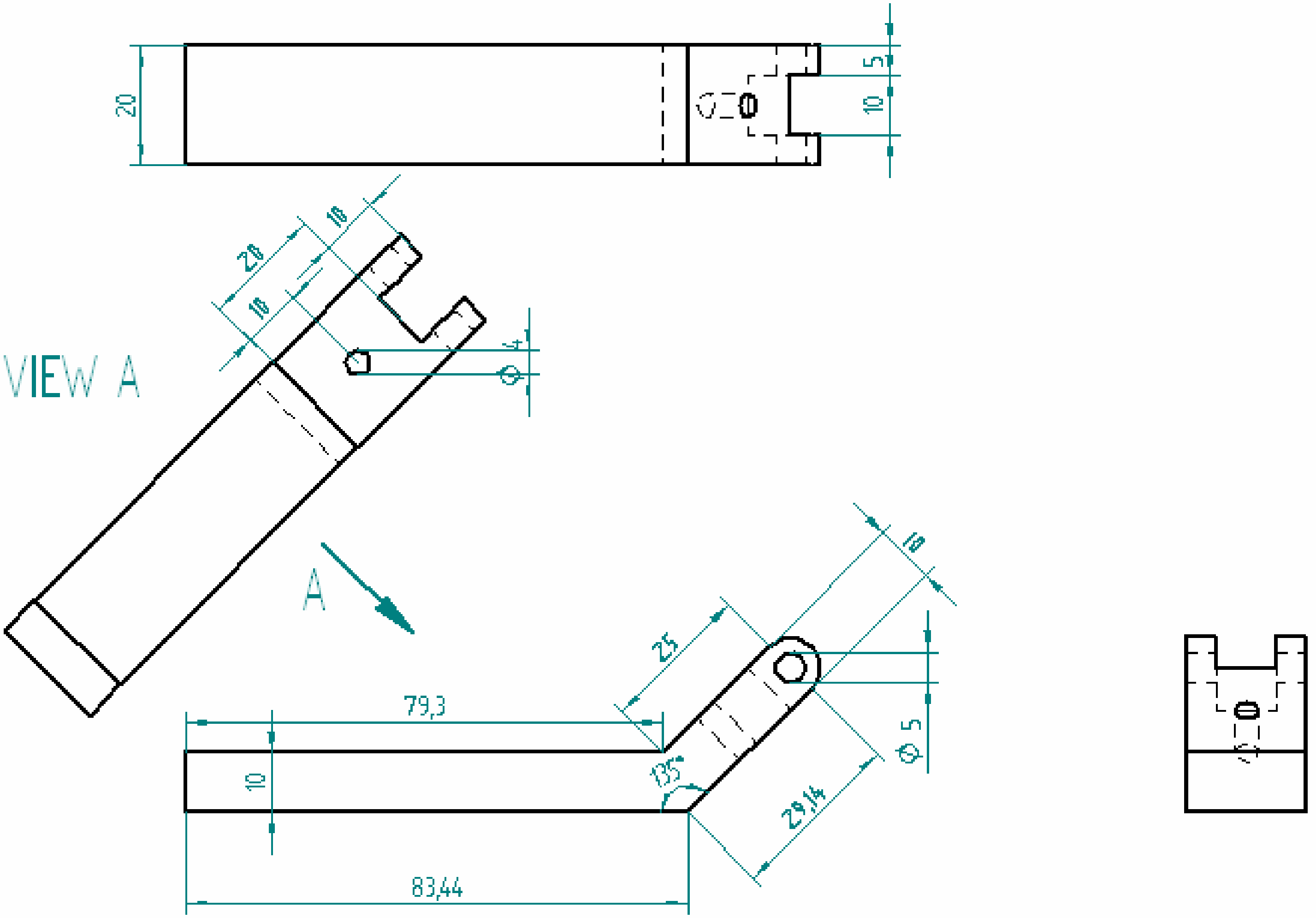

Qty. 1

M.S

Pricker Arm ·

Jason Ashworth 9900131F

Appendix E – Supports and Ports Engineering Drawings

The following engineering drawings are reproduced here:

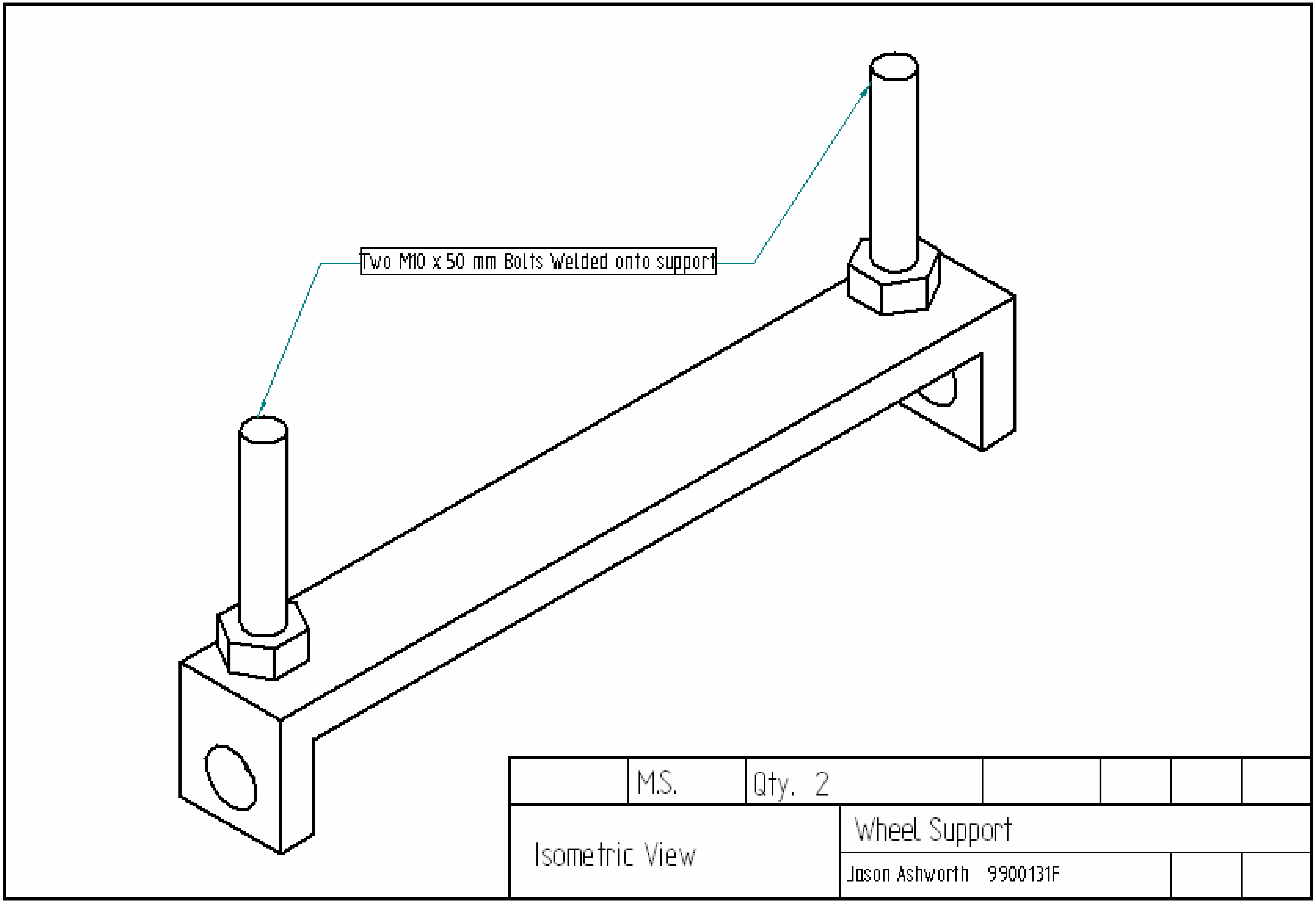
Two M10 x 50 mm Bolts Welded onto support
M.S.
Qty. 2
Isometric View
Wheel Support
Jason Ashworth 9900131F

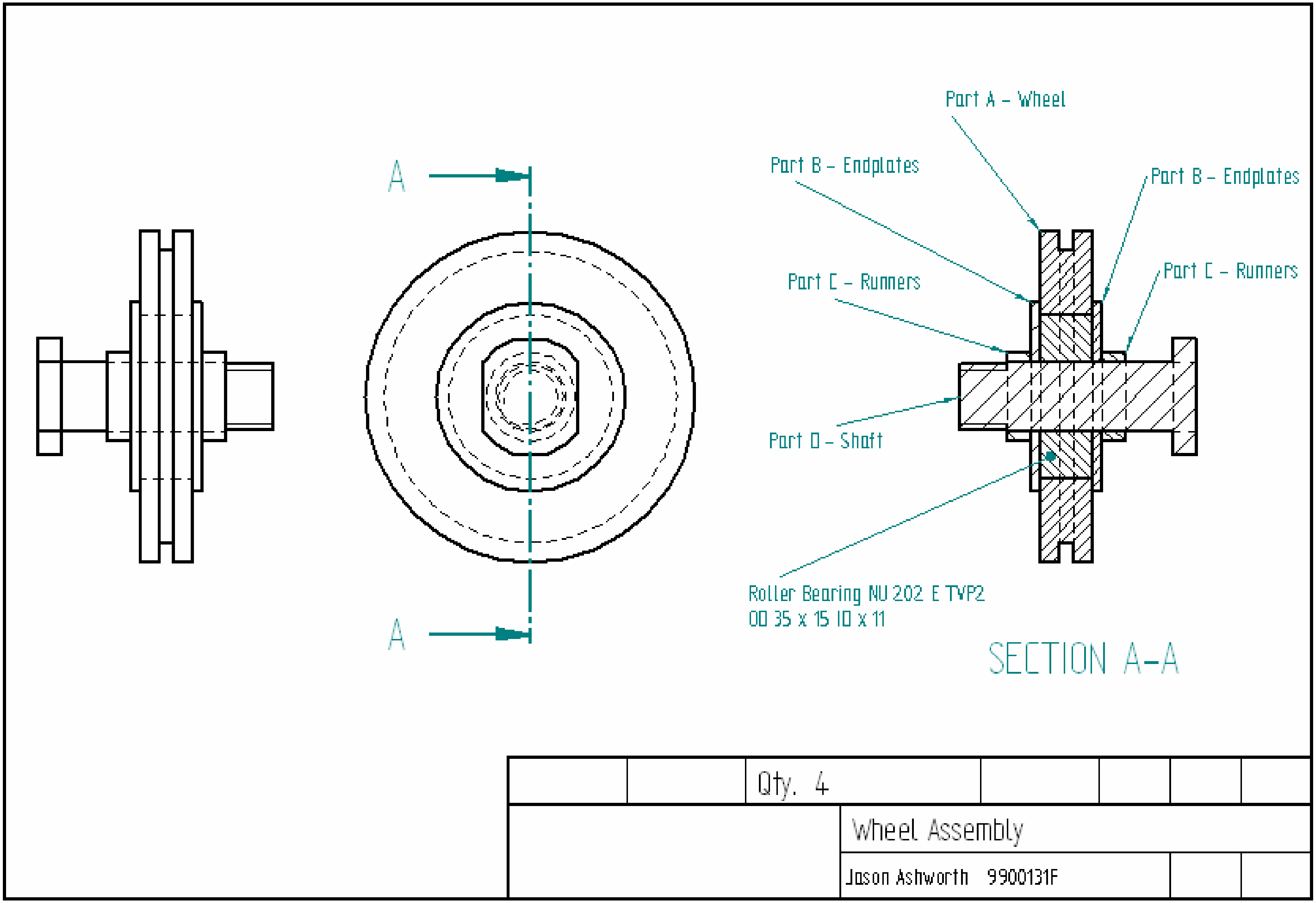
A
A
Part A – Wheel
Part B – Endplates
Part B – Endplates
Part C – Runners
Part C – Runners
Part D – Shaft
Roller Bearing NU 202 E TVP2
OD 35 x 15 ID x 11
SECTION A–A
Qty. 4
Wheel Assembly
Jason Ashworth 9900131F

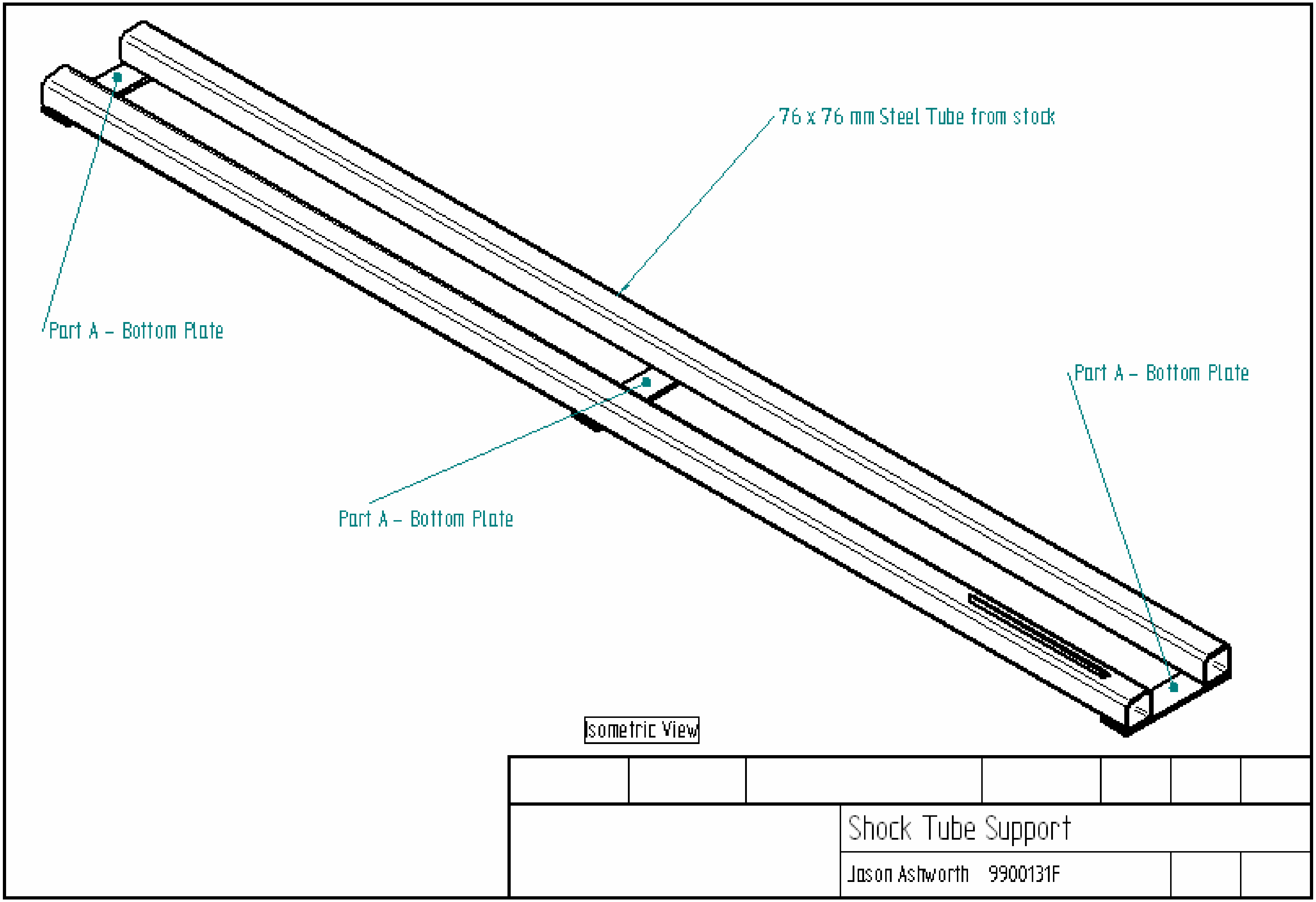
76 x 76 mm Steel Tube from stock
Part A – Bottom Plate
Part A – Bottom Plate
Part A – Bottom Plate
Isometric View
Shock Tube Support
Jason Ashworth 9900131F

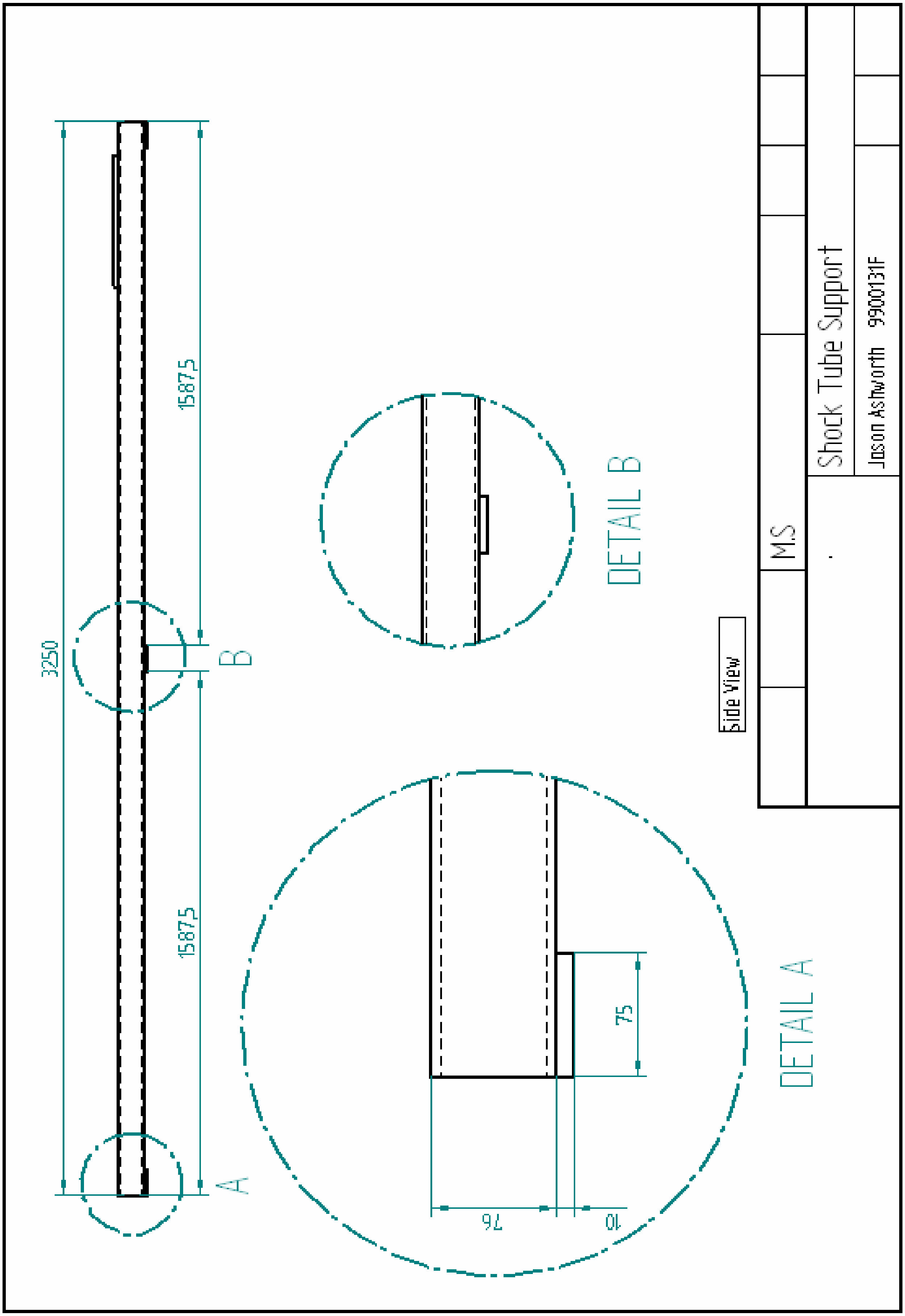
3250
15875
15875
A
B
DETAIL A
DETAIL B
75
76
10
Side View
M.S
Shock Tube Support
Jason Ashworth 9900131F

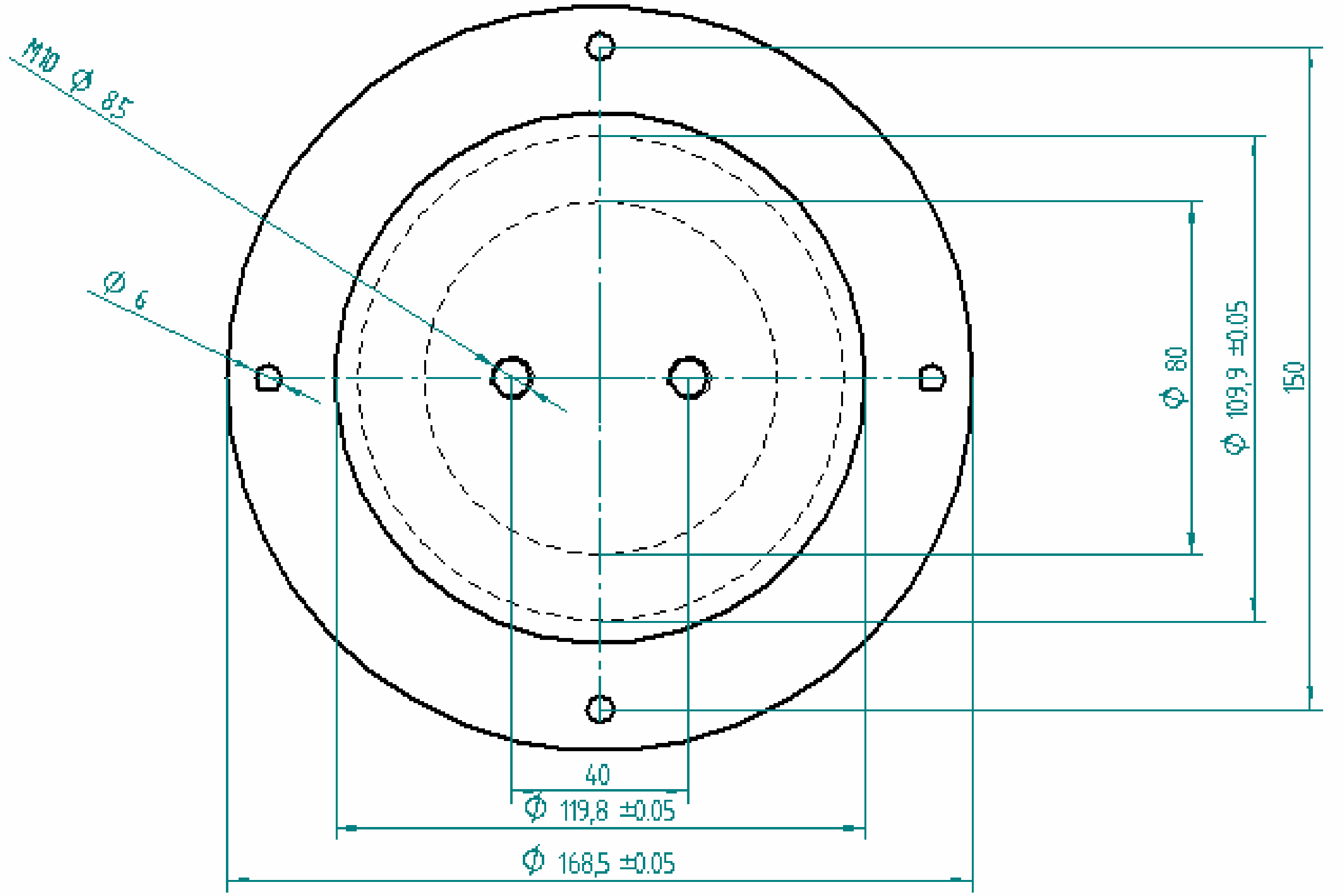

Quantity: 3 M.S

Removable Port 1

Jason Ashworth 9900131F

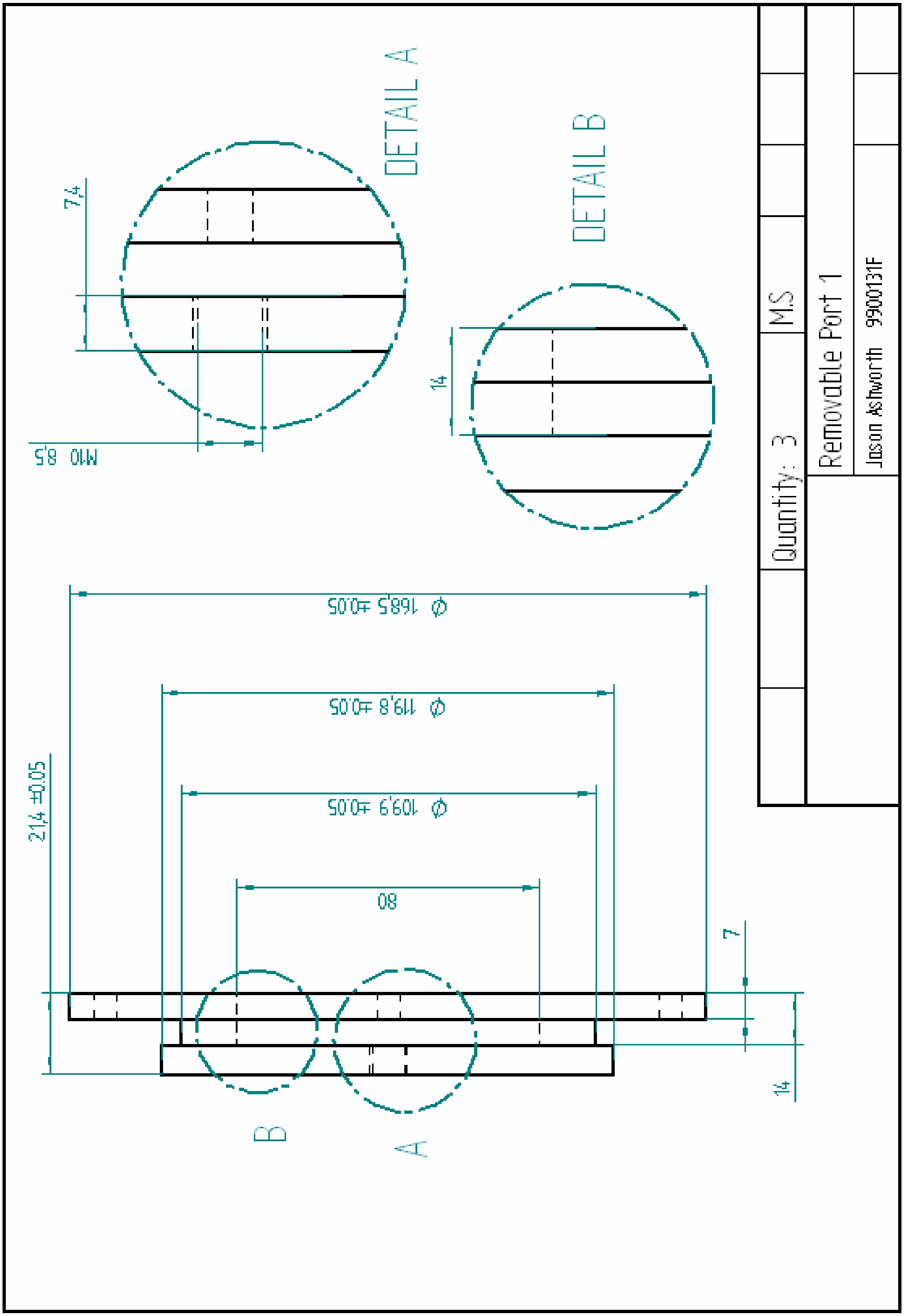
DETAIL A
DETAIL B
7,4
M10 8,5
14
Ø 168,5 ±0,05
Ø 119,8 ±0,05
Ø 109,9 ±0,05
80
21,4 ±0,05
7
14
B
A
Quantity: 3
MS
Removable Port 1
Jason Ashworth 9900131F

Appendix F – Schlieren Photographs

Contrast-adjusted images are presented here.

Film A

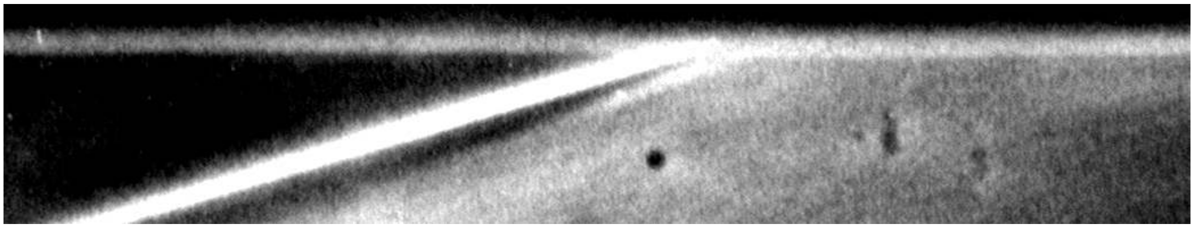

Figure F 1 – A06 with adjusted contrast

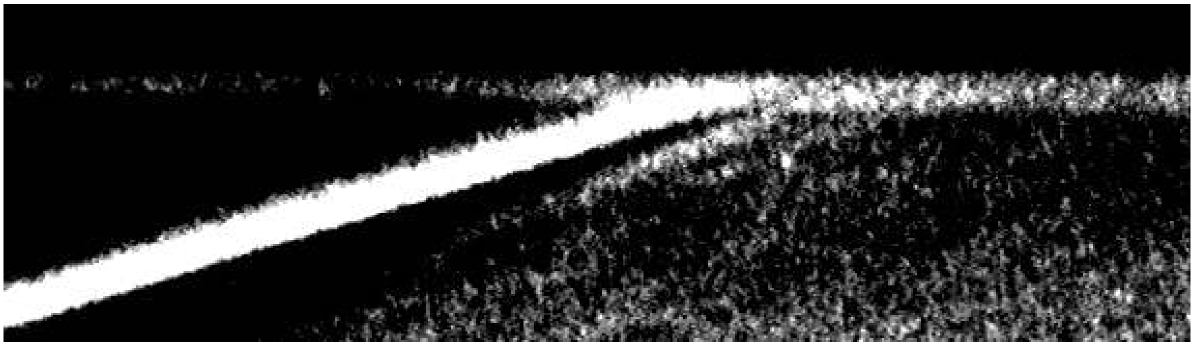

Figure F 2 - A07 with adjusted contrast

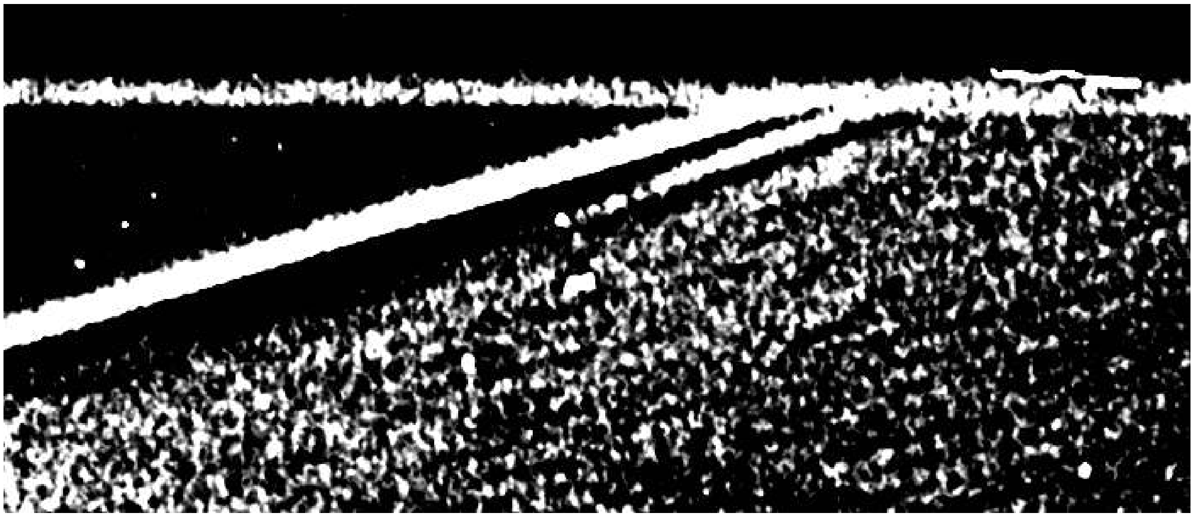

Figure F 3 – A08 with adjusted contrast

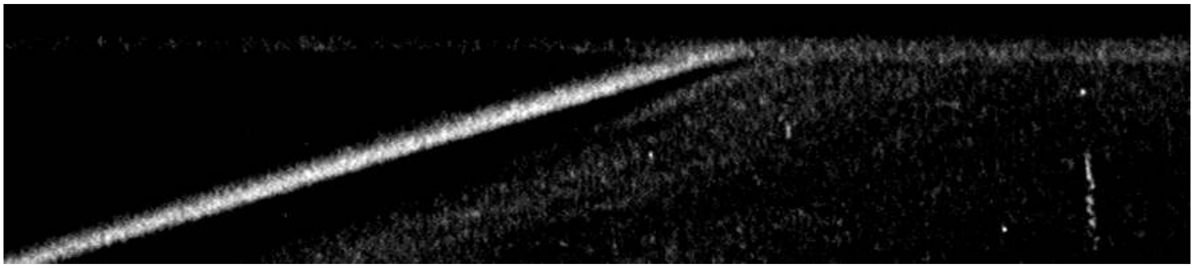

Figure F 4 – A09 with adjusted contrast

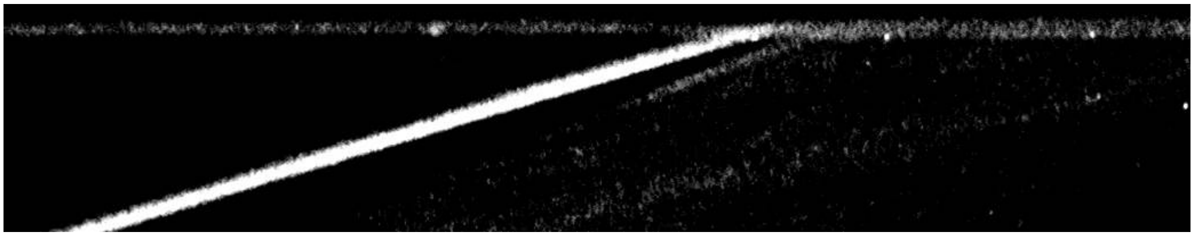

Figure F 5 – A10 with adjusted contrast

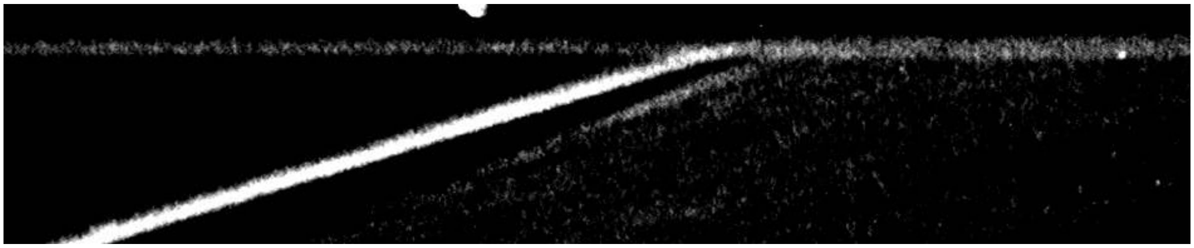

Figure F 6 – A11 with adjusted contrast

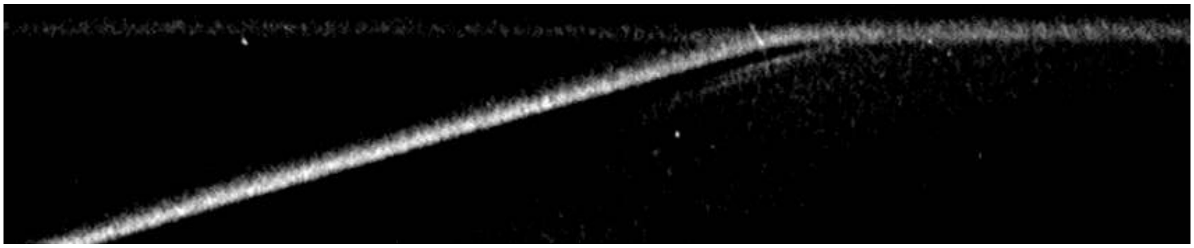

Figure F 7 – A12 with adjusted contrast

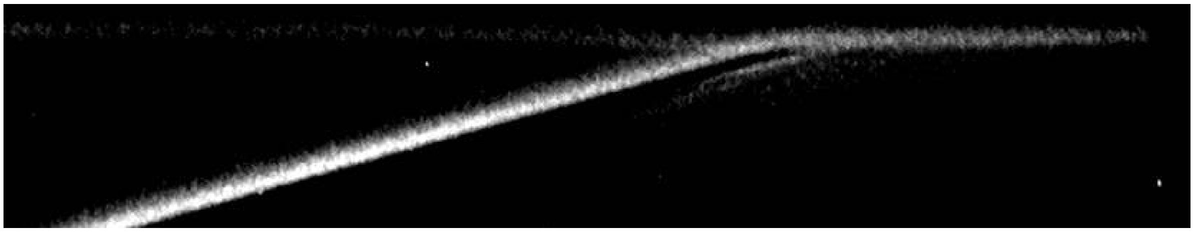

Figure F 8 – A13 with adjusted contrast

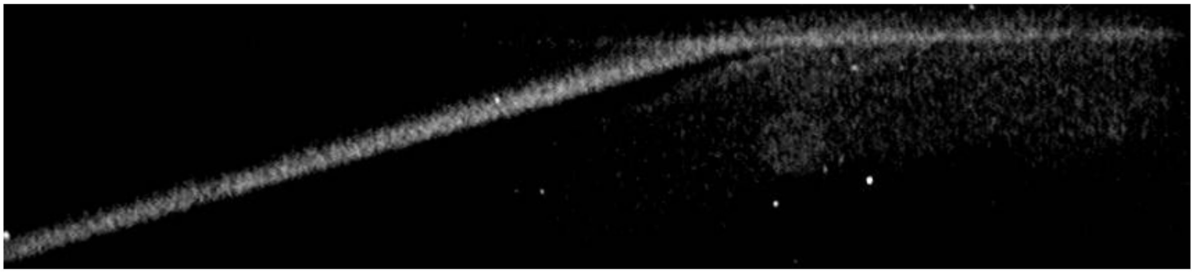

Figure F 9 – A14 with adjusted contrast

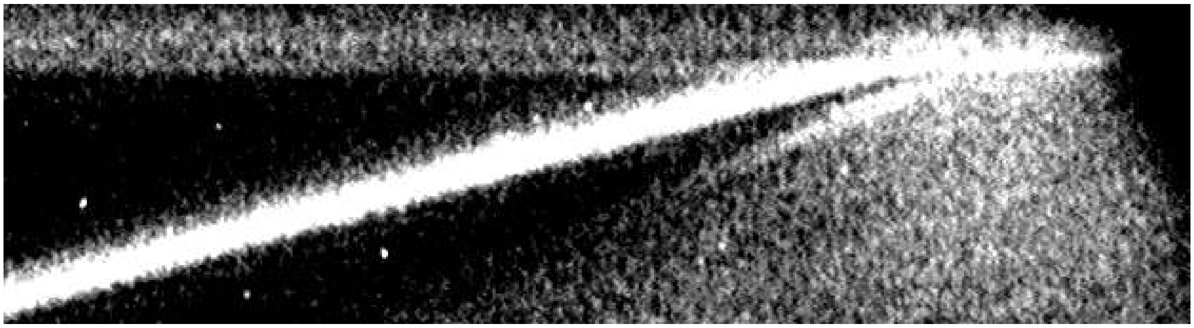

Figure F 10 – A15 with adjusted contrast

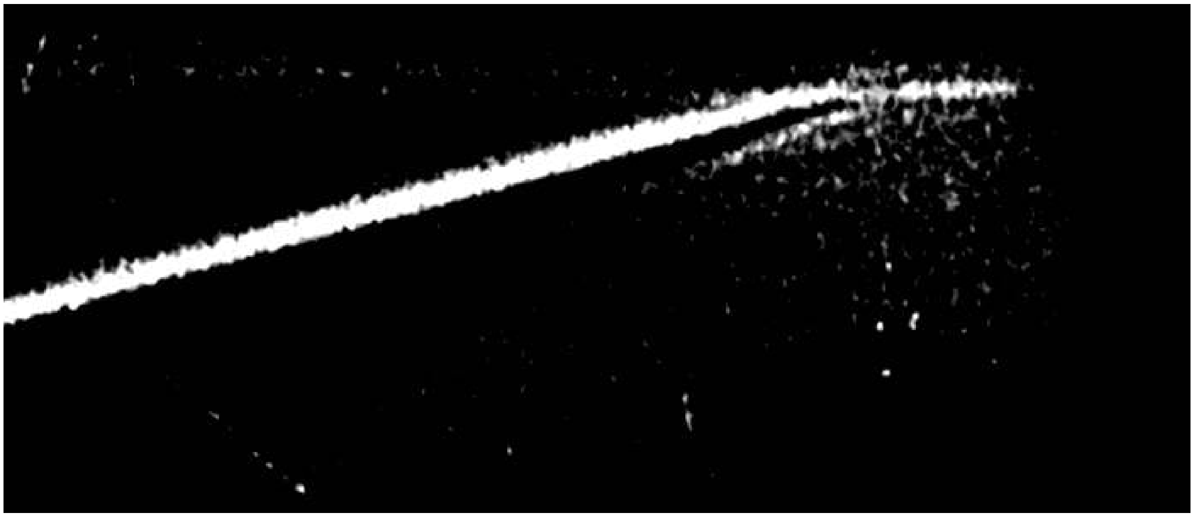

Figure F 11 – A16 with adjusted contrast

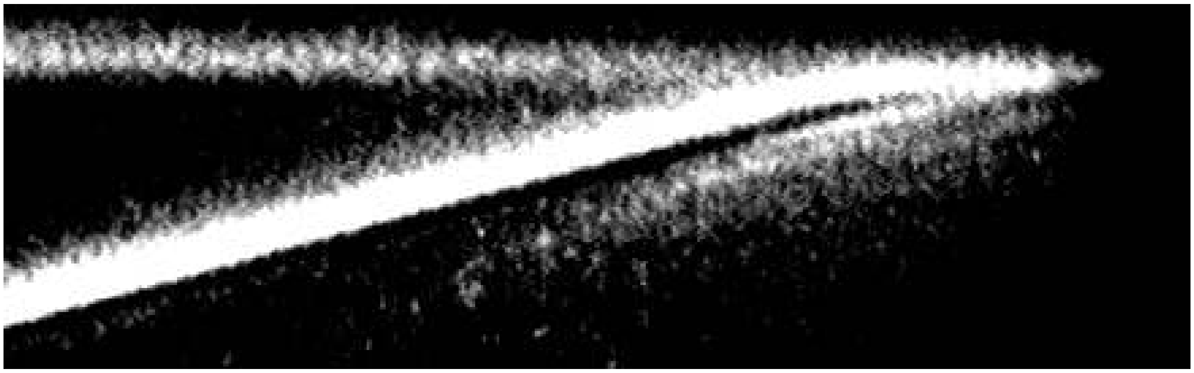

Figure F 12 – A17 with adjusted contrast

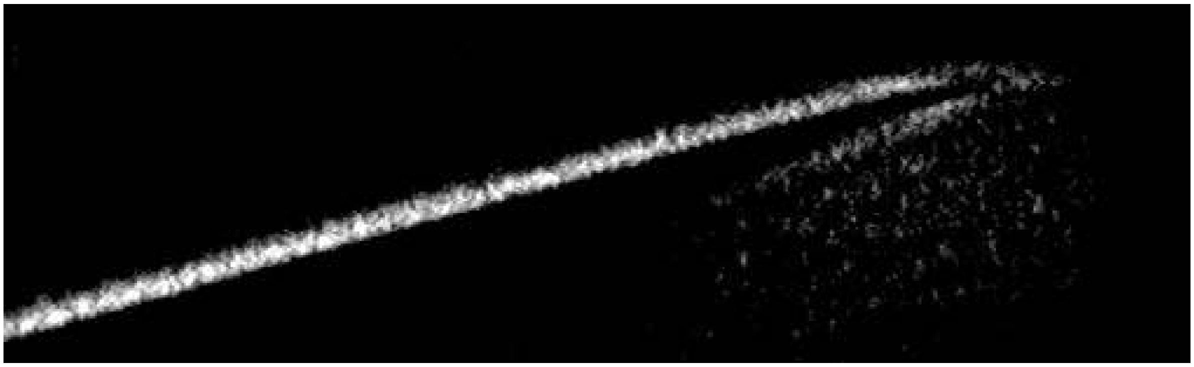

Figure F 13 – A20 with adjusted contrast

Film B

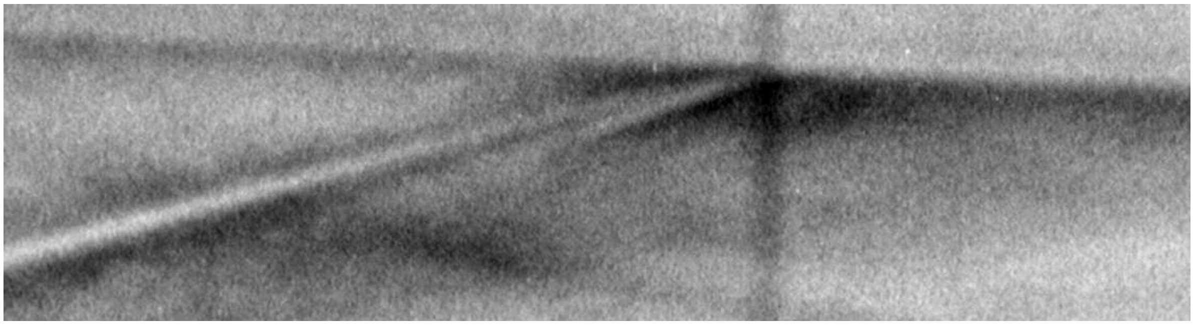

Figure F 14 – B29 with adjusted contrast

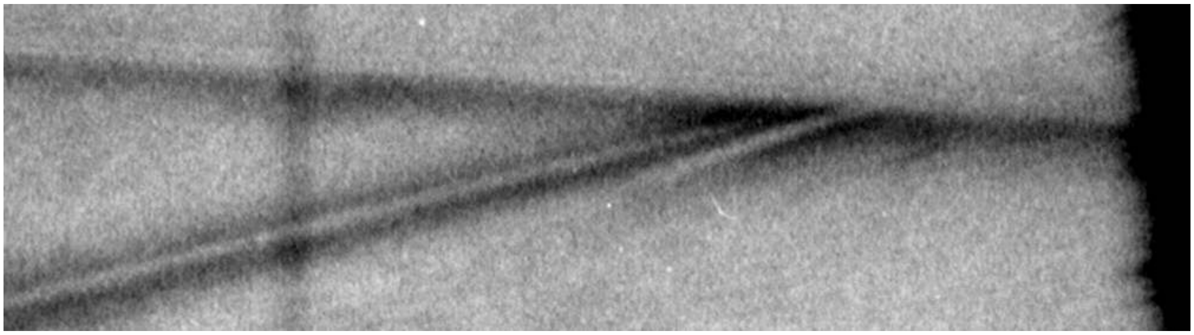

Figure F 15 – B32 with adjusted contrast

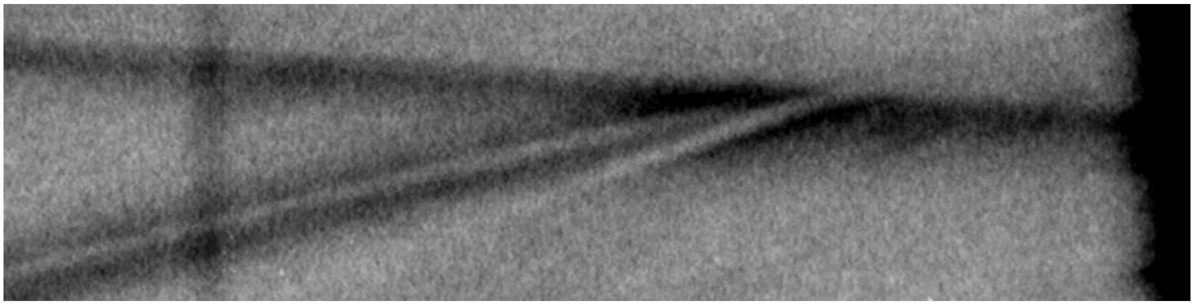

Figure F 16 – B33 with adjusted contrast

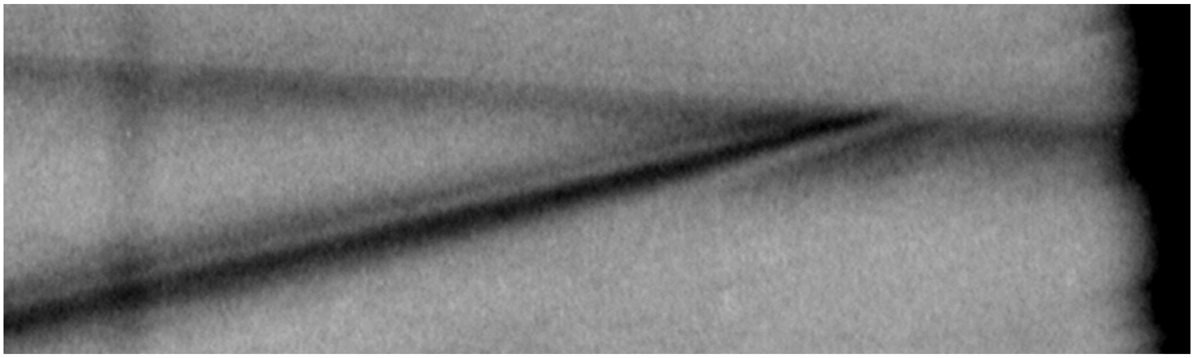

Figure F 17 – B35 with adjusted contrast

Film C

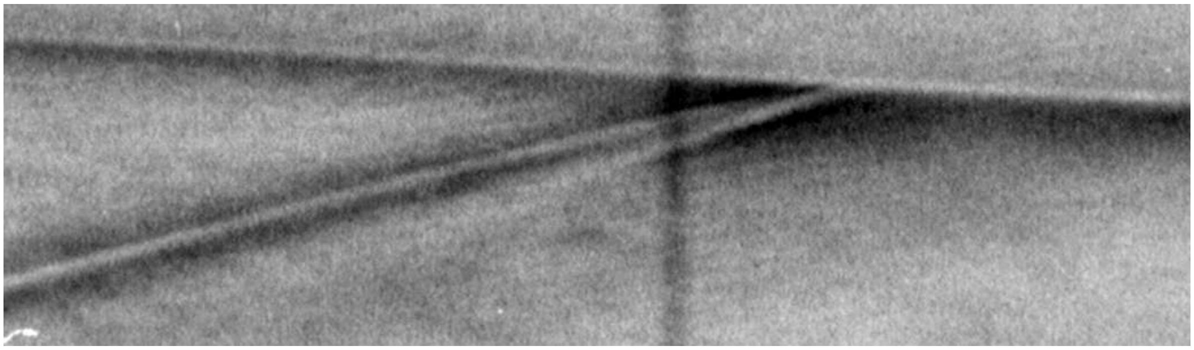

Figure F 18 – C04 with adjusted contrast

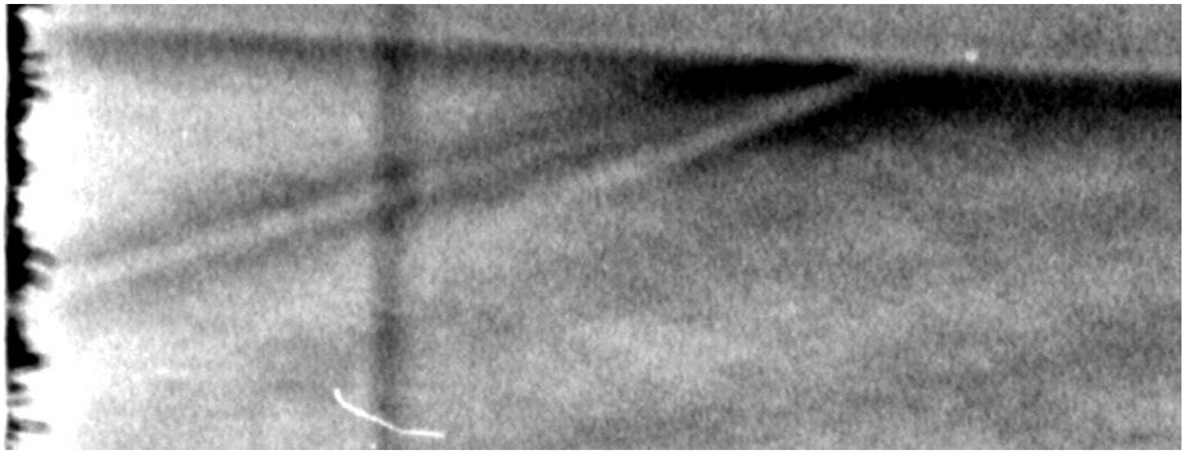

Figure F 19 – C05 with adjusted contrast

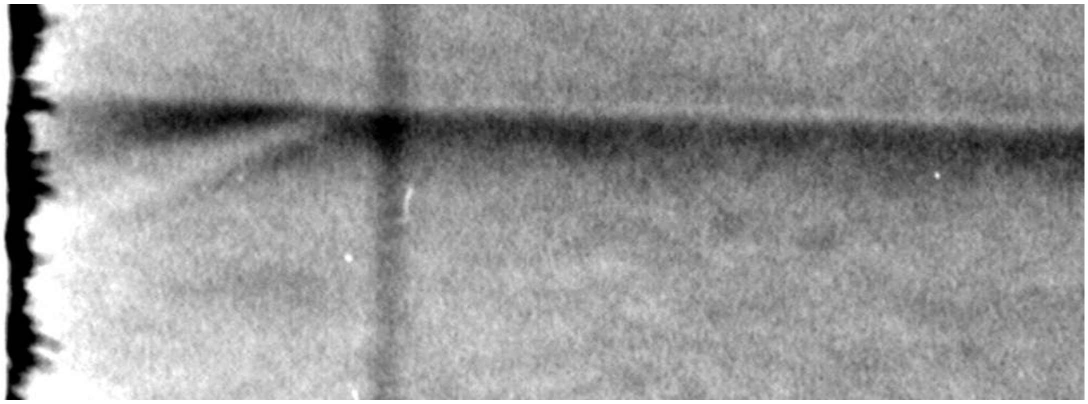

Figure F 20 – C06 with adjusted contrast

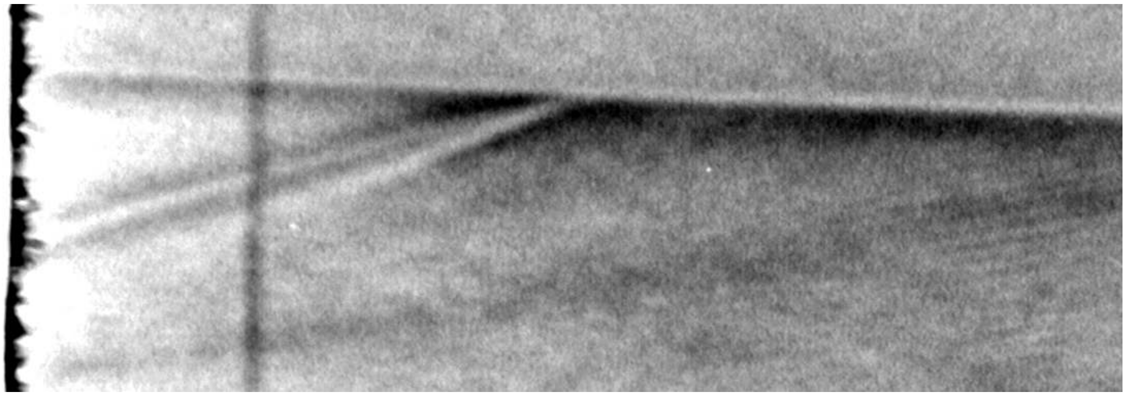

Figure F 21 – C07 with adjusted contrast

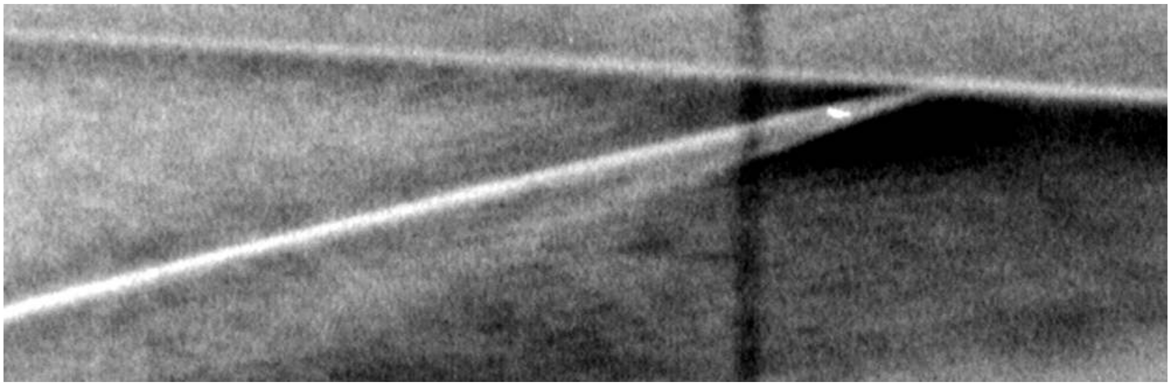

Figure F 22 – C09 with adjusted contrast

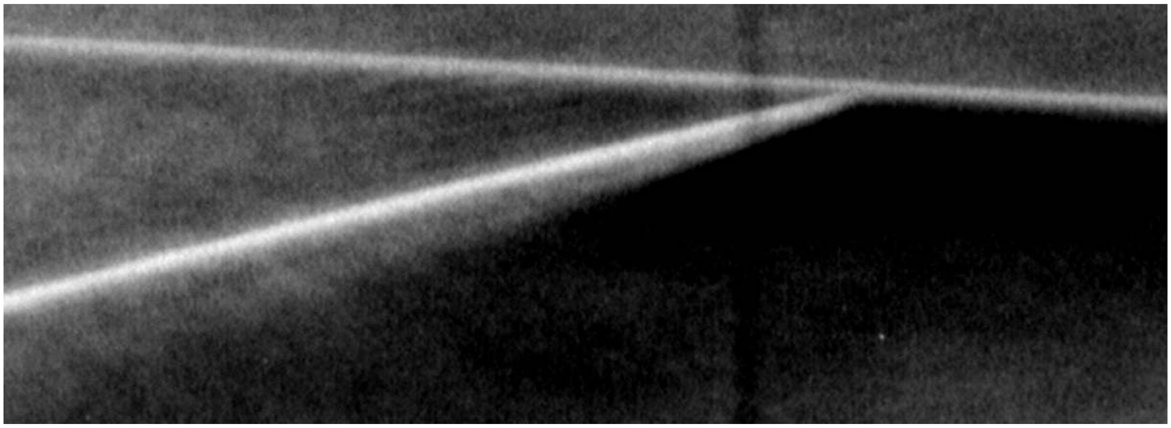

Figure F 23 – C10 with adjusted contrast

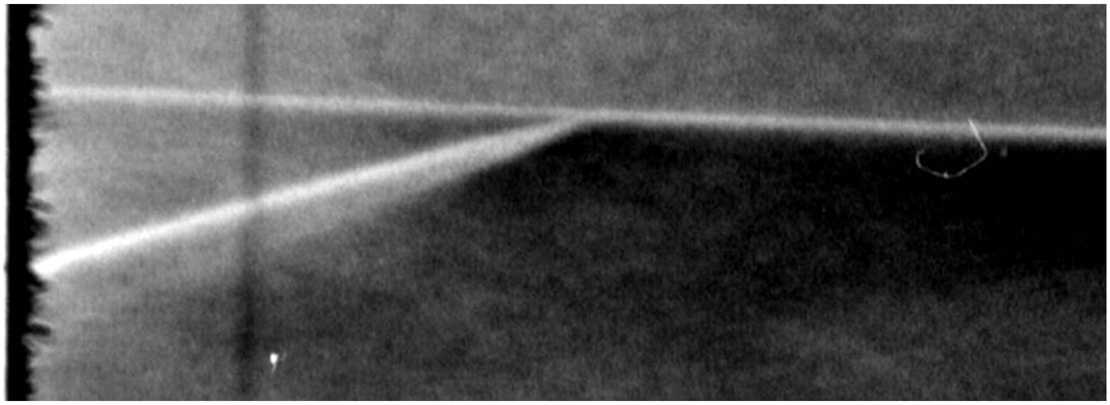

Figure F 24 – C11 with adjusted contrast

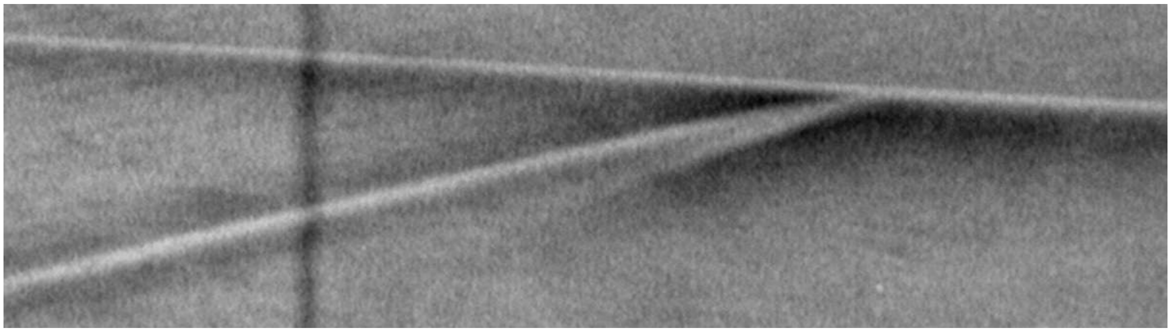

Figure F 25 – C13 with adjusted contrast

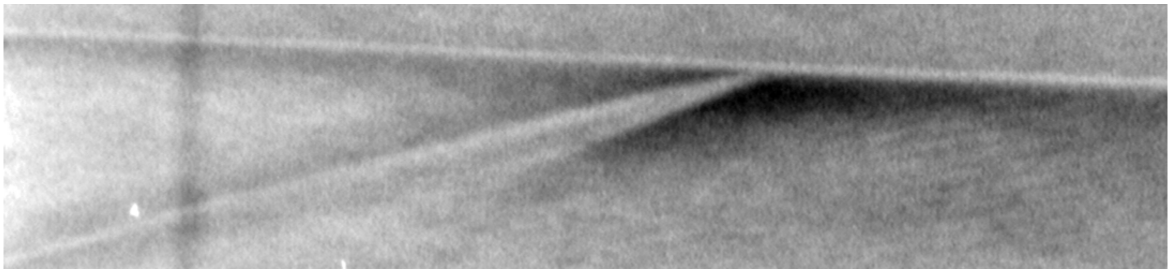

Figure F 26 – C14 with adjusted contrast

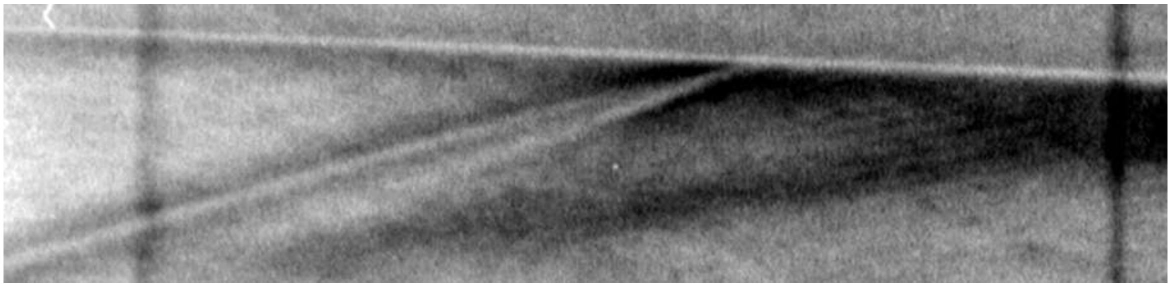

Figure F 27 – C15 with adjusted contrast

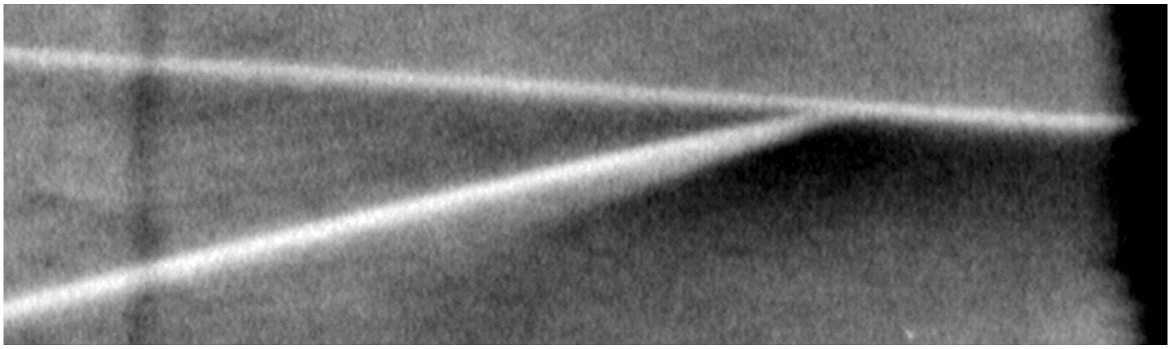

Figure F 28 – C16 with adjusted contrast

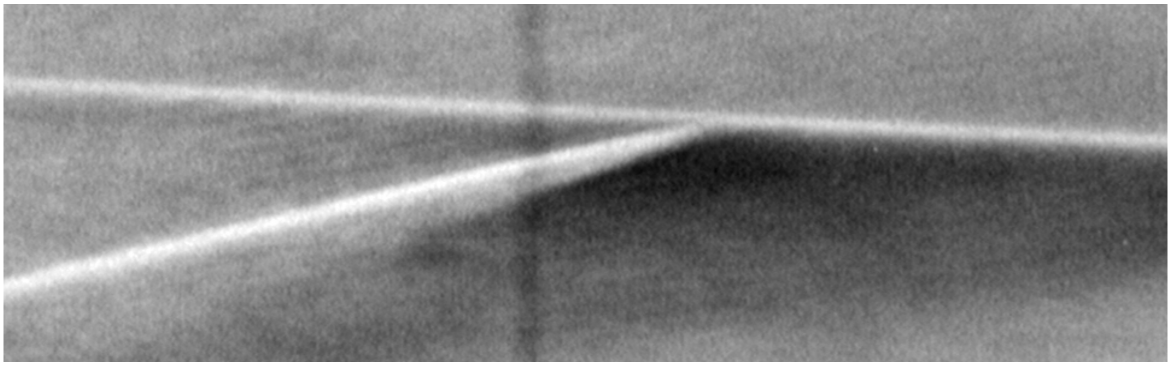

Figure F 29 – C17 with adjusted contrast

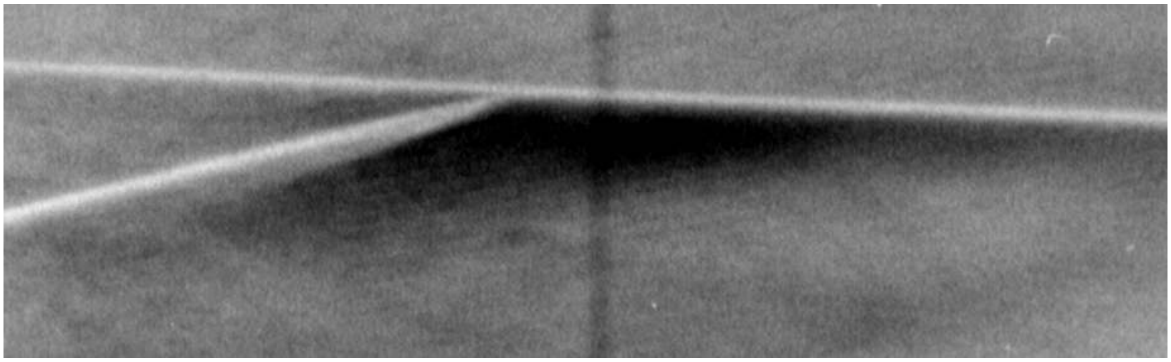

Figure F 30 – C18 with adjusted contrast

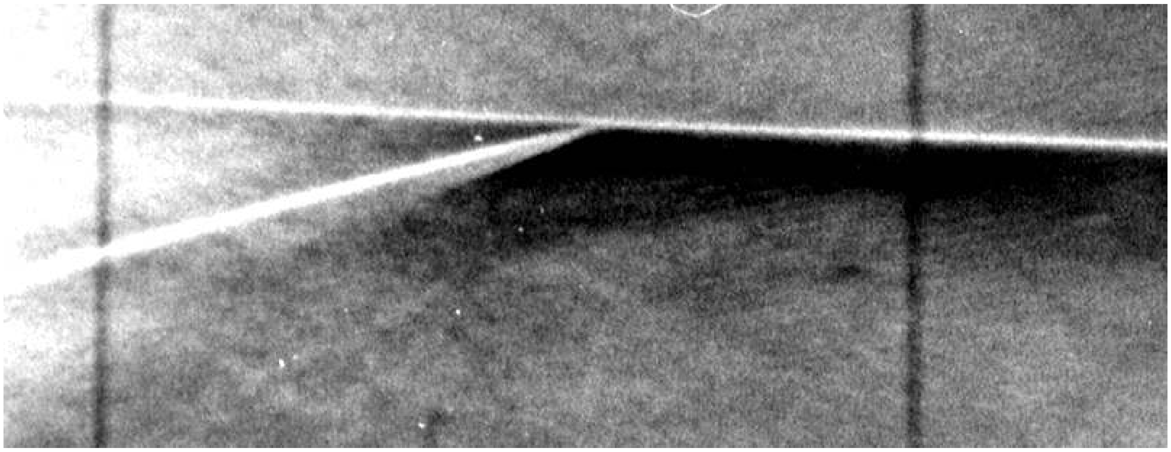

Figure F 31 – C19 with adjusted contrast

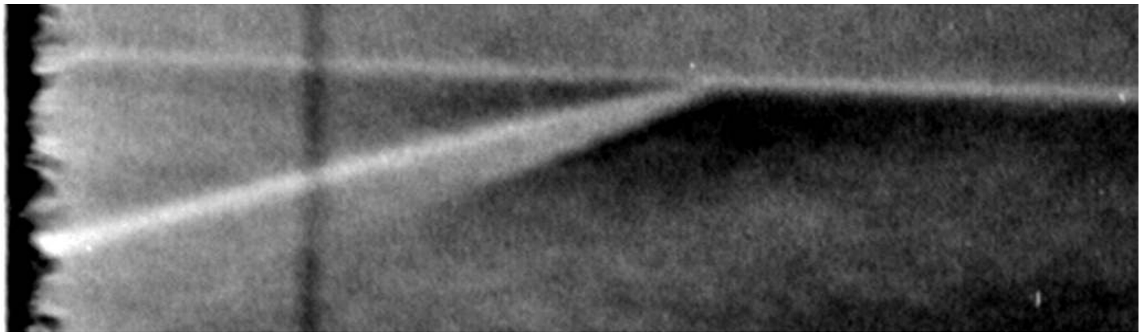

Figure F 32 – C20 with adjusted contrast

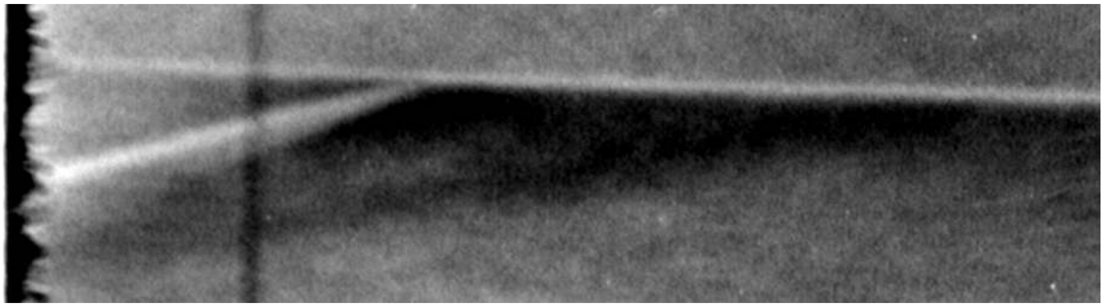

Figure F 33 – C21 with adjusted contrast

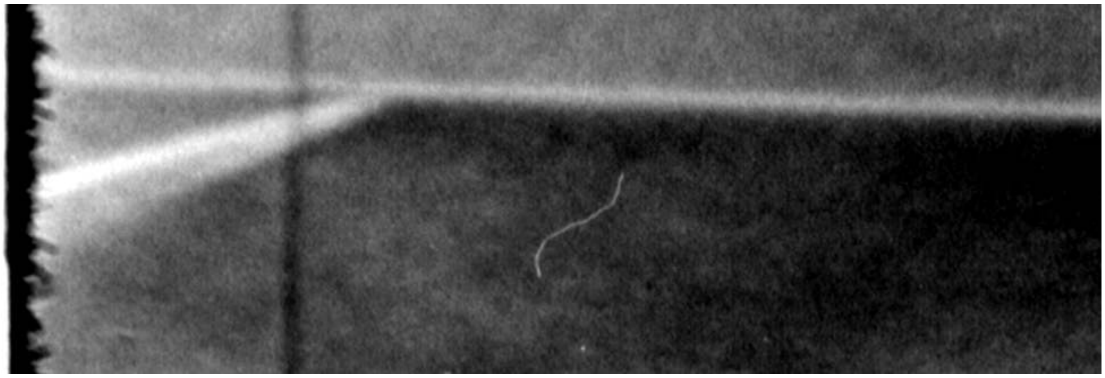

Figure F 34 – C22 with adjusted contrast

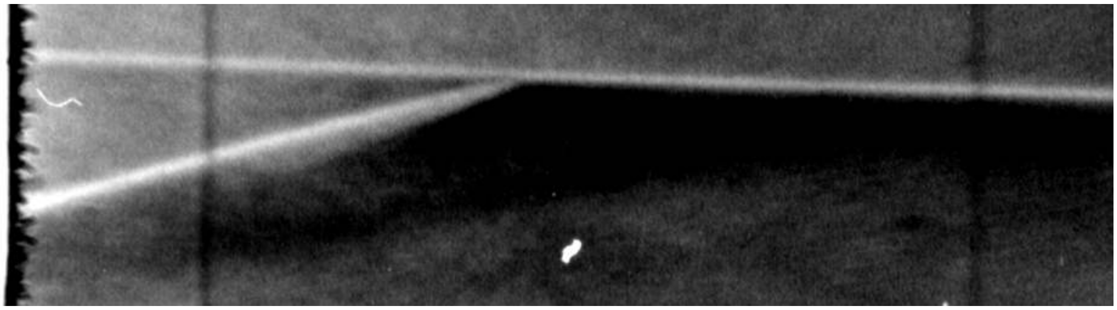

Figure F 35 – C23 with adjusted contrast

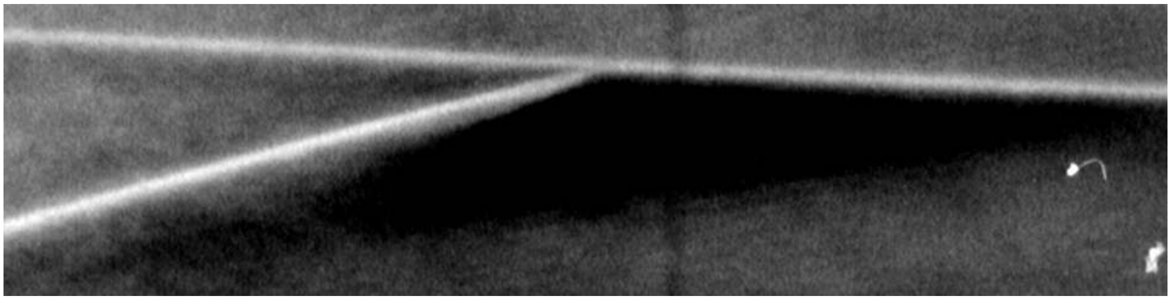

Figure F 36 – C24 with adjusted contrast

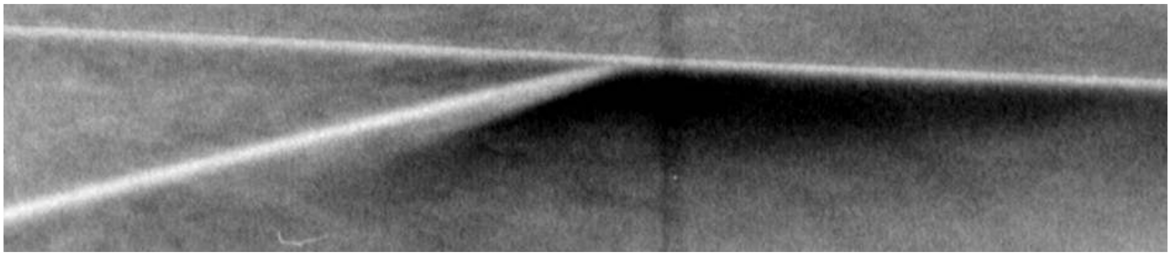

Figure F 37 – C25 with adjusted contrast

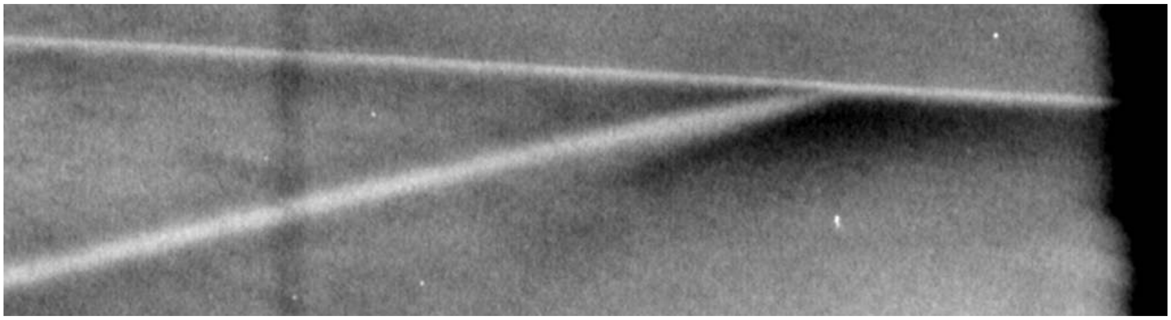

Figure F 38 – C26 with adjusted contrast

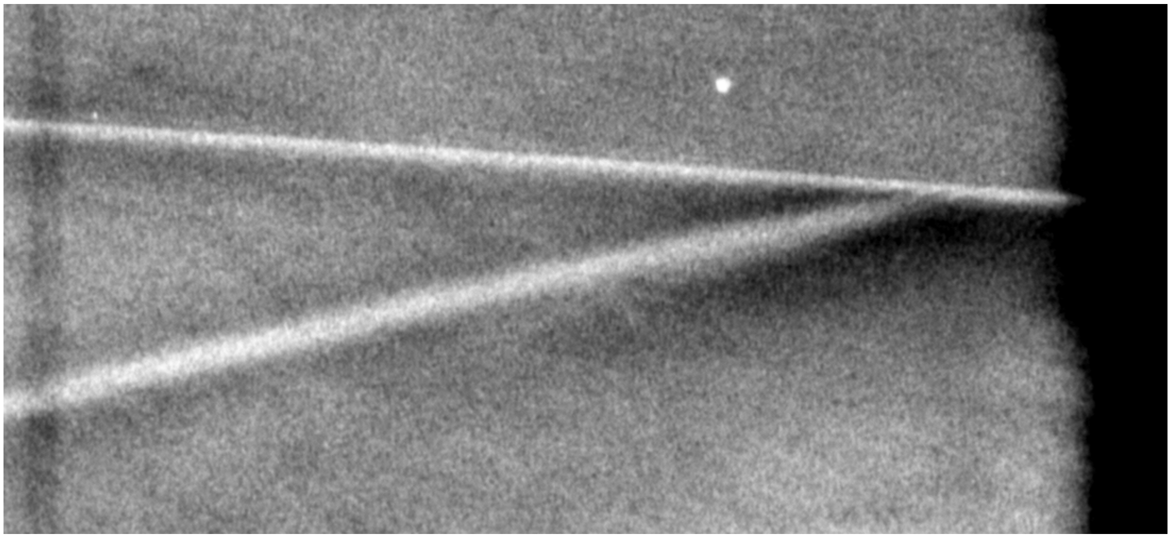

Figure F 39 – C27 with adjusted contrast